BALLOON-BORNE THREE-METER TELESCOPE FOR FAR-INFRARED AND SUBMILLIMETER ASTRONOMY

Grant NAGW-509

Semiannual Status Report No. 4

For the period 1 March 1985 through 31 August 1985

Principal Investigator
Giovanni G. Fazio

October 1985

Prepared for
National Aeronautics and Space Administration
Washington, DC 20546

Smithsonian Institution
Astrophysical Observatory
Cambridge, Massachusetts 02138

The Smithsonian Astrophysical Observatory
is a member of the
Harvard-Smithsonian Center for Astrophysics

The NASA Technical Officer for this grant is Dr. Nancy Boggess, Code EZ-7, National Aeronautics and Space Administration, Washington, D.C. 20546

BALLOON-BORNE THREE-METER TELESCOPE FOR FAR-INFRARED AND SUBMILLIMETER ASTRONOMY

Grant NAGW-509

Semiannual Status Report No. 4

For the period 1 March 1985 through 31 August 1985

Principal Investigator
Giovanni G. Fazio

October 1985

Prepared for
National Aeronautics and Space Administration
Washington, DC 20546

Smithsonian Institution
Astrophysical Observatory
Cambridge, Massachusetts 02138

The Smithsonian Astrophysical Observatory
is a member of the
Harvard-Smithsonian Center for Astrophysics

The NASA Technical Officer for this grant is Dr. Nancy Boggess, Code EZ-7,
National Aeronautics and Space Administration, Washington, D.C. 20546

BALLOON-BORNE THREE-METER TELESCOPE FOR FAR-INFRARED AND SUBMILLIMETER ASTRONOMY

Grant NAGW-509

Semiannual Status Report No. 4

For the period 1 March 1985 through 31 August 1985

Principal Investigator
Giovanni G. Fazio

Co-Investigators

William F. Hoffmann
Steward Observatory
University of Arizona

Doyal A. Harper
Yerkes Observatory
University of Chicago

October 1985

Prepared for
National Aeronautics and Space Administration
Washington, DC 20546

Smithsonian Institution
Astrophysical Observatory
Cambridge, Massachusetts 02138

The Smithsonian Astrophysical Observatory
is a member of the
Harvard-Smithsonian Center for Astrophysics

The NASA Technical Officer for this grant is Dr. Nancy Boggess, Code EZ-7,
National Aeronautics and Space Administration, Washington, D.C. 20546

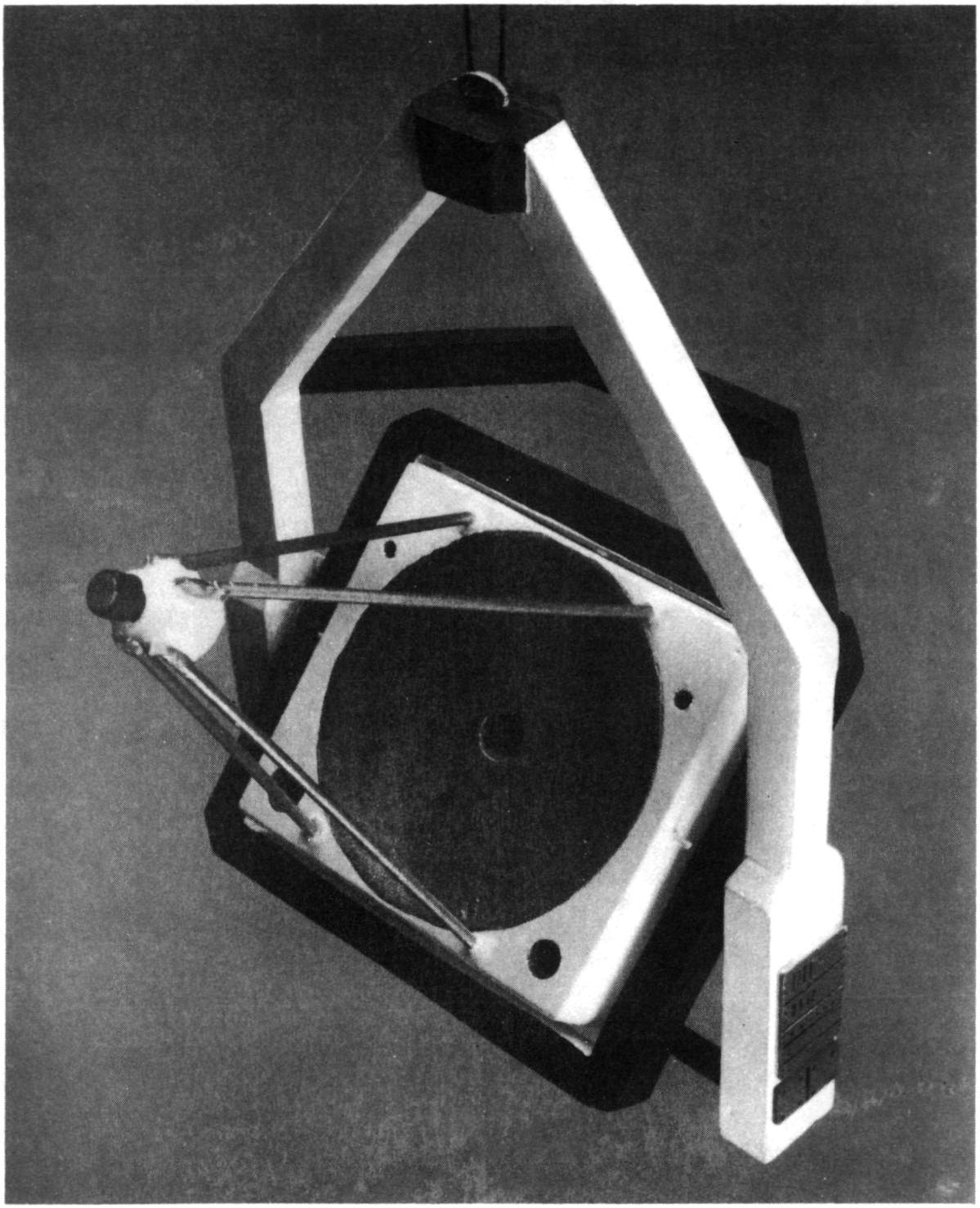

Model of Proposed Balloon-Borne Three-Meter Telescope for Far-Infrared and Submillimeter Astronomy

Abstract

This report presents scientific objectives, engineering analysis and design, and results of technology development for a Three-Meter Balloon-Borne Far-Infrared and Submillimeter Telescope. The scientific rationale is based on two crucial instrumental capabilities: high angular resolution which approaches eight arcseconds at one hundred μm wavelength, and high resolving power spectroscopy with good sensitivity throughout the telescope's 30-μm to 1-mm wavelength range. The high angular resolution will allow us to resolve and study in detail such objects as collapsing protostellar condensations in our own galaxy, clusters of protostars in the Magellanic clouds, giant molecular clouds in nearby galaxies, and spiral arms in distant galaxies. The large aperture of the telescope will permit sensitive spectral line measurements of molecules, atoms, and ions, which can be used to probe the physical, chemical, and dynamical conditions in a wide variety of objects.

An optimized optical, structural, and dynamic design has been achieved which meets the overall scientific performance goals and is compatible with National Scientific Balloon Facility launch weight and other requirements. The design is an f/13.5 Cassegrain telescope with an f/1.33 3-meter primary mirror supported with a 3-axis gimbal and stabilization system. The overall structure is 8.0 meters (26'4") high by 5.5 meters (18'0") in width x 4.0 meters (13'3") in depth and weighs 2,168 kilograms (4,780 pounds). Pointing and stabilization are achieved with television monitoring of the star field, flex-pivot bearing supports, gyroscopes, and magnetically levitated reaction wheels. Analysis shows that a pointing stability of less than one arcsecond rms is achievable.

Technology development has focused on fabrication, low temperature figure distortion, and cooling properties of very lightweight primary mirror candidates which can meet the 30-μm diffraction-limited requirement. We have found that precision replicated carbon-fiber-reinforced plastic sandwich panels weighing less than ten kilograms per square meter can satisfy the replication accuracy required and, through design changes in layup and fabrication, can meet the figure requirements at low temperature.

We are confident that a Balloon-Borne Three-Meter Telescope meeting the scientific requirements can be constructed at reasonable cost and time with the indicated design and technology.

CONTENTS

CONTENTS (Cont.)

CONTENTS (Cont.)

FIGURES

TABLES

CONTENTS (Cont.)

1.0 INTRODUCTION

1.1 Summary

Construction and operation of a Balloon-Borne, Three-Meter Telescope for Far-Infrared and Submillimeter Astronomy has been studied by the University of Arizona, the University of Chicago, and the Smithsonian Astrophysical Observatory under NASA Grant NAGW-509. Photometry, spectroscopy and imaging in the spectral region 30 μm to 1 mm, which is largely inaccessible from the ground, will be possible with this telescope. It will also provide a much needed gain in sensitivity and spatial resolution compared with present one-meter sized balloon and aircraft telescopes. This is the fourth semiannual report issued under the grant and covers the results of the three-meter telescope engineering study which focused on the design areas that determine the fundamental performance of the telescope. These are optical design, lightweight mirror design, pointing and stabilization system design, and lightweight gondola mechanical design.

In order to fully define the gondola, it was also necessary to look into the design of the other telescope subsystems, such as the aspect system, command and telemetry system, and the ground support equipment. These were studied at a more cursory level, basing our design approach on designs presently in use in the proven Smithsonian One-Meter Balloon IR Telescope.

Telescope optical tradeoff studies focused on the impact of varying the fundamental design parameters (aperture, focal ratio, primary-to-secondary separation, and primary-to-focal plane distance) on the focal-plane scale, primary focal ratio, secondary obscuration, chopper induced and field aberrations, and alignment tolerances. We believe the selected f/13.5 Cassegrain is optimum in these terms. The primary mirror must be very lightweight, maintain its figure at operating temperatures of -40 to -50°C, come to thermal equilibrium during ascent and survive high shock loads during parachute opening and landing.

Based on our preliminary mirror test results, we have selected a carbon-fiber-reinforced plastic aluminum-honeycomb-core, primary mirror for the telescope. This design realistically holds promise for meeting the optical requirements of the telescope. Recent developments in carbon-fiber-reinforced glass composite mirrors, "lightweighted" conventional glass mirrors, and foamed aluminum mirrors make them attractive alternatives which we will continue to evaluate.

Telescope mechanical design focused on meeting the requirements of the selected optical design at minimum overall weight and obscuration. Careful consideration was also given to the practical requirements of operation in the field. The selected quadrupod design meets these requirements, at an overall weight savings of some 68 kilograms compared to a more traditional head-ring configuration. This weight savings ripples through the whole gondola design leading to significant reductions in the size of structural elements, motor sizes, electrical power requirements, and so forth. The total weight of this gondola design including all National Scientific Balloon Facility (NSBF) required equipment is projected to be well under the present 5000-pound NSBF weight limit.

Pointing control to better than 1 arcsecond rms, a scientific requirement, is now possible at reasonable cost only because of recent advances in reaction wheel, gyroscope, and brushless motor design. A complete preliminary design for this system, which includes an error analysis and computer evaluation of disturbance torque response, has been performed as part of this grant.

This report presents a complete description of the proposed gondola and discusses its operational interfaces with the NSBF in detail. A cost estimate and program plan for the effort may be found in Section 7 of this report.

The Large Deployable Reflector (LDR) is likely to require new approaches which have not yet been proven in observational infrared astronomy. Some of these new concepts can be tested on the Three-Meter Balloon-Borne Telescope. One such possibility is the two-stage optical configuration proposed by Meinel (private communication) in which wave-front correction and sky beam chopping is accomplished at a flat quaternary mirror. The primary purpose of this concept is to apply wave-front corrections at a relatively small optical element located at an image of the primary mirror rather than on the very large 20-m LDR primary mirror itself. A potential secondary advantage of this concept is to make possible sky beam chopping by vibrating the quaternary mirror which is substantially smaller than the secondary. Since this mirror is located at an image of the primary, the chopped beam remains fixed on the primary mirror reducing potential thermal offset and noise.

Another new LDR concept that could be evaluated on the Three-Meter Balloon-Borne Telescope is an alternative to secondary mirror chopping that provides reimaging optics in the cold dewar and that images the primary mirror onto a small optical flat which can be vibrated to provide sky beam chopping. Consideration will be given to exploring these alternatives as the design effort proceeds.

1.2 Scientific Objectives

1.2.1 Introduction

The scientific rationale for the Three-Meter Balloon-Borne Far-Infrared and Submillimeter Telescope is based on two crucial instrumental capabilities: high angular resolution (at 100 μm wavelength approaching 8 arcseconds), and high resolving power spectroscopy with good sensitivity. Throughout the detailed description of the scientific objectives these two themes will be mentioned repeatedly.

In Figure 1.2-1 the typical sizes of objects this Three-Meter Balloon-Borne Telescope will study are indicated, as well as the distances at which they are likely to lie. Three diagonal lines indicate angular resolutions of 30 arcseconds, about the best achievable at 100 μm wavelength with one-meter-class telescopes, such as the Kuiper Airborne Observatory (KAO), other balloon-borne telescopes, and the Space Infrared Telescope Facility (SIRTF); 8 arcseconds, the resolution achievable with the Three-Meter Balloon-Borne Telescope; and 1 arcsecond, the resolution achievable with the LDR. From the figure it can be seen that the three-meter telescope will allow us to resolve and study in detail such objects as collapsing protostellar condensations in our own galaxy, clusters of protostars in the Magellanic Clouds, giant molecular clouds in nearby galaxies, and spiral arms in distant galaxies. Figure 1.2-2 is an optical charge-coupled device (CCD) photograph of the galaxy M51 showing the relative increase in angular resolution in going from 30 arcseconds to 8 arcseconds to 1 arcsecond. The reason why it is necessary to resolve these objects is given in the following sections, but it is clear that the Three-Meter Balloon-Borne Telescope will significantly increase the resolution with which we view the universe at far-infrared and submillimeter wavelengths.

The second major capability of the Three-Meter Balloon-Borne Telescope is sensitive observations of spectral lines. The region from 1 to 100 μm is full of significant spectral lines of molecules such as CO, H_2, HD, H_2O, OH, etc., and atoms and ions such as C I, O I, S I, Si I, C II, Si II, O III, N III, Ne III, S III, etc. These lines can be used to probe the physical, chemical and dynamical conditions in a wide variety of objects. The Three-Meter Balloon-Borne Telescope is important for these observations because its large collecting area allows for the first time detection of very weak lines in small ($\leq$ 8 arcseconds) sources.

The two areas of scientific investigation where the Three-Meter Balloon-Borne Telescope will have its greatest impact are in studies of the formation of stars and properties of the interstellar medium within our own galaxy and in nearby galaxies, and in studies of the structure of galaxies, including their formation and evolution, as well as the nature of their energetic nuclei.

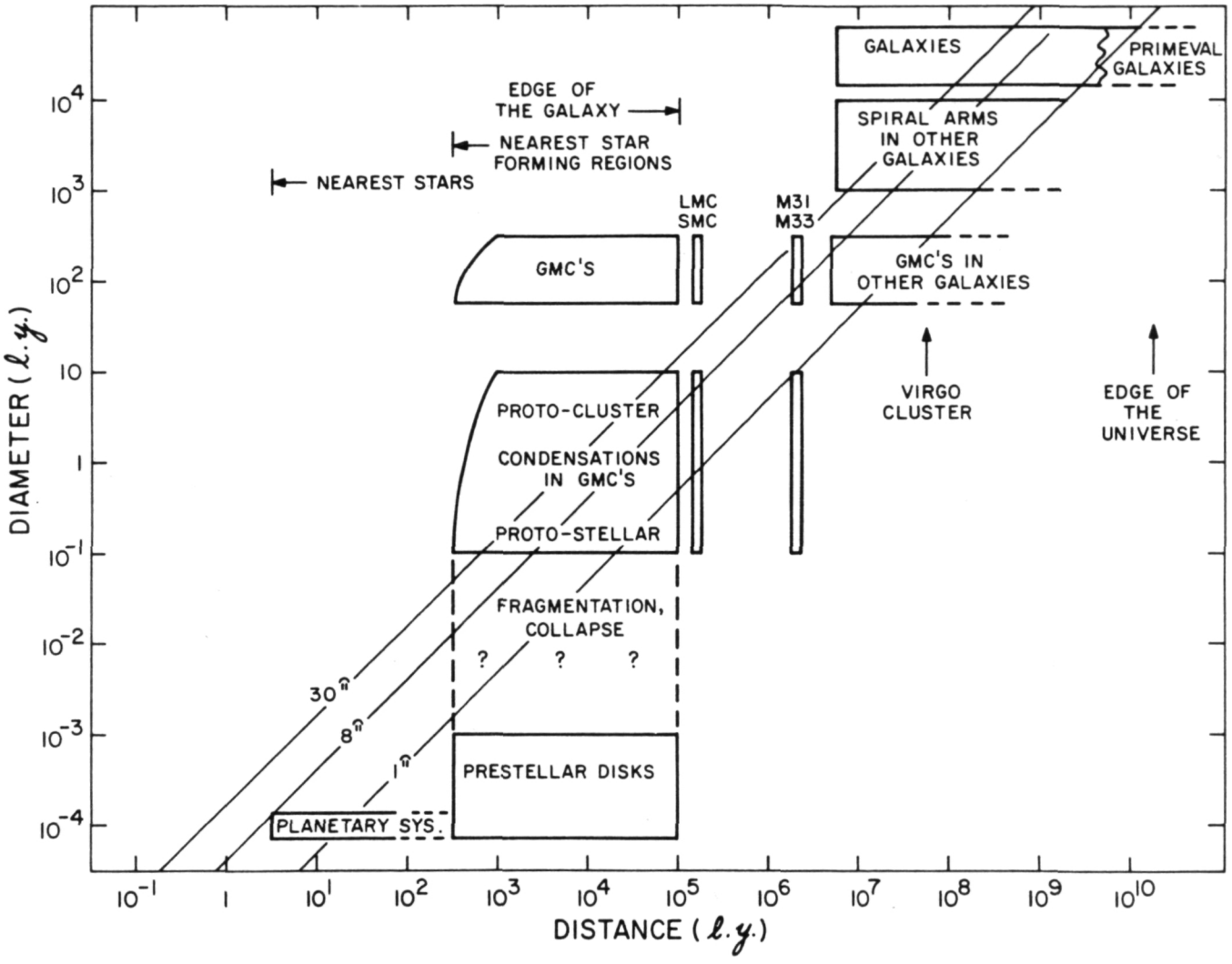

Figure 1.2-1. Typical Sizes of Objects to be Studied by the Three-Meter Balloon-Borne Telescope

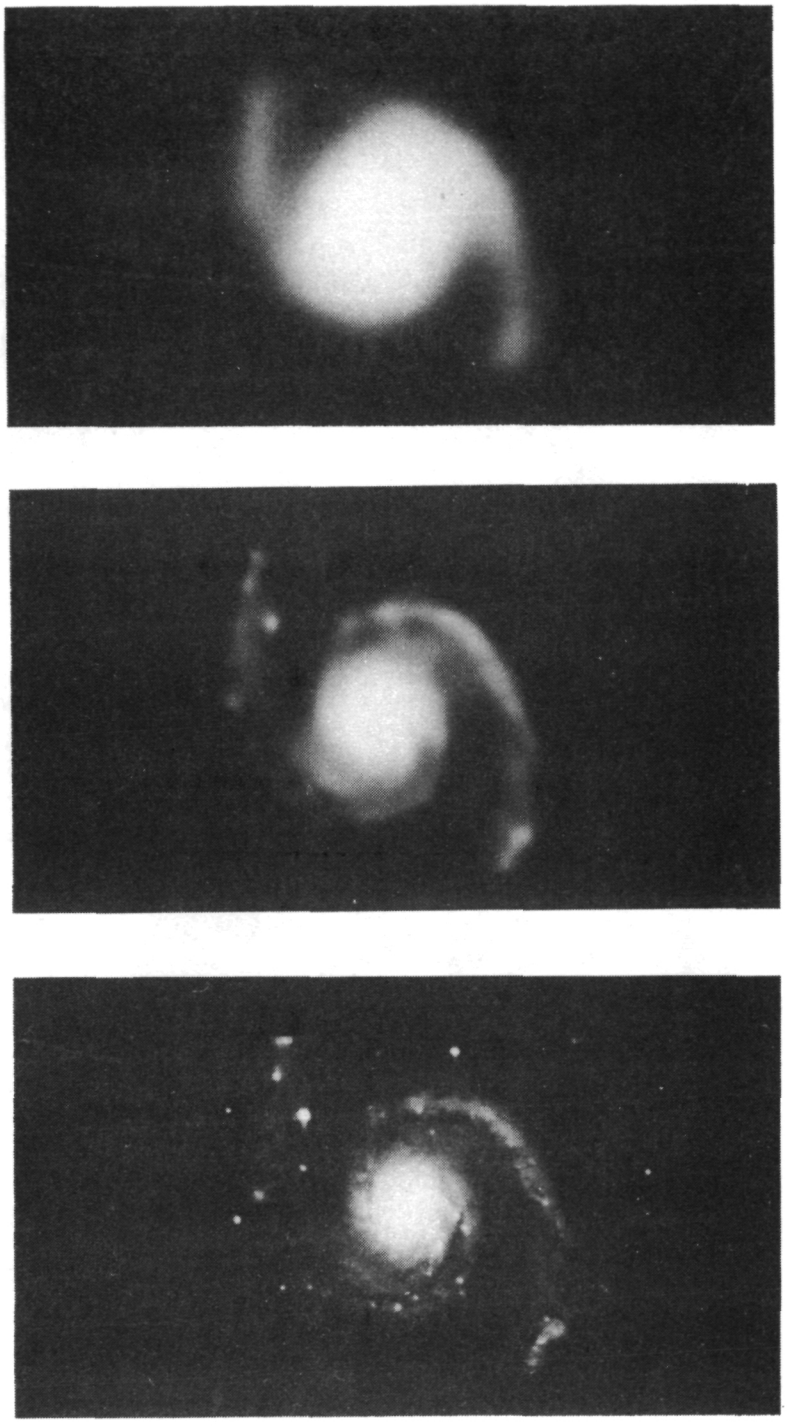

Figure 1.2-2. Optical CCD Photograph of M51 Showing the Relative Increase in Angular Resolution in Going from 30 Arcseconds to 8 Arcseconds to 1 Arcsecond.

1.2.2 Star Formation and the Interstellar Medium

Far-infrared observations provide a unique set of tools for studying star formation: first, because stars form in dense clouds that heavily attenuate radiation at shorter wavelengths and, second, because many important processes occur in gas and dust clouds with temperatures between a few tens and a few hundreds of degrees Kelvin. Most of the cooling for such clouds is provided by far-infrared continuum and line emission.

Perhaps the most fundamental quantity provided by far-infrared measurements is the total luminosity of dust-embedded energy sources. Very little dust is required to completely absorb stellar ultraviolet and optical emission, and this energy is subsequently re-emitted in the far infrared.

On the other hand, the penetrating power of the far-infrared radiation allows a clear view of obscured sources. For example, far-infrared atomic fine-structure lines, unlike their optical counterparts, are essentially unaffected by reddening or self-absorption. Far-infrared fine-structure lines are also very insensitive to electron temperature. Thus, they can provide very direct information on electron density, relative ionic and atomic abundances, cloud masses, and spectral types of ionizing stars. In addition, lines like those from O I at 63 μm and C II at 157 μm, which are major coolants for neutral gas at temperatures of 100-1,000°K, provide essential data on the heating of interface regions between ionic and molecular clouds and on shock heating of the interstellar medium.

Molecular lines at far-infrared and submillimeter wavelengths are important for two reasons. First, they represent dominant coolants and important diagnostic indicators for gas with temperatures of a few hundred degrees. Observations of emission from many different levels of CO, for example, can yield accurate estimates of molecular hydrogen density, temperature, and total CO column density in warm, shocked gas in active star formation regions. Second, far-infrared observations may allow detection of molecular species not accessible at other wavelengths (e.g., many of the most abundant hydrides). This could provide important clues to both abundances and chemical processes in the clouds.

Most far-infrared investigations of active regions of star formation have been limited not by instrumental sensitivity but by source confusion. The mean projected separation of stars in nearby open clusters (for which membership is fairly complete) is of the order of 0.1 pc. Separations within the most compact parts of the youngest clusters (e.g., the Trapezium and KL clusters in the Orion Nebula) may be smaller by a factor of 3-10. Other phenomena relevant to the process of star formation (e.g., Jeans' lengths for gravitational collapse in dense molecular clouds, the sizes of the high-velocity molecular flows seen in Orion and other sources, and the projected thickness of shock and ionization fronts) also have scale sizes in the range of .01-.1 pc. Since the nearest star-forming regions are typically a few hundred pc away, only the closest sources and the largest scales can be adequately resolved by current far-infrared telescopes (Figure 1.2-1).

In addition to extending our knowledge of regions such as the Orion/BN/KL complex, the Three-Meter Balloon-Borne Telescope should provide a powerful tool for studying formation of lower-mass stars. The University of Chicago group (Keene, et al., 1983) has recently reported observations of a compact object in the "Bok globule" B335. The source has a luminosity of less than 6 $L_{\odot}$, a grain temperature of less than 19 K, and a size at 100 μm of less than 20 arcseconds. It is the lowest luminosity source observed to date that has an associated "molecular outflow." As yet, no near-infrared counterpart to the far-infrared source has been detected. Since the current measurements are limited by diffraction, a larger telescope might allow the source to be resolved, and it would certainly permit much more stringent constraints to be placed on optical depths and column densities.

The nearest star-forming regions lie at a distance of 100-200 parsecs. At 150 parsecs, 2 arcseconds corresponds to a linear scale of 300 AU. This is close to the diameter of the infrared emitting circumstellar disks observed around Vega and Beta Pictoris (Aumann, et al., 1984; Aumann, 1984; Smith and Terrile, 1984; Harper, et al., 1984) and to the expected sizes of dense circumstellar disks around low mass protostars. Such disks may play crucial roles in formation of planetary systems and in the dissipation of angular momentum during protostellar collapse. The Three-Meter Balloon-Borne Telescope would afford the first opportunity to study such structures in the far infrared.

1.2.3 Galactic Structure

The major unsolved problems of galactic structure are how galaxies form, how they evolve through successive generations of star formation, and the nature and significance of energetic events in their nuclei. A full-scale attack on these problems in the far infrared will require the very large collecting area and high angular resolution of space-based instruments such as LDR -- particularly for attempts to observe galaxies at very high redshifts. However, the Three-Meter Balloon-Borne Telescope could contribute substantially to our understanding of processes occurring in the nearest galaxies, thereby laying the groundwork for later work with larger instruments.

At 100 μm the Three-Meter Balloon-Borne Telescope can resolve an object about 100 pc in size at a distance of approximately 3 Mpc. This is a sufficiently large distance to include the nearest field galaxies and groups beyond the Local Group. One hundred pc is comparable to the scale sizes of individual giant molecular clouds, to the thicknesses of the disks of spiral galaxies, and to the scale of "circum-nuclear" structure in our own galaxy (e.g., to the major features in far-infrared maps made with angular resolutions of a few arcminutes). This is the scale required, for example, to distinguish low-luminosity "nuclear" sources from nearby, luminous molecular cloud complexes. It is also the scale at which one can begin to test hypotheses concerning star formation in spiral arms and circum-nuclear "rings" (Figure 1.2-1).

Figure 1.2-3 illustrates the impact angular resolution can have on our understanding of galactic structure. It shows optical, far-infrared, and radio images of the Sb galaxy NGC 4736 (distance ~5 Mpc). The upper left and upper right panels show optical photographs in continuum and Hα emission, respectively (resolution limited by seeing to 1-2 arcseconds). The lower right panel shows far-infrared data taken with the KAO telescope (49" beam) superposed on a 6-cm VLA map, with an angular resolution of ~3". The left-hand map is the 6-cm VLA map which has been smoothed by applying a Gaussian taper to the data in the UV plane, giving a resolution of ~9". Thus, the tapered map has a resolution similar to that which the Three-Meter Balloon-Borne Telescope would have at 100 μm, and the beam size of the untapered map is analogous to the 100-μm beam size of LDR. The jump in angular resolution between earlier radio data and the VLA maps shown here is analogous to the improvement to be expected when going from current one-meter far-infrared telescopes to the proposed Three-Meter Balloon-Borne Telescope and LDR. Features in the early radio maps were initially interpreted as double-lobed structures similar to those seen in radio galaxies. In the high-resolution data, it is clear that the radio emission comes from a ring of "knots" that are more similar to the structure seen in Hα photographs and may be powered by accelerated star formation in a gaseous "ring." Closer examination reveals that the Hα and radio knots are not exactly coincident, suggesting that the optical extinction is heavy and variable. To understand such complex systems, it is essential to have optical, infrared, and radio observations (both continuum and line data) with the highest possible angular resolution.

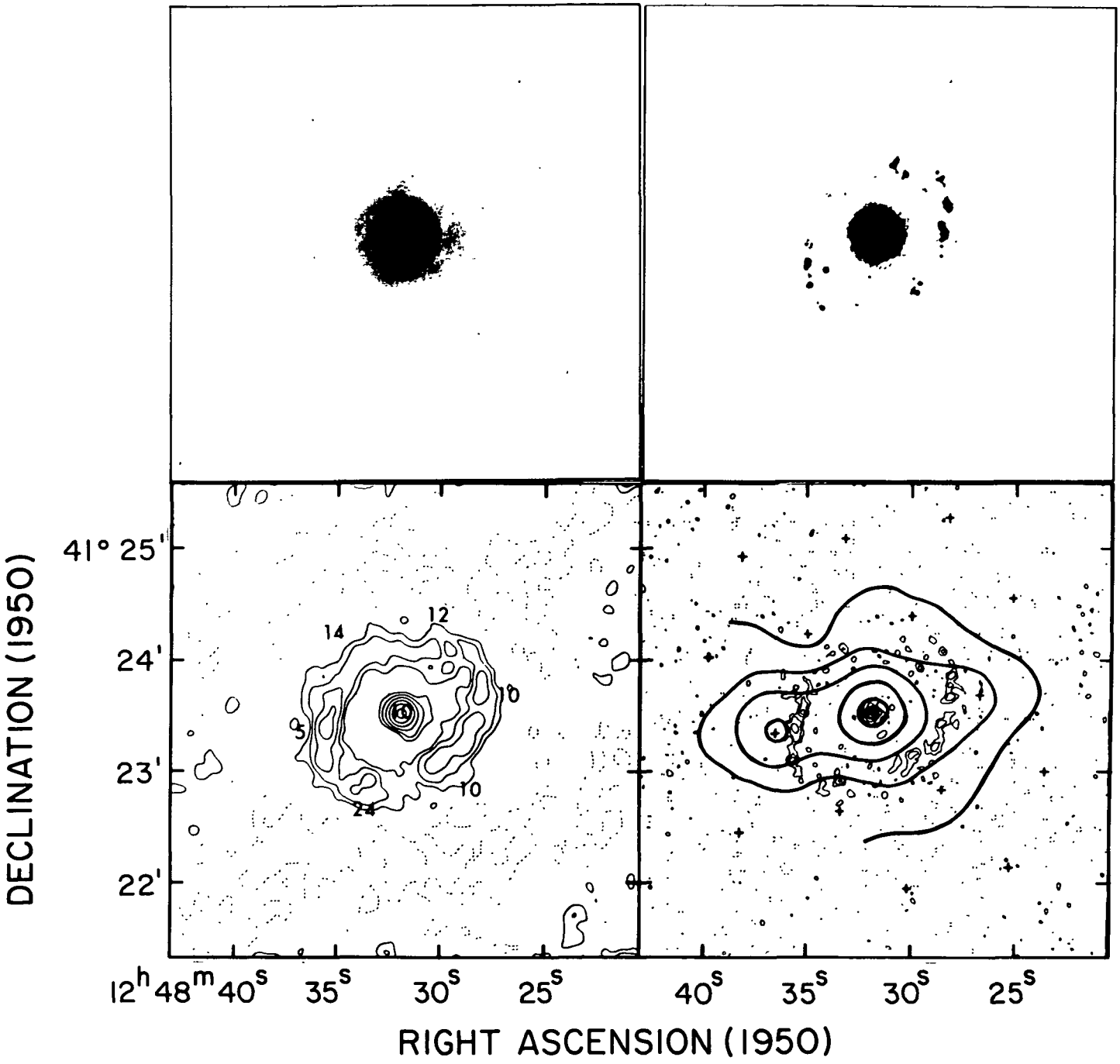

Figure 1.2-3. Impact of Angular Resolution on Our Understanding of Galactic Structure

1.3 Scientific Performance

The infrared performance of the Three-Meter Balloon-Borne Telescope is determined by the aperture, effective telescope emissivity, and the telescope temperature, the same items that determine the LDR performance. With the exception of the aperture, the values for these quantities on the gondola should be similar to those of the LDR. This telescope will operate at an ambient temperature of about 230°K and should have an emittance near 10%. A lower value of the mirror emittance may be achievable. Figure 1.3-1 gives the broadband sensitivity at 100 μm vs. the diffraction-limited beam size for existing and planned instruments. The highest sensitivity is at the top. Figure 1.2-1 shows clearly the effectiveness of the Three-Meter Balloon-Borne Telescope for follow-through of 100-μm sources at the limit of IRAS sensitivity, a task of which the KAO is not capable. The Three-Meter Balloon-Borne Telescope has substantially less sensitivity than SIRTF for broadband photometry because of its higher temperature. It is superior to SIRTF only in angular resolution and in high spectral resolution observations limited by detector noise.

Figure 1.3-2 shows the background-limited sensitivity for a photoconductive detector operated broadband and diffraction-limited. The dashed line represents achieved detector performance at very low backgrounds. From this figure it can be seen that observations at 100 μm will become detector noise limited only at a spectral resolution of >10,000.

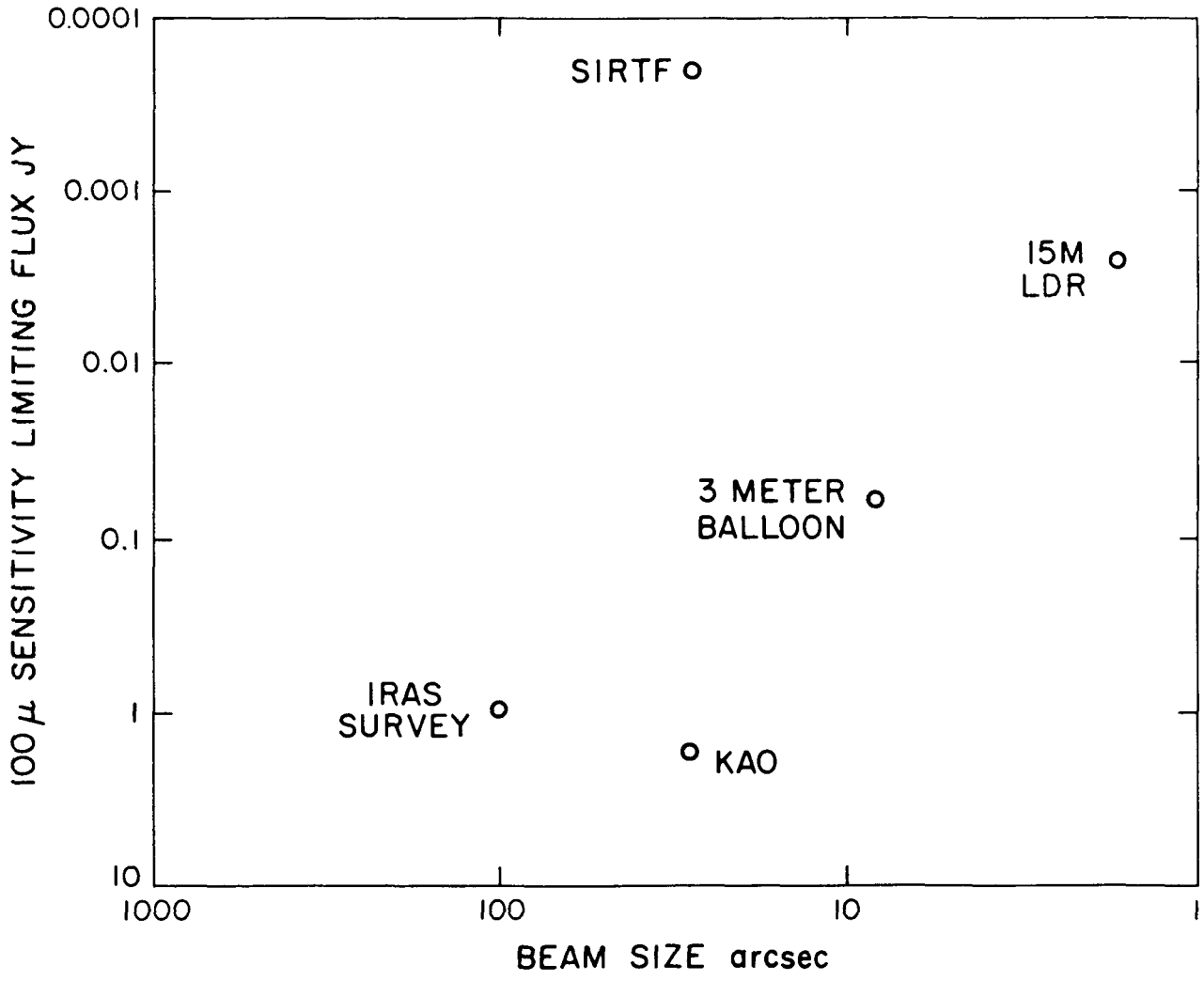

Figure 1.3-1. Broadband Sensitivity at 100 μm vs. the Diffraction-Limited Beam Size. For the pointed telescopes, the limiting flux is given for a signal-to-noise of 10σ, bandwidth $\Delta\lambda/\lambda = 0.5$, beam size of 1.22 λ/D, photoconductor detective quantum efficiency of $\eta = 0.5$, and integration time of 30 minutes with half of the time on the source. For the Three-Meter Balloon-Borne Telescope and LDR, the telescope emissivity and instrument efficiency are each taken to be 0.1 and the telescope temperature 220°K. For the KAO, the telescope emissivity, sky emissivity, and transmission are taken to be 0.2, 0.2, and 0.8 respectively. The IRAS survey limiting flux is taken from IRAS specifications.

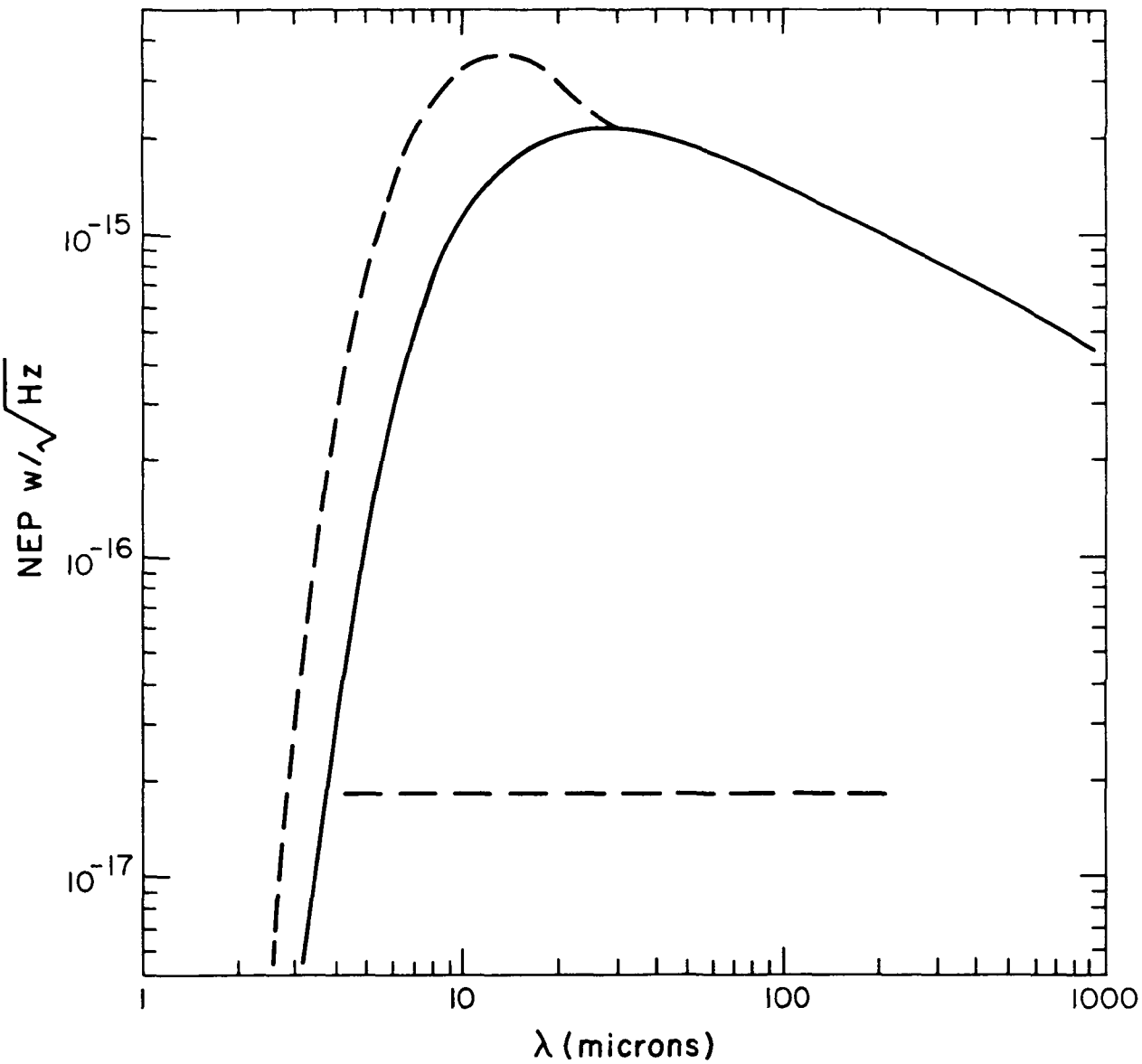

Figure 1.3-2. Background-Limited Sensitivity of Far-Infrared Detectors. The curve is for telescope temperature of 220°K, telescope emissivity of 0.1, telescope and instrument efficiency of 0.1, bandwidth $\Delta\lambda/\lambda = 0.5$, beam size of 1.22 λ/D, and photoconductor detective quantum efficiency $\eta = 0.5$. The dashed extension gives the NEP for the wavelengths less than 30 μm for a 30-μm diffraction-limited beam size. The horizontal dashed line represents present or anticipated limits on detector performance at very low background.

2.0 TELESCOPE AND GONDOLA DESIGN

2.1 Design Overview

2.1.1 Telescope Requirements

Four important scientific requirements of the telescope which dictate the optics specifications are: 1) to cover the spectral range not observable or only poorly observable from the ground from 30 μm to 1 mm; 2) to provide a collecting area much larger than now available from 1-meter size balloon-borne and airborne telescopes for high resolution far-infrared spectroscopy; 3) to provide a major advance in far-infrared spatial resolution; and 4) to take advantage of the potential sensitivity obtainable from the low thermal background at balloon altitudes. The optics specifications resulting from these requirements are given in Table 2.1-1. The resulting preliminary design is in Figure 2.1-1.

The 3-meter aperture provides the required large step in collecting area and spatial resolution, and is the largest size compatible with current U.S. balloon launch facilities. The spectral range and angular resolution requirements imply diffraction-limited optical performance at a wavelength of 30 μm. This means a half-power full-width of the central diffraction fringe of 2.5 arcseconds, which determines the acceptable image blur from optical design aberrations, misalignment, and fabrication errors. Conventionally, with optical (visible light) telescopes, this is taken to mean total effective rms surface errors of 1/26 of the wavelength. This yields a Strehl ratio (the ratio of the peak intensity of a point source to that produced by an ideal diffraction pattern) of 0.8. For radio telescope design, the rule of thumb is to require a surface half as accurate yielding a Strehl ratio of 0.5. Thus we interpret a 30-μm diffraction-limited performance to mean an image diameter (HPFW) of 2.5 arcseconds and a total surface error of 1- to 2-μm rms. Since much of the most important science done on this telescope will come from observations at 50 and 100 μm and beyond, the 2-μm rms surface accuracy appears adequate.

The specification for operation at visible wavelengths is determined by the desire to use the main telescope to image stars for guiding purposes. This places additional constraints on the character of the optics surface error and polish. We intend to make every effort to meet this constraint and will relax it only if it cannot be achieved at reasonable primary mirror cost.

The unvignetted infrared field of view of 5 arcminutes is chosen to provide two full Airy disk diameters (diameter to the first diffraction zero) at the longest wavelength of operation (1 mm).

Table 2.1-1. Telescope and Gondola Specifications

Aperture	3 Meters
Spectral Range	Visible to millimeter
Optics Design	Cassegrain
Cassegrain Focal Ratio	f/13.5
Back Focus	140 cm
Interoptic Spacing	350 cm
Angular Resolution	Diffraction limited to 30 μm (Rayleigh Criterion: 2.5")
Field of View	IR: 5' unvignetted with $\pm$ 2.5' chop, and diffraction spillover at 1 mm. Secondary is the aperture stop of the telescope. Optical: 15' vignetted only by the primary.
Secondary Chopper (Cross elevation chop)	16 Hz at 5-8 arcminutes (max.) 2 Hz at 5 arcminutes (goal) 20% deadtime (6 ms) in observing at 16Hz Secondary settable to ~3% of total throw Secondary position repeatable to 0.25" Secondary position drift less than pointing stability over an hour. Chop axis rotation settable to 1° Secondary focus motion settable to 10% of depth of field
Pointing Stability	Inertial Mode 1 arcsec rms as maximum with 0.25 arcsec as a goal. Drift corrected within above error. Magnetometer mode $\pm$10 arcminutes azimuth, $\pm$5 arcminutes elevation with $\pm$1/2° max. offset in both axes of true celestial position correctable after first acquisition.
Slew Rate	10 arcminutes/sec

Table 2.1-1 (continued)
Telescope and Gondola Specifications

Raster Scan Rate	24 arcseconds/sec max.	
Roll Compensation	None	
Max. Offset Capability	TBD arcminutes	
Telescope Observing Range Azimuth	360°	
Elevation	-10° to +65°	
Cross Elevation	± 3°	
Power System		
	Gondola	Experiment
Total Energy Storage	250 amp hrs.	250 amp hrs.
Bus Voltage	28 VDC^{+5V}_{-1V}	28 VDC^{+5V}_{-1V}
Max. Current	15 amps @ 28 V	15 amps @ 28 V
Battery Type	Lithium	Lithium
Gondola		
Max. Useful Flight Time	10 hours	
Float Altitude	29-31 km	
Weight	2,168 kg (4,780 lbs.)	
Mirror Protection	Motor-driven nylon curtain	
Telescope Protection/ Refurbishment Approach	Crash rings and crushable pads Modular assembly with spare modules	
Aspect System		
Wide Field of View Camera	~5° Full Field	
Sensitivity	11th magnitude	
Type	Intensified CCD (Fairchild model CCD 3000)	
Display	Real-time TV on ground	
Medium Field of View Camera		
Sensitivity	11th magnitude	
Type	Intensified CCD (Fairchild CCD 3000)	
Display	Real-time TV on ground	

Table 2.1-1 (continued)
Telescope and Gondola Specifications

Focal-Plane TV FOV	15' x 20'
Type	Intensified CCD (Fairchild CCD 3000)
Display	Real-time TV on ground
Star Tracker FOV	1°
Type	Intensified CCD/Strapdown
Accuracy	0.25 arcseconds in one-second integration time
Sensitivity	10th magnitude stars
Thermal Control System	
Telescope Operating Temp.	-40° ±10°C
Mirror Cooling/Heating	Convective-Passive
Mirror Stabilization Time	<1 hour
Electronics Bay and Experiments	Controlled emittance coatings and thermostatically controlled heaters.
Command and Telemetry System	
Number of IRIG User Channels	6
Useful Range (km)	To limit of standard NSBF telemetry
IRIG Operating VCO Channels Available	1, 3, 5, 7, 8, 9, 10, 11, 12, B, E, H, HH.
Experiment Accommodation	
Experiment Power	140 watts typ.
Experiment Weight	115 kg typ.
Mechanical Interface	See Section 4.4

ORIGINAL PAGE IS
OF POOR QUALITY

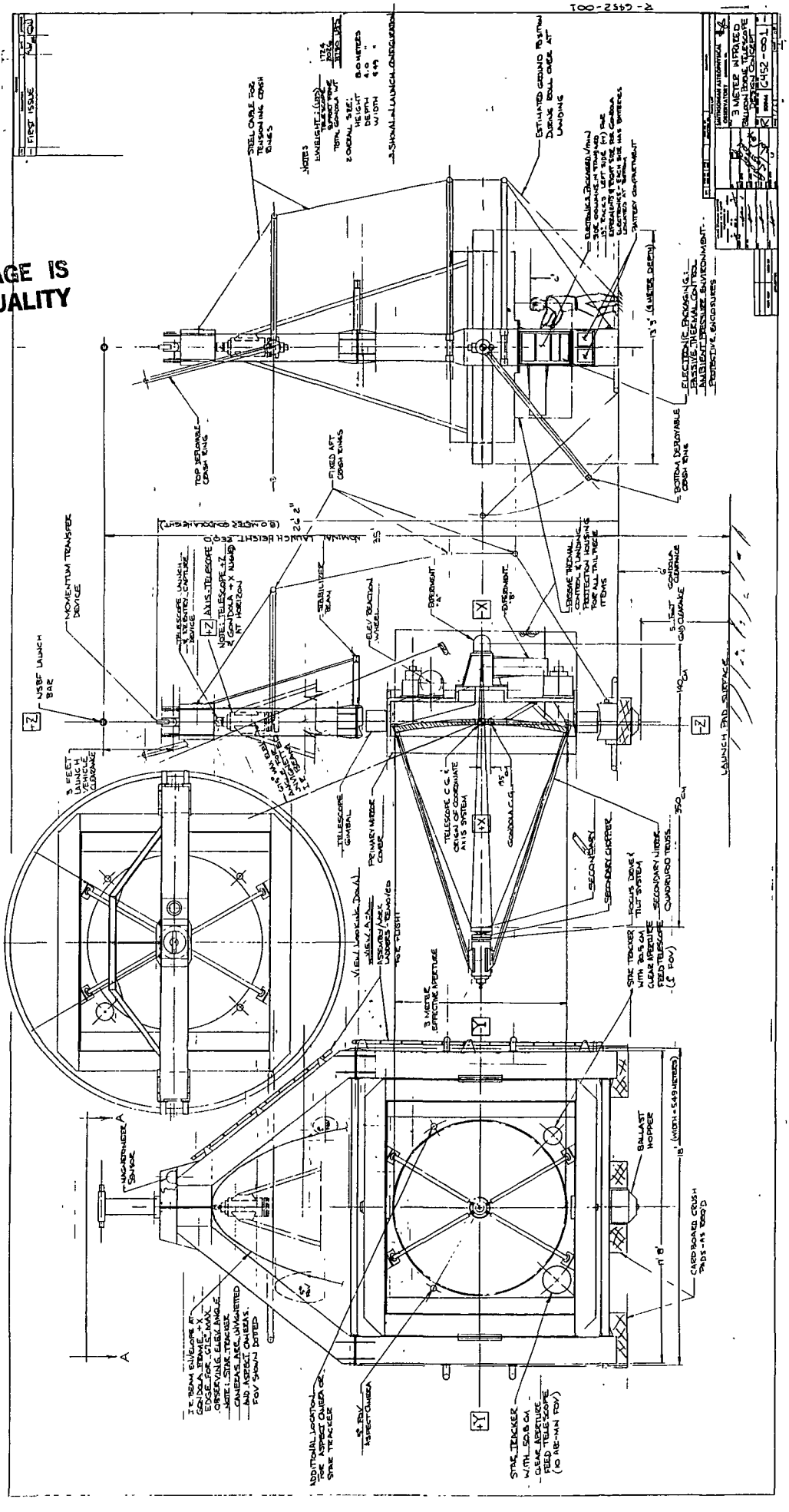

Figure 2.1-1. OVERALL VIEW OF GONDOLA AND TELESCOPE

Achieving maximum possible sensitivity requires an effective noise-free mechanism for subtracting the thermal background due to the telescope and sky from the observations. The most successful technique to date for doing this is beam switching by oscillating the second mirror through an angle either with a square wave or a linear scan. While the use of arrays of detectors in the far infrared may provide an alternative background subtraction technique for some observations, the secondary chopper still appears necessary for this telescope. Maintaining quality images while tilting the secondary places major demands on the optical design.

A second aspect of the high sensitivity requirement is minimizing the thermal emission of the telescope by minimizing obscuration from the secondary mirror and the secondary mirror support structure and maintaining very low emissive surfaces on the optics. Both the chopper and the low obscuration requirements dictate a small secondary mirror.

The launch equipment and staging facilities at the NSBF dictate the overall size of the telescope and, in particular, the maximum acceptable primary-to-secondary vertex separation.

2.1.2 Pointing Requirements

The pointing and structural specifications shown in Table 2.1-1 are dominated by the 30-μm wavelength beam size, the slewing and scanning requirements, the maximum allowable gondola weight, the thermal environment, and the operational requirements of balloon flights. The pointing stability specification of 1-arcsecond rms is set so as not to compromise the imaging quality of the optics. An estimated pointing error of 0.89 arcseconds is projected as shown in Table 2.1-2.

Table 2.1-2. Pointing Error Budget

Error source	Allowable error Arcseconds
Pointing servo system	0.15
Telescope Structure	0.6
Star tracker	
Resolution	0.1
Coalignment	0.2
Coalignment stability	0.6
RMS pointing error	=0.89

The telescope is suspended in gimbals within the gondola frame and is oriented in two orthogonal control axes, elevation and cross-elevation. Telescope motion in the cross-elevation axis is limited to about $\pm 3°$.

Coarse azimuthal control is achieved by rotating the entire gondola at its attachment point to the balloon.

Aspect data is provided by three television cameras of differing focal length and field of view and a star tracker. All use well developed CCD technology. Star tracker aspect capability is approximately 0.2 arcseconds. Television presentation of the aspect fields during the flight will provide continuous assurance to the ground crew of correct pointing and pointing stability.

2.1.3 Structural Requirements

The total gondola weight limit of 2,268 kg (5,000 lbs.) has led to a composite material telescope structure with a quadrupod secondary support. The quadrupod is load bearing during launch, termination and landing. A ball-and-socket type lock captures the telescope structure and applies a tension load between it and the gondola during these flight phases. All NSBF safety requirements can be met, however, with the telescope unlocked. Reaction wheels on the telescope and near the azimuth bearing provide the required inertial references for the pointing system.

Requirements for telescope and instrument integration, launch and recovery were major drivers of the proposed design. Gondola recovery in particular led to a modular design approach which is easily refurbishable by means of replaceable elements.

2.1.4 Support System Requirements

Allowable instrument weight, volume, power, command and telemetry capabilities will meet the requirements of a wide range of potential users. The instrument area has been designed for ease of instrument mounting and alignment and is enclosed in a thermal shroud before launch.

The command and telemetry system is designed for compatibility with present and planned NSBF capability. Battery types and capacities were chosen on the basis of price and weight tradeoffs. Sufficient energy is available for flights in excess of 10 hours with the baselined gondola systems and experiment complement.

2.1.5 Operating Mode Requirements

Acquisition of a celestial source is achieved through two modes of operation that are called the Magnetometer and Inertial Modes. The Magnetometer Mode is used for acquisition and coarse positioning within the celestial field. This is accomplished by rotating the gondola about the azimuthal axis, using the Earth's magnetic field as reference, to a positional accuracy of about 30 arcminutes. Telescope rotation about the elevation axis, using the gondola gravitational alignment as reference, to

a positional accuracy of about 10 arcminutes brings the desired source direction within the range of motion of the cross-elevation axis. The Inertial Mode is used for science-data gathering. In addition to fixed pointing, which stabilizes the telescope on a given celestial target, the inertial mode can also be used to step or scan the telescope with respect to a celestial object. For mapping of extended sources a raster pattern can be generated by scanning in cross-elevation and stepping in elevation at the end of each scan line. The angular size of such rasters and the scan rates can be varied on command. In addition to the commanded scan rates and directions, a joystick control at the ground station can be employed for telescope positioning.

2.2 Telescope Design

2.2.1 Description of Selected System

a) Optics Design

Figure 2.2-1 illustrates the design of the telescope optics and specifications. The optical design is based on third order analytic aberration theory as presented by Gascoigne (1973). The telescope is a classical Cassegrain with a paraboloidal primary and hyperboloidal secondary. The secondary is undersized relative to the primary so that it acts as the optical stop of the system. The undersizing is selected so that for the full field size, the maximum chop amplitude, and the full diffraction width (diameter of Airy disk first zero) at the maximum design wavelength (1 mm) the field of view of a detector at the focal plane will "see" only the secondary, the cold sky, and the primary, but not the warm periphery of the primary.

The minimum wavelength and associated diffraction HPFW determines the diffraction-limited performance of the telescope. The maximum HPFW is defined at the longest wavelength expected to be used. The diffraction size of the beam at this wavelength contributes to the required secondary undersize. The secondary undersize ratio is set to assure that it is the pupil stop of the telescope for all normal use.

The optical design parameters are chosen to provide no spherical aberration or other third order aberrations in the image at the nominal focal plane on axis. Figure 2.2-2 shows how the coma, astigmatism, and field curvature affect the image size as a function of field radius. Figure 2.2-2 also gives the misalignment image blur due to secondary chopper tilt as a function of image displacement in the focal plane. The chop angle (in terms of focal-plane displacement), back focus, and field radius for which the image blur is 1 arcsecond in size are also given in Table 2.2-1. The greatest image degradation comes from the chopper tilt. This is a basic problem for this method of sky subtraction with a fast primary Cassegrain telescope. Shown on the chopper blur curve in Figure 2.2-2 are points for a Strehl ratio of 0.9 at 30 μm wavelength and 2.5 arcminutes chopper amplitude. For this telescope the image diameter equals the 30-μm Airy disk full diameter of 5.3 arcseconds at a chopper focal-plane displacement of 1.7 arcminutes, for which the Strehl ratio is 0.9. At a chopper field amplitude of 2.5 arcminutes, the Strehl ratio is 0.9 at 44 μm. Thus, for a Strehl ratio of 0.9 (coma length equals Airy disk full diameter) at all wavelengths the maximum focal-plane displacement due to secondary chopper tilt is 40 resolution elements (1.22 λ/D).

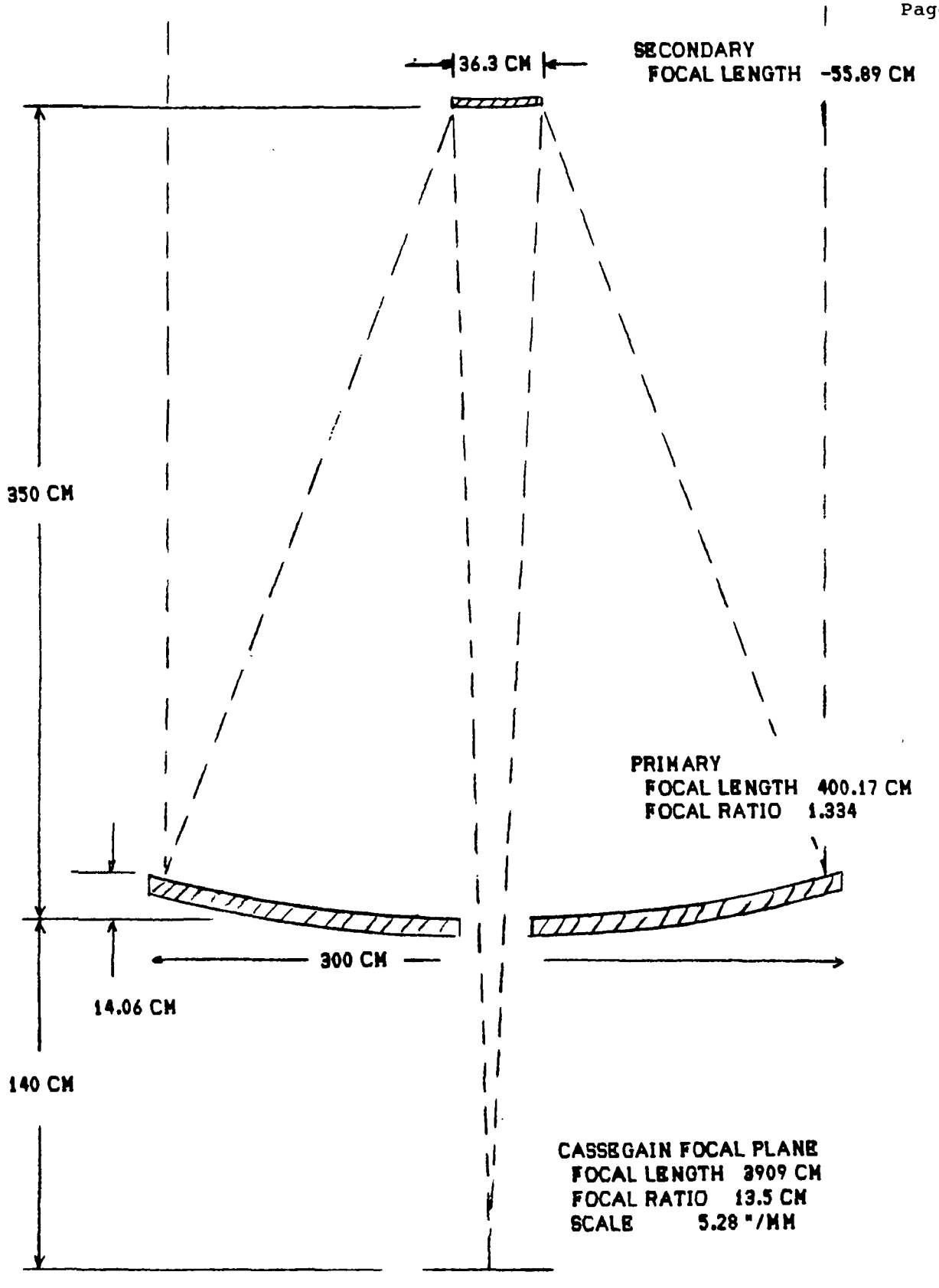

Figure 2.2-1. Optical Design

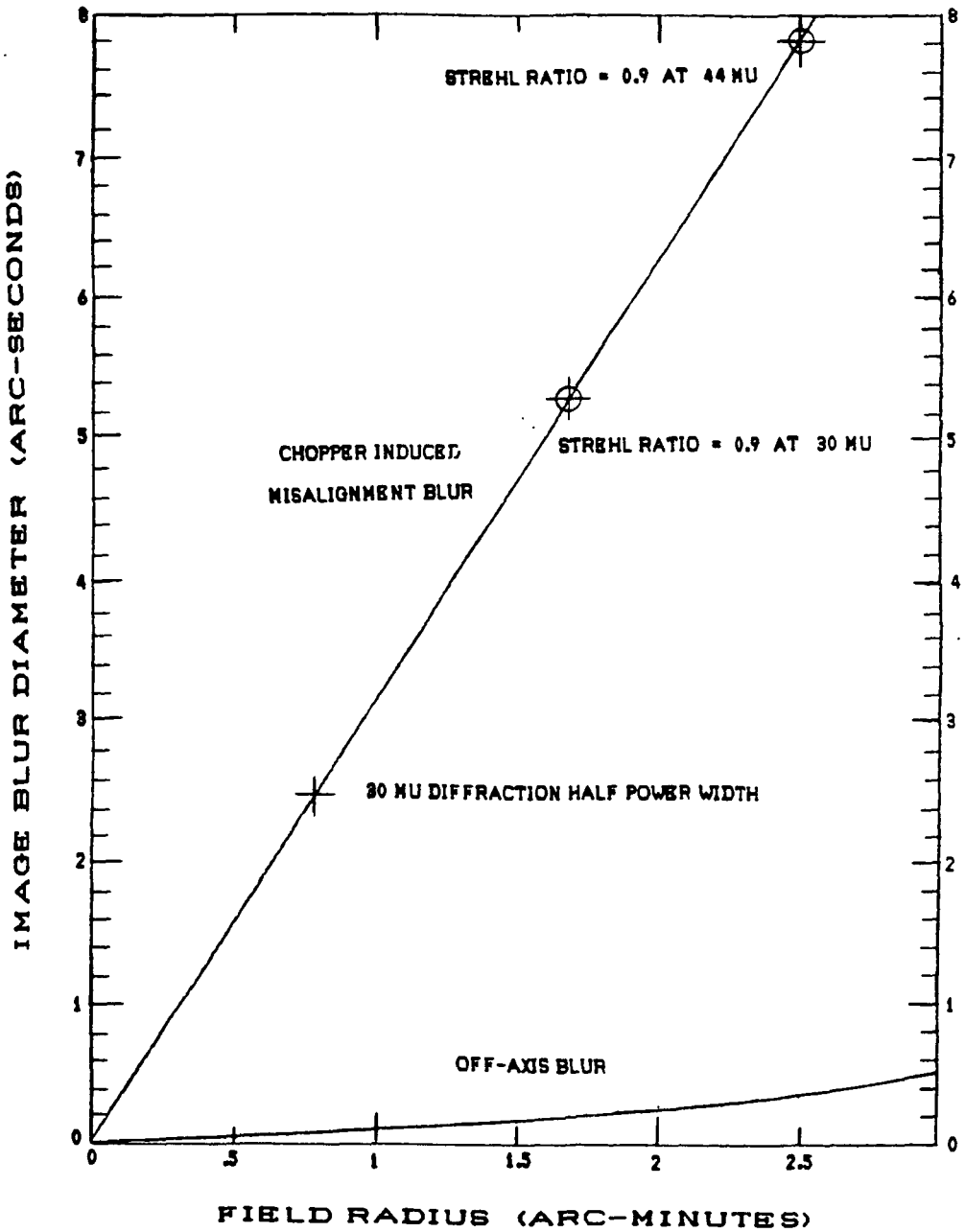

Figure 2.2-2. Image Blur vs. Field Position and Chopper Angle

Table 2.2-1. Telescope Optics Design and Performance

Aperture (cm)	300
Cassegrain focal ratio (f/)	13.5
Primary secondary separation (cm)	350
Primary focal-plane separation (cm)	140
Field radius (')	2.5
Chop field amplitude (')	2.5
Minimum wavelength (μm)	30
Maximum wavelength (μm)	1000
Diffraction HPFW min (")	2.6074
Diffraction HPFW max (')	1.4486
Secondary undersize	.03491
Cassegrain focal length (cm)	3908.6
Focal-plane scale ("/mm)	5.2771
Primary focal length (cm)	400.17
Primary focal ratio (f/)	1.3339
Primary sagitta (cm)	14.057
Primary departure from sphere (cm)	.12567
Secondary diameter (cm)	36.296
Secondary focal length (cm)	-55.89
Secondary conic constant ($-e^2$)	-1.508
Secondary sagitta (cm)	1.4634
Secondary departure from sphere (cm)	.00946
Secondary axial magnification	-96.40
Secondary angular magnification	.25073
Range for 1" blur	
Chop (')	.31966
Back focus (cm)	14.204
Field coma (')	15.089
Field astigmatism (') quadratic	14.338
Field curvature (') quadratic	4.4708

b) Alignment Tolerances

The above design and the desire for a 2.5-arcsecond beamwidth determine the acceptable alignment tolerances for the secondary tilt, decenter, and axial motion. This includes both initial alignment when the gondola reaches float altitude and the stability of alignment during observing. Initial alignment has far greater tolerances than alignment stability because of the adjustments which can be made in secondary axial motion (focus) and secondary tilt after the gondola reaches float.

Meinel has pointed out that precision centering of the secondary of a Cassegrain telescope is not essential. The miscollimation coma created by a secondary decenter can be corrected for by a compensating secondary tilt. For this reason this telescope requires only a remote controlled secondary tilt adjustment, not a centering adjustment, for adjusting the collimation

of the telescope after it reaches float altitude. This adjustment can best be made by observing the symmetry of the aperture illumination with an out-of-focus image of the bright star utilizing the focal-plane tracking camera.

c) Initial Alignment

With the exception of decenter, the primary basis for the optical stability tolerance requirements on reaching float altitude is the necessity of insuring rapid and efficient alignment of the telescope at the beginning of observation. It is necessary to have a star image appear in the field of the main focal-plane camera when it is centered on the boresighted acquisition guide telescope and to have telescope focus close enough to correct the result in a detectable star image. The decenter tolerance is limited by the amount of decenter that can be compensated by secondary tilt before the resulting tilt of the focal plane blurs images at the edge of the field of view unacceptably.

With regard to decenter, we have assumed that the initial defocus results in an image four times the full diameter of the 30-μm central tolerance diffraction fringe, that is, 20 arcseconds; and tilt and decenter result in a coma of 10 arcseconds. Also, we have assumed an angular offset due to initial tilt and decenter equal to the focal-plane infrared camera field radius, 2.5 arcminutes. Finally, the initial decenter is limited by requiring an image defocus blur of less than 1 arcsecond at the edge of the field due to focal-plane tilt after secondary tilt compensation. The resulting initial tolerances are given in Table 2.2-2.

If there is a predictable and repeatable focus shift from ground to float altitude, it can be removed by the initial focus setting. For example, a carbon-fiber-reinforced plastic secondary truss support with a coefficient of thermal expansion of 2×10^{-6} °C will result in a secondary defocus motion of 0.56 mm due to a temperature change of 80°C from ground to float altitude*. The tolerances in Table 2.2-2 cover the remaining mechanical and thermal uncertainties of such a correction. They should be treated as maximum tolerances. Smaller errors will result in faster telescope realignment during the flight.

The expected temperature change from ground to float altitude will actually be about 65°C.

Table 2.2-2. Telescope Optics Alignment Tolerances

Alignment for 1" blur	
Secondary decenter (cm)	-.0186
Secondary tilt (')	-1.275
Secondary axial motion (cm)	.00256
Alignment for 1" motion	
Secondary decenter (cm)	-.0022
Secondary tilt (')	.06647
Initial Alignment	
Secondary defocus for 20" blur (cm)	.05122
Secondary decenter for 10" coma (cm)	.18605
Secondary decenter for 1" corrected blur	.42856
Secondary decenter for 2.5' motion (cm)	.32420
Secondary tilt for 2.5' motion (')	9.9709
Secondary tilt for 10" coma (')	12.749

d) Operating Alignment Tolerance

The operating tolerances for secondary tilt, decenter, and axial motion each defocussing the image by 1 arcsecond are also given in Table 2-2.2. These tolerances are for telescope stability between realignment on a reference star, an activity which should take place as little as possible during the flight. The defocus blur is minimized by refocussing on a bright star. The decenter blur can be corrected by examining an out-of-focus star image and tilting the secondary to restore collimation. The decenter and tilt shift tolerance affect the stability of the bore sighting with a tracking telescope. If the gyros are updated by images in the main telescope these tolerances can be substantially relaxed.

2.2.2 Optics Design Tradeoffs

a) Tradeoff Approach

The telescope design is constrained by our desire to provide as large an aperture as possible within the capability of the National Scientific Balloon Facility. This maximum aperture is approximately 3 meters. In addition the overall secondary vertex-to-Cassegrain focus distance is constrained by the launch facilities to approximately 4.9 meters. In the design study we have chosen as the variable parameters the aperture, Cassegrain focal ratio, primary-secondary separation, and primary-to-focal-plane distance. We have considered the required field radius, chopper field amplitude, and maximum operating wavelength to be fixed. The tradeoff studies investigate the impact of varying the input parameters on the focal-plane scale, primary focal ratio, secondary obscuration, chopper-induced aberrations, field aberrations, and alignment tolerances. These impacts are examined for five different values of each of the four parameters while the other three are held fixed at the chosen design values. The calculations are based on the third order analytic aberration referred to

in Section 2.2.1. Appendix A displays the results of these calculations.

b) Interpretation of Tradeoffs

Figures 2.2-3 through 2.2-6 display the variation of several important optical characteristics over the range of the four tradeoff parameters based on the data in Appendix A. On each of these graphs the nominal design values are circled.

The maximum values for the aperture and the secondary vertex-focal-plane distance are limited by the launch and staging capabilities of the NSBF and are basically the values of the chosen design. Hence, Figure 2.2-3 shows primarily how the optical performance improves and tolerances are relaxed if the telescope's specifications are reduced to a smaller aperture and Figure 2.2-5 indicates the impact on the optical performance and alignment tolerances of a reduction in the overall length of the telescope. The advantage of the latter would be to simplify the telescope structure design and reduce its weight. Figure 2.2-6 gives the primary vertex-to-focal-plane (back focus) tradeoff. The back focus distance is constrained both by instrument requirements and telescope balancing requirements. Because of balance requirements, the parameter held constant for the back focus tradeoff is the overall secondary vertex-focal-plane distance rather than primary-secondary distance. The Cassegrain focal ratio is the parameter least constrained by mechanical and operational requirements.

The significance of the items plotted for the telescope performance is as follows:

Five-Arcminute-Field Diameter. This determines the minimum possible size of the instrument dewar window and the scale of the instrument cold optics and is especially important at the longest wavelengths where even a small number of elements of an imaging array cover the full five-minute-diameter field. Thus, the field diameter should be as small as possible.

Primary Focal Ratio. Optically ground and polished, paraboloidal primary mirrors of large size have been made only to f/2. New methods utilizing a computer controlled flexible lap promise to extend this to much shorter focal ratios. Replicated primary mirrors have been fabricated with focal ratios as short as f/.35. In general, the larger the primary focal ratio, the easier the fabrication and testing of the primary is, although this is not considered a major constraint for this tradeoff.

Secondary Diameter. The secondary obscuration which impacts the effective emissivity of the telescope increases as the square of the diameter. The secondary moment of inertia that dominates the secondary chopper performance increases as the fourth power of the secondary diameter. A major driver for the telescope is to keep the secondary as small as possible.

Back Focus Range. Since instruments are to be designed for operation at the design focus, the back focus range is not a significant consideration.

Field Angle for One-Arcsecond Blur. The field aberrations are well within the specifications for image blur at the specified 5-arcminute infrared field diameter for all designs. The field aberrations are dominated by the

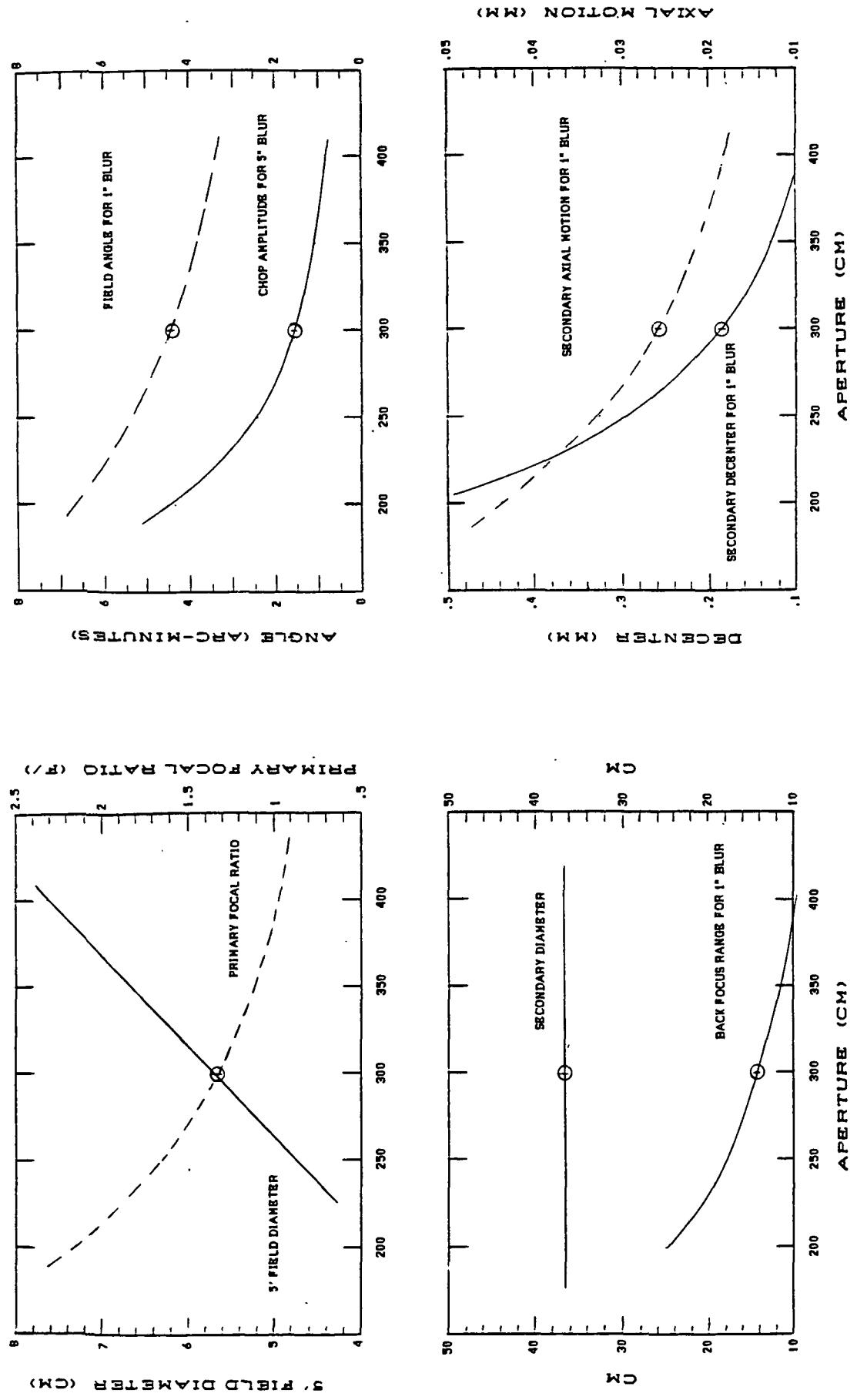

Figure 2.2-3. Aperture Tradeoff

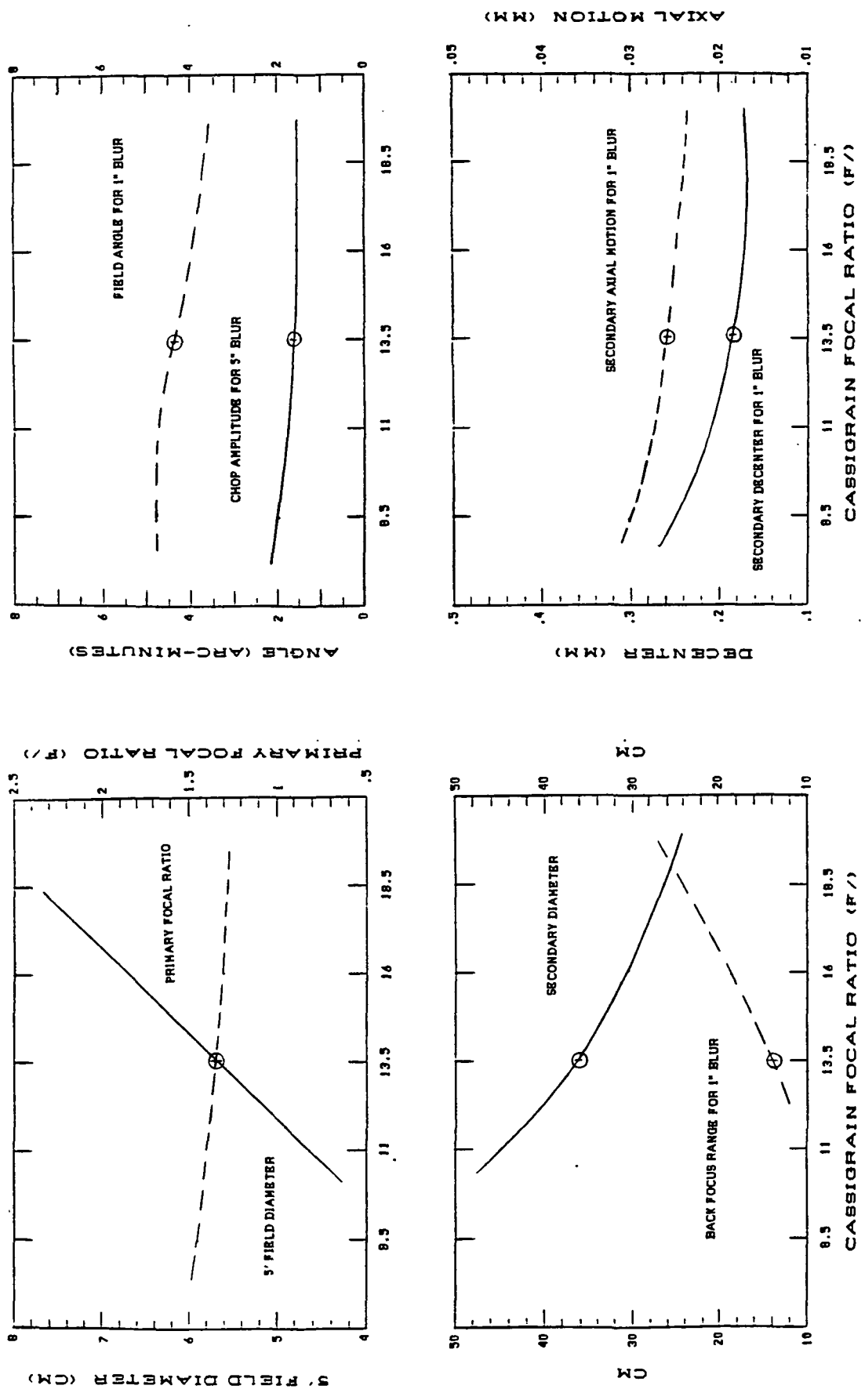

Figure 2.2-4. Cassegrain Focal Ratio Tradeoff

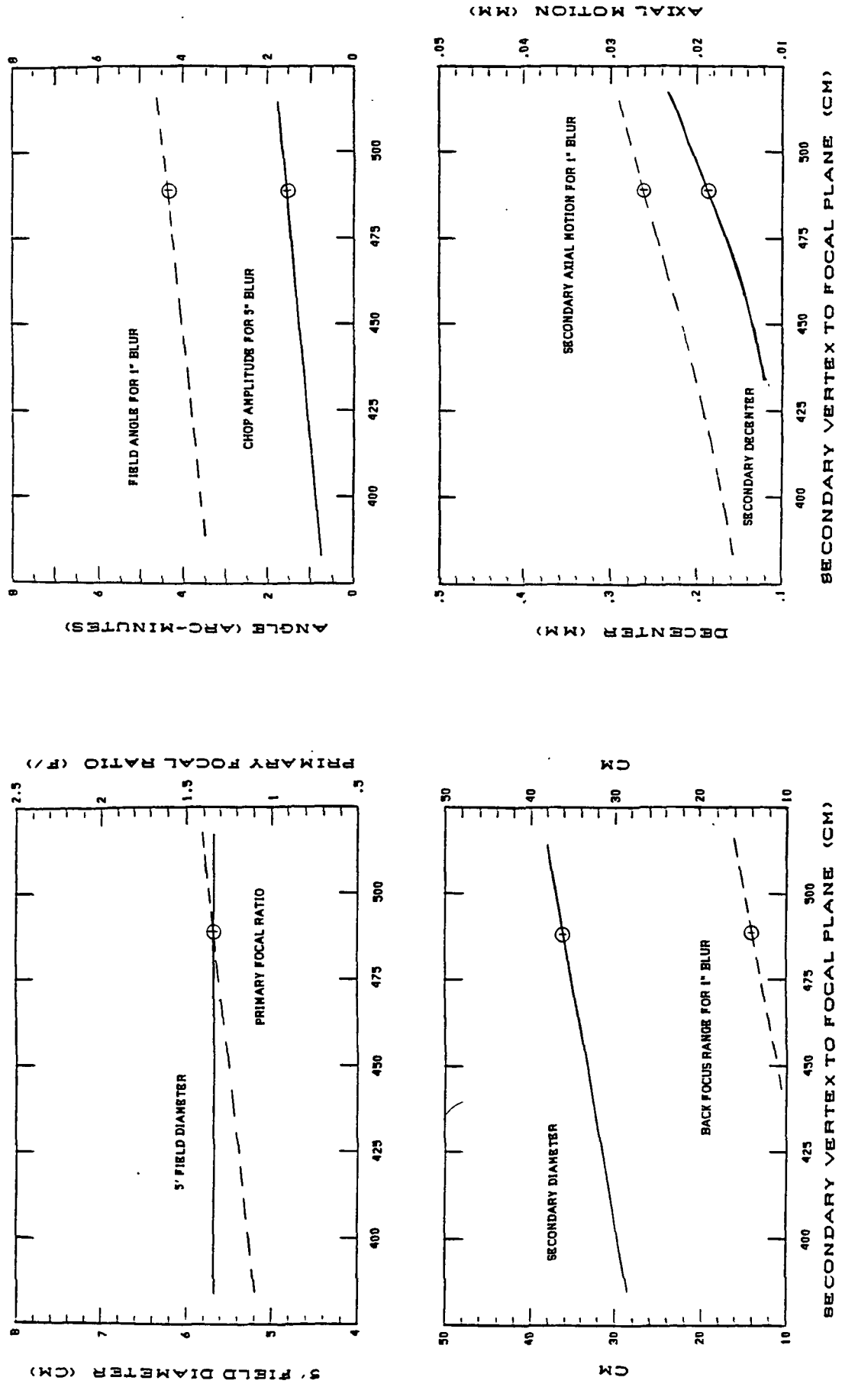

Figure 2.2-5. Overall Length Tradeoff

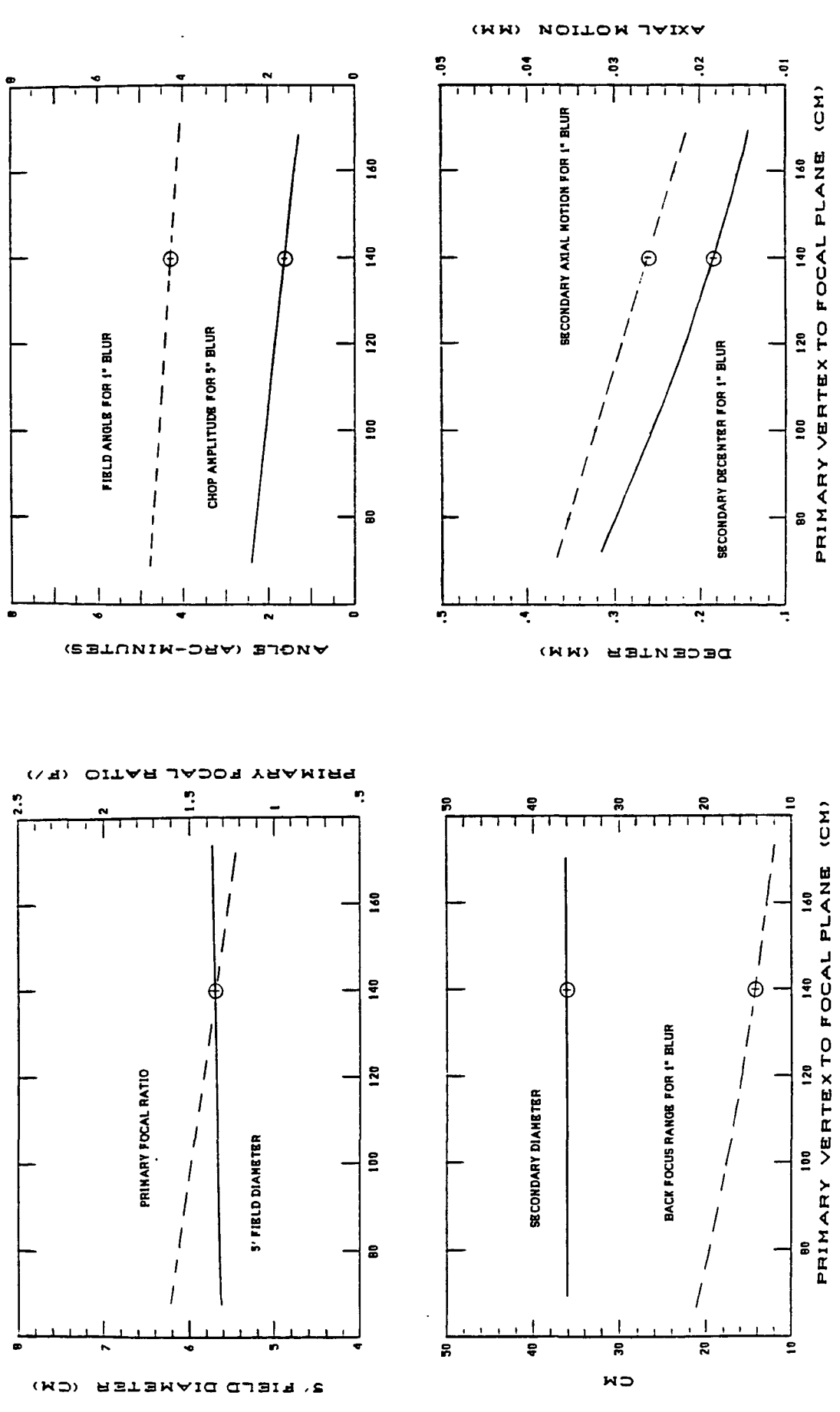

Figure 2.2-6. Back Focus Tradeoff

field curvature. For the specified visible field of view of 15-arcminutes diameter, the image blur in arcseconds is given approximately by the square of the ratio of 7.5 divided by the field angle in Figures 2.2-3 to 2.2-6.

Chop Amplitude. Chopper-induced coma is by far the largest optical aberration of the telescope. The chopper amplitude which produces a five-arcsecond coma length is plotted because this is the coma for which the Strehl ratio is 0.9 at a wavelength of 30 μm for a three-meter telescope. As can be seen from the tradeoff study figures, the nominal design provides this image quality only to a chopper angle of 1.7 arcminutes and, hence, does not meet the desired specification for image quality to a chopper amplitude of 2.5 arcminutes at 30 μm. As was shown in Section 2.2.1, it does meet the requirement of a Strehl ratio of 0.9 at 44 μm. Hence, the chopper-induced image blur is a critical item to minimize over the tradeoff range.

Secondary Axial Motion for One-Arcsecond Blur and Secondary Decenter for One-Arcsecond Blur. These two items indicate the tolerances the telescope must maintain during observations without refocussing or adjusting the secondary tilt to compensate for decenter. The one-arcsecond blur is intentionally taken to be a small fraction of the Airy disk in order that this item be small compared to the potential chopper-induced blur. While it appears from the mechanical design analysis that these tolerances are acceptable and can be met, clearly tradeoffs that increase the tolerances are preferable.

c) Conclusions

The most critical goals of the design tradeoff are in descending order of priority:

1. Minimize the secondary diameter.

2. Maximize the chopper amplitude for which the comatic blur is 5 arcseconds.

3. Minimize the size of the 5-arcminute field diameter at the Cassegrain focus.

These impact the free parameters as follows:

1. Aperture. Reducing the aperture improves all performance aspects with the exception of the secondary diameter, which stays the same and, hence, becomes a larger fraction of the overall aperture. Thus, if the aperture were to be decreased it would be desirable to reduce the overall length as well in order to reduce the secondary diameter correspondingly.

2. Cassegrain focal ratio. This should be small for maximum chopper amplitude and minimum field size. It should be large for minimizing the secondary diameter. A focal ratio of f/13.5 is a compromise choice.

3. Overall length (secondary vertex-focal plane). Reducing this reduces the secondary diameter but produces a smaller chopper amplitude for a 5-arcsecond blur. It has no effect on the field diameter. The chosen design is based on the largest possible overall length for the NSBF.

4. Back focus (primary vertex-focal plane). Reducing the back focus improves the chopper amplitude and the field diameter and has no effect on the secondary diameter. The smallest back focus is best for the optical performance. The design value is chosen primarily for telescope balance reasons.

2.2.3 Telescope Mechanical Design

The optical design characteristics and optical positioning tolerances were given in Tables 2.1-1 and 2.2-2. The telescope mechanical design is aimed at achieving these optical positioning requirements in an efficient manner.

Primary Mirror and Cell. The primary mirror cell serves as a pedestal from which to erect the telescope including its aspect cameras, stabilization components, mirror protection cover and experiments. Table 2.2-3 lists the major telescope components along with their expected weights. The primary cell will be a monocoque structure fabricated from graphite-epoxy composite in a fashion similar to that proposed for the primary mirror. This affords maximum structural stiffness per unit of weight while minimizing mirror distortions created by temperature-induced differential expansions between the mirror, its mounting system, and the cell. The cell is directly attached to the cross-elevation gimbal via a set of centrally aligned flexpivots. This interface is insensitive to temperature effects between cell and gimbal. The mirror cell also provides mirror mounting and protection while serving as a base for the secondary truss. The primary mirror mounting technique will most likely follow techniques developed by Dornier-System GmbH for mounting large-diameter graphite-epoxy millimeter wavelength radio astronomy telescope primary reflectors.

Mirror protection is accomplished in two ways. First, the mounting cell has a forward skirt that protrudes beyond the mirror, thereby placing the mirror in a protective cavity. This skirt can be removed to provide access for mirror mounting. Second, a retractable mirror cover, presently conceived as a rolled curtain of strong plastic woven mesh, is mounted on the skirt. The cover will be used during testing and during recovery to prevent tools, telescope components, tree branches, and the like from striking the mirror.

The quadrupod secondary mirror truss mounts at four points just forward of the primary mirror. This is a departure from the standard infrared telescope design of a circular head ring with four thin secondary vanes and was chosen to minimize the overall gondola weight while guaranteeing the positional accuracy required by the optical design. The telescope truss is designed to place the natural vibrational frequencies of the truss well

beyond the pointing and stabilization servomechanism systems' bandpass to minimize coupling sensitivity to secondary chopper motion and other vibrational inputs.

The truss design:

- Is weight-efficient.
- Allows secondary mirror system optical alignment.
- Maintains optical positioning for 1-g load variations and thermal excursions.
- Has all natural resonant frequencies $\geq$80 Hz.
- Can be disassembled for recovery and transport.

Table 2.2-3. Three-Meter Telescope Subassembly Weight Summary

	Subsystem	Weights (Lbs.) Unit Weight (lbs.)	
I.	Secondary Mirror Assembly		
	Mirror	10	
	Focus Drive	22	
	Chopper	25	
	Tilt System	5	
	Truss & Attachments	125	
			187
II.	Primary Mirror Assembly		
	Mirror	234	
	Mirror Cell	400	
	Mirror Cover	51	
	5^{o} FOV Aspect TV	15	
	1^{o} FOV Star Tracker	35	
	10' FOV Star Tracker	55	
	Cross Azimuth Servo	20	
	Miscellaneous	20	
			830
III.	Cross-Elevation Axis (X-Elev)		
	X-Elev Drive System	80	
	Elev Drive System	50	
	Gimbal Frame	140	
	X-Elev Reaction Wheel	25	
	Elev Reaction Wheel	25	
	Electronic Interface	10	
	Wire Harness	10	
	Miscellaneous Devices	25	
			365
IV.	Experiment Package		
	Tailpiece	50	
	Experiment A	125	
	IR Camera	50	
	Experiment Selector	12	
	Combined Electronics	100	
	Trim Weights	5	
			342
	Total Telescope Weight		1724 lbs. (782 kg)

A telescope of three-meter aperture of head ring design would be heavier by about 68 kg than the proposed quadrupod design because of the amount of material required to fabricate the head rings and secondary support vanes. Also, the head ring creates a large rotational moment which must be balanced with additional weight behind the primary in order to maintain a "zero moment" pivot point near the primary mirror vertex. The higher weight of the head-ring design would similarly ripple throughout the entire gondola design since it would necessitate increased load carrying capability in all structural members, larger drive motors in the mechanisms, additional battery power, and so forth.

The secondary mirror assembly truss mounting must allow positioning of the secondary to ≤ 0.002 cm and support re-entry loads without failure. Secondary mounting designs of similar characteristics have been developed for ground-based telescopes and should not pose any technical problems for this program.

The telescope is capable of making observations from 10 degrees below the horizon to an elevation of 65 degrees. The truss must therefore maintain the position of the secondary mirror over this observational range. The gravity load vector will change as the sine of the elevation angle. The truss deflection can be calculated using the virtual work method developed by Norris (1960).
The formula used is:

$$\alpha = \sum_{1}^{N} \frac{F_p \cdot F_Q L_i}{A_i E_i}$$

where:

α = deflection (inches)

F_p = force in member due to load (pounds)

F_Q = force in member due to one pound virtual load (pounds)

L_i = truss support length (inches)

A_i = cross-sectional area of member (inches^2)

E_i = Young's modulus of elasticity (pounds per inch^2)

N = truss members

The use of direction cosines allows determination of the truss member length and support angles with reference to the optical axis once each end is defined by rectilinear coordinates. In our case, the member length is 171 inches and angles of interest are 20.12° for gravity axis deflections and 10.9° for chopped axis deflections. Also, the expected member lowest natural frequency is taken as:

$$f_n = \frac{3.55}{\sqrt{\frac{W\ell^3}{768EI}}}$$

where: E = Young's modulus (pounds - in^{-2})

I = Inertia ($inches^4$)

W = Member weight (pounds)

ℓ = Member length (inches)

The truss structural characteristics then were calculated to be:

Natural frequency, gravity axis	$\geqq$110 cps
Natural frequency, chopped axis	$\geqq$119 cps
Natural frequency, individual member	$\geqq$75 cps
1 g deflection (zenith to horizon)	8×10^{-4} in ($\geqq 2 \times 10^{-3}$ cm)
Gravity deflection Hr^{-1} at fixed pointing	2×10^{-4} in ($\approx 0.5 \times 10^{-4}$ cm)

The truss is also subjected to a large thermal excursion from launch to altitude with a small fluctuation occurring at altitude. A temperature difference of 54°C (130°F) and ±5.6°C (±10°F) fluctuation was used to determine the material characteristics required to minimize the need to actively refocus the telescope during an observation. This requirement mainly influenced the selection of graphite-epoxy as the truss material, although its strength-to-weight ratio and natural damping qualities are also highly desirable. The temperature defocus was calculated to be 0.018 cm over this range which implies an in-flight defocus equal to 0.0015 cm. These values are attained by using a coefficient of thermal expansion of $1.0 \times 10^{-6}/F^{\circ}$ which is conservative for this material.

2.2.4 Telescope Thermal Design

a) Basis for Design

Minimizing telescope distortion induced by the adverse thermal environment at float altitude is the major criterion for thermal design of the Three-Meter Balloon-Borne Telescope. Active control of telescope optics and structure at the original launch ambient temperature during flight is impractical because of the complexity of doing so and the very large heater power requirements. Fast stabilization of the telescope at a quasi-equilibrium temperature (at which heat exchange with the environment is minimized) and maintenance of this condition throughout the observation period is the primary goal of this design. Thermal gradients across the mirror face and through its thickness must be minimal, focal length must be within

tolerance, and quadrupod temperatures must be equal and stable.

The Three-Meter Balloon-Borne Telescope will utilize the enhanced convection environment of the ascent phase and the low air temperatures of the tropopause to cool critical elements to the desired temperatures, about -40°C. Although little investigation of convection conditions in a balloon environment has been reported, our own work (summarized in a later section) shows that convection coefficients on exposed surfaces of order 10 W/m^2K or greater can be expected during a large portion of ascent, and about 5 W/m^2K at float altitude.

It is readily calculated that a lightweight glass mirror of density 70 kg/m^2, with both surfaces exposed to such a convective environment of temperature 20°C below itself, will reach -40°C during ascent. Such a calculation is conservative with respect to both convection and air temperature, so there is adequate reserve cooling capability; enough, in fact, that a provision to prevent overcooling may be needed. We have also verified that radiative heat transfer in the cellular construction of a lightweight Pyrex mirror permits the mid-plane to stabilize with a time constant of less than a half hour. A composite mirror would stabilize even more rapidly because of higher thermal conductivity as demonstrated in the cooled test chamber.

During observation an exposed primary mirror would radiate to space at 10-15 W/m^2, depending on the emittance of its polished surface. However, a protective tube surrounding the optical path will reduce the solid angle of exposure to space, reducing the net radiation to 2-3 W/m^2. This radiation will be balanced by convection to the front surface from the air near the surface and by conduction and radiation from the rear surface to the front. This second mode would result in a temperature difference between front and back which would distort the figure, and must therefore be kept to a minimum by radiative and convective isolation of the back surface (coatings, insulation, or both), allowing convection at the front to dominate. It is not yet clear what the convective environment will be inside the telescope tube (partially shielded from relative motion between the gondola and surrounding air) and a scaled-down experiment is planned for the near future to help determine this.

Structural elements such as the quadrupod legs will respond to the ascent convective environment with a time constant of a few minutes. Overcooling in the tropopause will occur, and response will slow as the experiment nears float, but these elements will be within a few degrees of final temperature within a half hour of achieving altitude. At stable altitude, and therefore stable air temperature, the quadrupod will be stable as well except for changing radiative environment. Controlled-emittance coatings will be used on critical structural elements; detail design will determine whether coatings of high emittance (giving faster response but greater excursion) or low emittance (yielding the opposite) are best.

b) Flight Test of Convective Mirror Cooling

To supplement our understanding of the convective environment at balloon float altitudes we recorded special thermal measurements during a recent flight of the One-Meter Infrared Telescope. The primary mirror

(solid aluminum in this case) was instrumented, as were sections of aluminum tubing selected to simulate typical structural elements (the proposed quadrupod legs, for example) and the surrounding air temperature. We observed these temperatures as a function of time and from this data calculated approximate coefficients of convective heat transfer from the rates of temperature change of the elements and the air temperature. The simulated structural elements followed air temperature quite closely, and equilibrated in less than an hour after altitude was achieved, after which their temperatures wandered slowly over a four-degree range, probably in response to changes in radiative conditions (which were not monitored). The mirror responded much more slowly because of its much greater mass/area ratio. Calculated convective coefficients from the independent measurements agreed remarkably well, peaking at 25-40 W/m^2K at low altitude and decreasing gradually to about 5 W/m^2K at float altitude of 30km (96,000 ft), which is roughly equivalent to that for free convection at surface ambient conditions. It is clear that significant relative motion between the air and the experiment must exist to achieve such values at low air density, and suggests that surfaces protected from such relative atmospheric shear may experience much lower convection. We plan to investigate these matters experimentally on other balloon flights in the near future.

2.2.5 Chopping Technique

Telescope specifications call for a secondary chopper with a beam switching angle referred to the sky of 5 arcminutes at a frequency of 16 Hz and a dead time of 20%. The secondary mirror diameter is 36.3 cm. It will be lightweighted. Several options exist such as beryllium, glass, composite, and foamed silicon carbide.

High performance servo-controlled secondary choppers have been developed by Steward Observatory for the Multiple Mirror Telescope, by Kitt Peak National Observatory (KPNO), and by several balloon and aircraft infrared groups. The Three-Meter Balloon-Borne Telescope secondary design will take advantage of these developments. It will have a reactionless drive with high permeability core "loud speaker" type drives pushing against a reaction plate. The drive will permit remote control of the chopper throw and frequency.

Properties of the secondary chopper are given in Table 2.1-1.

2.3 Support Structure Design

2.3.1 Mechanical Concept

The Three-Meter Balloon-Borne Telescope design concept is shown in Figure 2.1-1. Two major assemblies, the telescope and support structure, form the overall gondola. The telescope design has been previously described in Section 2.2.

The support structure is a yoke frame that serves five major functions:

- Telescope structural attachment to the balloon.
- Telescope azimuthal orientation and coarse stabilization.
- Telescope elevation reference frame.
- Packaging for all electronics and gondola support systems.
- Launch, landing and recovery protection.

A yoke frame has been selected as the best method of telescope support given the NSBF size and weight restrictions previously described. The telescope weighs 782 kg (1,724 lbs.) and measures 6.0 meters along the optical axis (including experiments), 4.4 meters in width, and 4.0 meters in depth. The yoke frame requires only 335 kg (1,100 lbs.) to meet the telescope's structural load-carrying requirements while only increasing the overall gondola size to 8.0 meters in height and 5.49 meters in width with no change in depth. Deployable crash rings are needed to protect the telescope on landing. These add to the gondola's width and depth but not sufficiently to cause a handling problem with the NSBF launch vehicle or staging building.

The yoke frame is a symmetrical structure requiring six structural members for telescope support: two diagonal beams, two side columns and two horizontal stabilizers. The two diagonal beams fasten together along the line of suspension forming a cavity where the momentum transfer system and telescope launch lock are located. The side columns extend down from these diagonal beams to provide telescope attachment at the elevation axis, and then extend beyond this attachment to provide cavities in which to package electronics and to provide a landing structure (see Figure 2.1-1). The electronics systems will be separated such that all gondola electronics are in one side column and all experiment systems in the other. Electronics include batteries and NSBF command and telemetry systems. Horizontal beams span the width between the side columns to maintain their parallelism.

Free body diagrams and static equilibrium equations can be applied in the standard manner yielding forces acting in the members for the on-axis load cases. However, these loads and resulting stress levels were not the limiting case. The NSBF off-axis load case of 5 g's at 45° was the struc-

tural design driver. The NSBF allows either a dynamic or static solution for this case. The dynamic and static forces were computed to be 6,441 kg (14,200 lbs.) and 9,947 kg (21,930 lbs.) respectively. We averaged these values for a conservative design load of 8,194 kg (18,065 lbs.) All structural members then are based on this load value. The assembled gondola will have a total weight of 2,168 kg (4,780 lbs.) (Table 2.3-1). The products and moments of inertia for the gondola and telescope are shown in Table 2.3-2. These are taken about the center of mass for each system as shown in Figure 2.1-1.

A momentum transfer device is used at the point of balloon attachment. It provides 360 degrees of angular rotation for azimuthal orientation and is decoupled except for friction for azimuthal stabilization. This system is described fully in Section 2.4.

The gondola yoke frame will align itself with the earth gravity vector. The elevation servo system uses this gravity alignment for determining the telescope elevation angle and for stabilization purposes.

The telescope will be locked in place during launch. Locking is necessary to ensure maximum telescope and experiment protection for all times when it is exposed to impact loads. The locking device will be thoroughly tested with redundant schemes for activation so that the highest probability exists for achieving the locked configuration. In this configuration, peak stress levels are well below the endurance limit (equal to or less than 8,000 psi vs. 20,000 psi). The factor of safety against structural weakening due to cyclic stress is therefore 2.5. It is 5.0 against structural rupture since the yield strength of the material is $\geq$40,000 psi. Structural failure in the launch locked condition is not a concern.

Since telescope locking can not be absolutely guaranteed, the structural members were sized to carry the full loads of an unlocked telescope. Stress levels were allowed to rise to within 80% of the materials' yield strength, thereby yielding a minimum factor of safety equal to 1.5 for structural failure.

The diagonal and side column members were designed as thin-walled, deep-section aluminum beams. The dimensions of the diagonal beams are 38.1 cm square with 2.4 mm wall thickness weighing 10 kg per meter of length. Similarly the dimensions of the side columns are 38.1 cm x 61 cm x 2.4 mm wall thickness weighing 15.8 kg per meter of length.

Table 2.3-1. Gondola Weight Summary

	WEIGHT (LBS.) Unit	Subtotal
Telescope Assembly (see Table 2.2-3)		1,724
Structure and Subsystems		
Structure (Yoke Frame)		
Upper	250	
Telescope Mounting Interface	60	
Side Columns	600	
Stabilizer Beams	90	
Miscellaneous Structure	100	
		1,100
Stabilization and Pointing*		
Momentum Transfer Unit	60	
M-T Reaction Wheel	40	
Magnetic and Gravity Sensors	20	
Elevation Drive	40	
		180
Electronics		
Command	25	
Control	66	
Batteries	150	
Cables, Connectors, etc.	75	
Enclosures	170	
Miscellaneous	30	
		516
Re-entry Devices		
Telescope Latch	40	
Crash Rings	150	
Crash Pads	40	
		230
NSBF Equipment		
Ballast	500	
Electronics	55	
120-Ft. Parachute	430	
Suspension Ladder	65	
		1,050
TOTAL PAYLOAD WEIGHT		4,780 (2,168 kg)

*Remaining items not attached to Telescope

Table 2.3-2. Gondola and Telescope Products and Moments of Inertia

Gondola Inertial Properties about Its Origin (kg-m*m)

Axis	X	Y	Z
X	9640.	0.	0.
Y	0.	7330.	-317.
Z	0.	-317.	7310.

Telescope Inertial Properties about Its Origin (kg-m*m)

Axis	X	Y	Z
X	1258.	0.	0.
Y	0.	1387.	-42.
Z	0.	-42.	1065.

2.3.2 Launch, Landing, and Recovery Considerations

Launch requires that the gondola be suspended from the launch vehicle for transportation to the launch area and subsequent launch. The gondola will be exposed to low level mechanical vibrations during this activity. Experience indicates these levels to be less than the vibration levels experienced during nominal handling in test and experiment integration phases. Therefore, we will design the gondola for no detectable performance degradation when exposed to nominal handling. This is specified as not to exceed 3 g's rms over the spectral range of 20-2,000 Hz. The gondola in Figure 2.3-1 is shown suspended from the launch vehicle ("Tiny Tim") ready for launch. The NSBF requires five feet minimum for ground clearance and various radial clearances at elevations below the launch arms. This relatively light payload can be supported well in front of the vehicle allowing adequate ground and vehicle clearance. The crash rings have been stationed at the secondary to allow proper radial clearance with the launch arms. All sensitive equipment and experiments are fully protected during launch.

Damage is most likely during landings. The gondola will descend in its normal (upright) flight attitude. On impact, one or both side columns will contact the ground, absorbing energy via crushable pads and structural stressing. The structure is designed to sustain these impact loads and will roll over either naturally or be pulled over by the parachute pulling on it. The crash rings are designed to absorb this rollover energy by distortion. The crash rings should maintain a reasonable ground clearance, even if nominal (50') parachute dragging occurs, to protect the telescope and experiments. All electronics are completely protected because they are mounted inside the frame.

Recovery is difficult at best from the various terrains into which balloon payloads descend. Therefore, the yoke frame as well as the telescope are modular designs. This allows field disassembly into manageable components. These components can then be arranged on a standard flat-bed trailer for transport back to the NSBF without the need for special roadway routing and/or variances.

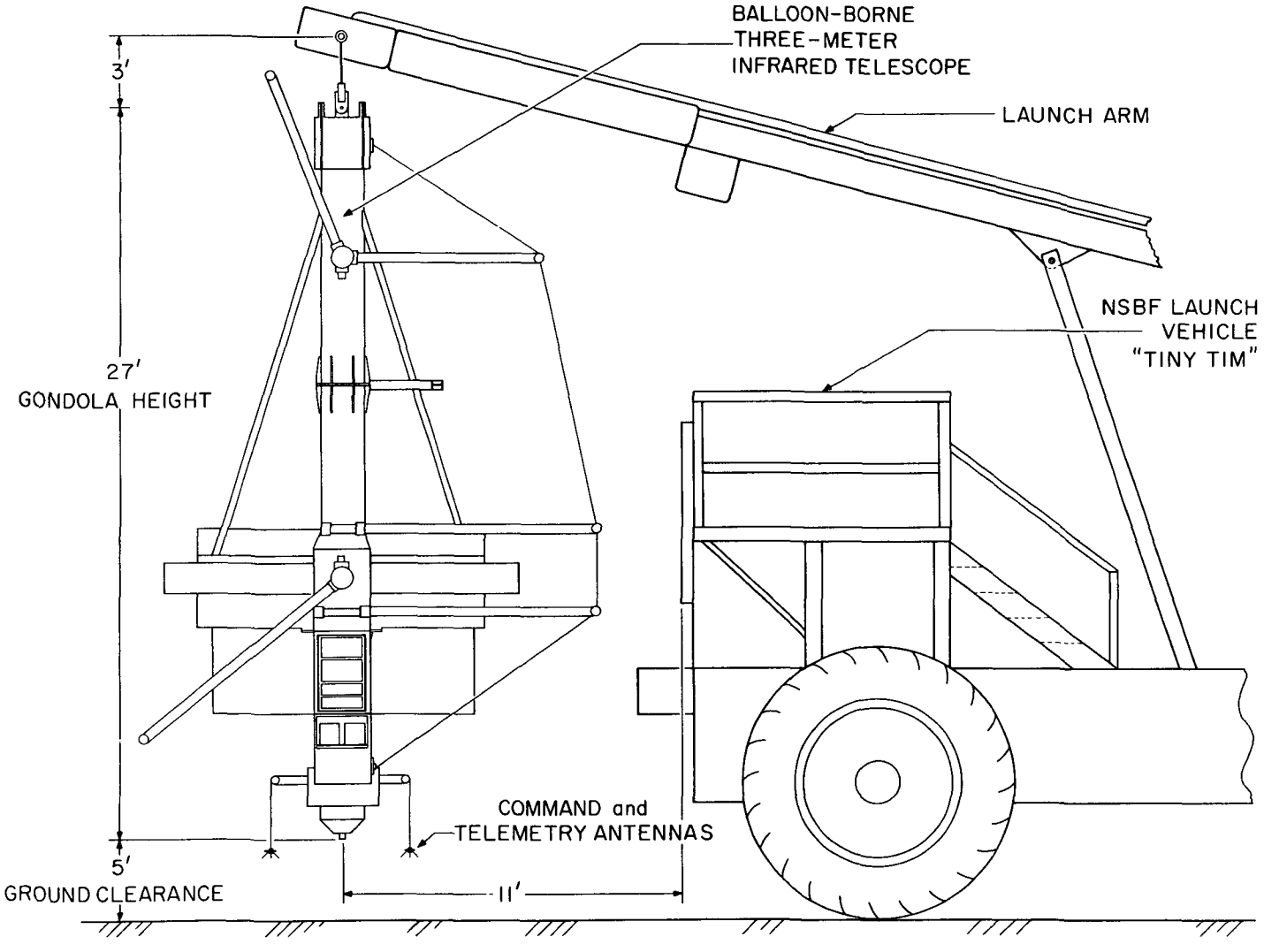

Figure 2.3-1. Gondola Suspended from Tiny Tim

2.4 Pointing and Stabilization System Design

2.4.1 Introduction

The goal of this design effort was a control scheme that would inertially point the Three-Meter Balloon-Borne Telescope to an accuracy of 1 arcsecond rms, at the same time providing the ability to scan the sky at 24 arcsec/sec and slew at 10 arcmin/sec. The control system was designed to a predicted precision of 0.1 arcsecond; the actual system behavior is expected to be somewhat worse as the analysis could not take into account all possible sources of pointing error. This state-of-the-art system is now possible only because of recent advances in certain critical servomechanism system components: the reaction wheels, gyros, and brushless motors.

2.4.2 Selection of Servo System Components

The initial task was to identify a set of minimum specifications to use in assessing candidate components. The central characteristics governing the usefulness of a component to this application are the magnitude of its nonlinear behavior and its cost. Nonlinearity manifests itself in a number of ways: as slip-stick, friction and rumble in bearings; as ripple, cogging and drag in motors; and as rumble and gimbal noise in inertial components like control moment gyros and reaction wheels. All nonlinear behavior is treated as its equivalent torque noise in this analysis. Thus the first task is to define the maximum torque noise allowable for a minimum acceptable pointing accuracy. This provides a means of selecting the candidate components.

Allowable torque noise is calculated using 1 Hz bandwidth. This frequency is the low end of the specified bandwidth range and it is considered achievable. The assumptions in this calculation are that: 1) all the noise is at 1 Hz (the bandwidth), and 2) at the bandwidth frequency the inertia of the telescope dominates the control loop response. The torque sensitivity of a control system is typically highest at its bandwidth so these assumptions and the fact that the noise will not be clustered at this frequency make this a conservative calculation.

The equation that relates allowable torque to desired pointing accuracy, at the bandwidth is:

$$Tn = Ep * Wn^2 * J_T$$

Where:
- Tn is the peak-to-peak torque noise at 1 Hz
- Ep is desired pointing accuracy, peak to peak
- J_T is telescope inertia
- Wn is the bandwidth frequency in rad/sec.

Calculations are based on a telescope inertia of 2,000 kg-m^2. Using this value, this equation yields an allowable noise torque of 0.35 Nm which is achievable. This value provides a cutoff which precludes certain components immediately.

a) Component Search:

A review of presently available components was carried out in four areas: 1) bearings for the gimbals, 2) inertial torquing systems, 3) high quality motors, and 4) sensors. The review was carried out with an eye to minimize cost and complexity. All of the reviewed components met the maximum noise requirement.

Bearings: The bearings examined in detail were hydrostatic bearings (air and liquid), flex-pivots and magnetic bearings. Flex-pivots were selected as the best candidates for the gimbals because of their low cost, simplicity, and proven behavior.

Both the air and the liquid hydrostatic bearings require extensive supporting subsystems consisting of at least a pump, reservoir and drain pan. Air bearings require a large air reserve, one quite possibly too large to be carried on the gondola. Further, their supporting air cushion is not at a high enough pressure to produce high positional stiffness; thus the bearing could touch down. If the surfaces of the air bearing touch in an uncontrolled manner the bearing would be destroyed. Therefore a secondary bearing in tandem with the air bearing is necessary to handle high-g loads such as those occurring during landing. The system is very expensive and impractical for this application. Liquid bearings are very stiff since they operate at a higher pressure than air bearings and the liquid has a higher bulk modulus than air. The system needs only a small reserve. These bearings, however, are quite expensive. Also, the liquid would probably need to be heated to keep the bearing behavior constant. Oil bearings also pose a contamination threat to the mirror. The oil does leak and would condense on the nearest cold object, the mirror and surrounding structure.

Magnetic bearings are too expensive to consider. They are not presently operating at the load levels required in this system and, therefore, this application would require breaking new ground. The stiffness (loading ability) of magnetic bearings is also not very high and, hence, a backup bearing would be required at takeoff and flight termination.

Flex-pivots provide an attractive alternative to these systems but there are application issues which must be considered when designing with flex-pivots. The pivots, being flexures, have limited travel. They have a spring constant which causes a steady-state torque when the telescope is not pointing at the pivot null position and the pivots' spring behavior transmits torques related to the motion of the gondola to the telescope, thus reducing its isolation from disturbance torques. The pivot spring constant varies with the magnitude and alignment of the borne load (see Figure 2.4-1). This characteristic can be helpful; with proper selection of pivot size the flex-pivot spring constant can be diminished considerably (see below). The spring constant also varies with temperature. Further, the flexures have limited thrust load capacity. These problems are suc-

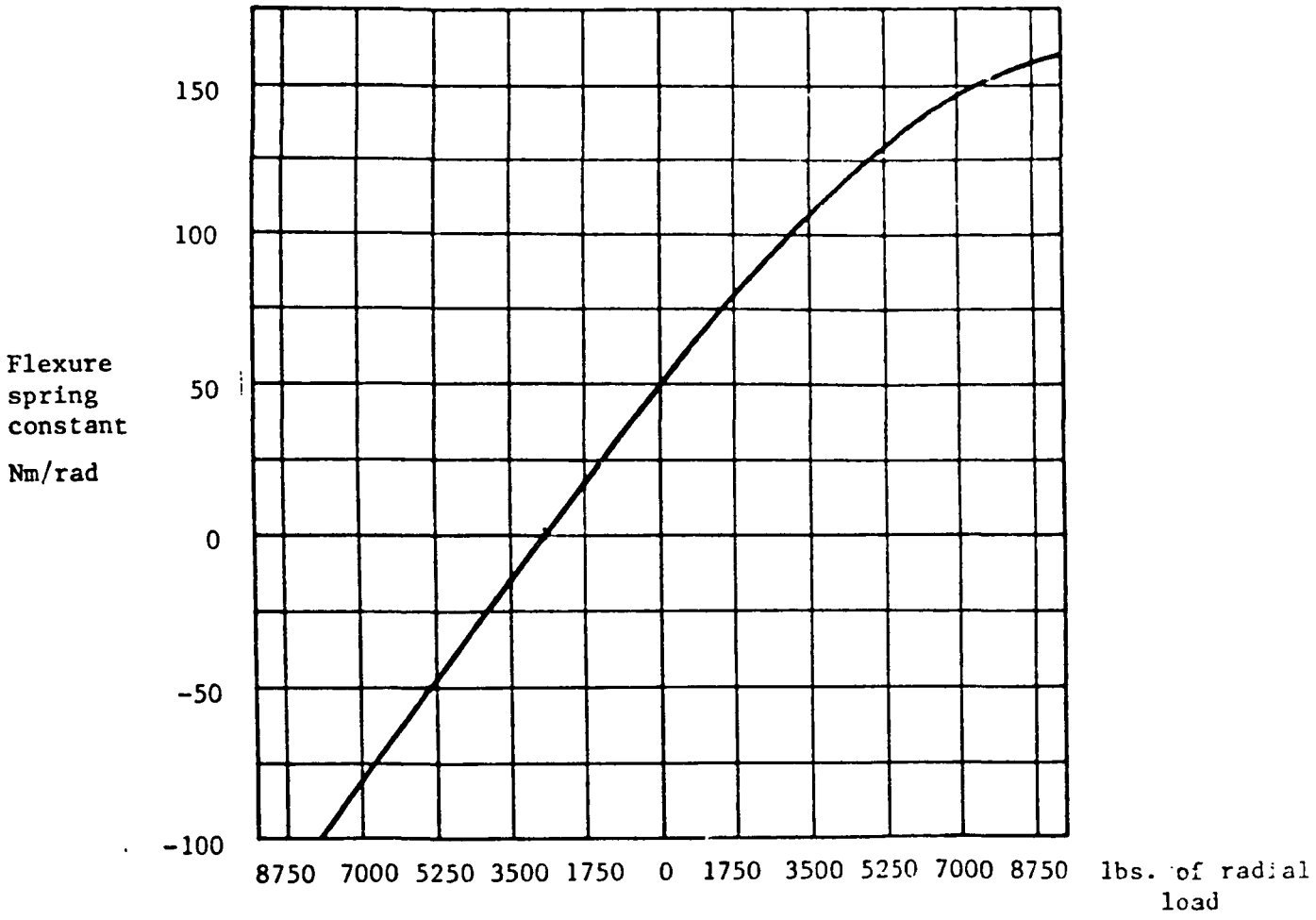

Figure 2.4-1. Flexure Spring Constant Variation with Radial Load for a Selected Flex-Pivot (from Bendix Data).

cessfully addressed in the gimbal design presented in the next section.

Inertial Torque Devices: Control moment gyros (single and double axis) and reaction wheels were reviewed. The torque required for this application is about 5 Nm peak. This is high for a reaction wheel but control moment gyros (CMG's) could deliver this torque easily. Their expense (about $1M per unit) and complexity unfortunately make them an unlikely choice for a balloon application. No CMG system previously designed meets all the Three-Meter Balloon-Borne Telescope requirements. There are production reaction wheels available that come close to meeting the torque output requirements. Developing one around a presently made wheel with increased torque capability would be considerably less expensive (costing only $100K or less) than purchasing a set of CMG's. This price includes magnetic bearings, a feature that makes the reaction wheel a nearly perfect torque source. There will be very little torque noise and the torque output will be linear through zero wheel speed. We have baselined reaction wheels in this application.

Motors: The selected design requires two motors per axis: one that drives the reaction wheel and which will be part of that assembly and one that drives across the gimbal. The specifications on maximum torque and the maximum noise (cogging, drag and ripple) are such that only a DC brushless motor will suffice.

Sensors: The servo pointing reference comprises a two-axis gyro system whose spin reference axes are continually updated by error signals from a telescope-mounted star tracker. This approach greatly eases the requirements on gyro drift and allows a "scan" mode of operation whereby the star tracker output is disabled and the gyro inertial reference axes are controlled by application of electrical currents to the gyro gimbal torquer windings.

b) Star Tracker:

Probably the least expensive approach would be an adaptation of the single-star tracker system in use on the KAO. This consists of a telescope feeding a COHU Intensified Silicon Target (ISIT) camera. Resolution is 400 x 600 effective elements covering a 20- x 30-arcminute field of view. Video output is fed to a custom-designed electronic module and then computer processed to generate correction signals to the gyro system. In turn, the gyros supply error signals to the main telescope servo loop.

This system, with a 6-inch tracking-telescope, has demonstrated 2-3 arcsecond p-p stability while tracking stars of +12 magnitude on the KAO. On a balloon payload, in the absence of airframe vibration and air turbulence, this system might easily perform at the 1-arcsecond p-p level. The Three-Meter Balloon-Borne Telescope can accommodate a larger tracking telescope, say 15 inches diameter, if star tracking down to 14th magnitude is desired.

More modern star-tracker systems use charge-coupled devices (CCD's) or intensified CCD's (ICCD's) in the focal plane. Very high resolution can be obtained in these systems by deliberately blurring the image to cover a number of pixels, then digitally processing the data in real time to com-

pute the centroid of the image. This technology is not new; and, in the opinion of those now working in this field, development of a system capable of better than 0.2-arcsecond resolution is certainly feasible (see Section 2.5).

c) Gyros:

As explained above, pointing system performance is not greatly affected by gyro drift because of the presence of the star tracker in the loop. Gyro noise, however, will be directly coupled into the servo system. Assuming a servo loop bandwidth of 3 Hz, the specification of 1-arcsecond peak-to-peak jitter (= 3.3-arcsecond rms) requires that the gyro noise power spectral density (PSD) be less than

$$0.3 \text{ arcsec } \sqrt{3\text{Hz}} = 0.173 \text{ arcsec } \sqrt{\text{Hz}}.$$

Typical PSD for off-the-shelf gyros of the better inertial grade are of the order of 0.01 to 0.001 arcsec$\sqrt{\text{Hz}}$. For example, Northrop's model GGG-PMM single-axis gas bearing gyro, currently in production, is quoted at 0.001 arcsec$\sqrt{\text{Hz}}$ and Singer's "Gyroflex" gyro (while no PSD figures are available) has demonstrated position-pointing stability of 0.004 arcsecond in a system bandwidth of 5 Hz.

2.4.3 Servomechanism System Description

The telescope pointing system is designed to isolate the telescope in inertial space. This requires that the telescope be balanced about each axis, the principal moments of inertia be in reasonably good alignment with the gimbal axes and that the losses across the gimbals be small. The isolation can be further increased by torquing directly to inertial space by means of a reaction wheel or control moment gyro. The selected bearings (flexures) do reduce isolation by their spring constant but this is linear and predictable.

The gimbal arrangement of the selected system is shown in Figure 2.4-2. Two components cross the gimbals; one is the brushless motor and the other is the flex-pivot bearing. The telescope side of the flex-pivot is supported in ball bearings which in turn have their motion controlled by a stepper motor/worm gear combination. The gear mating with the worm is shown attached to the extension shaft on the flex-pivot. The motor acts to center the flex-pivot during fine pointing. This is the source of some torque noise but it is at a very low frequency and should not be a problem. The same motor slews the telescope from point-to-point during coarse pointing mode. The flex-pivots are locked out prior to coarse pointing maneuvers, either by driving a pin into the gimbal end of the flex-pivot extension or by activating a magnetic brake across it. These measures leave the ball bearings free to rotate about the clamped flex-pivot. Coarse mode sensors such as potentiometers and tachometers are required in the gimbal design but are not shown in this drawing.

In the elevation gimbal this arrangement has the added virtue that as the flex-pivot is recentered its relationship to the gravitational load

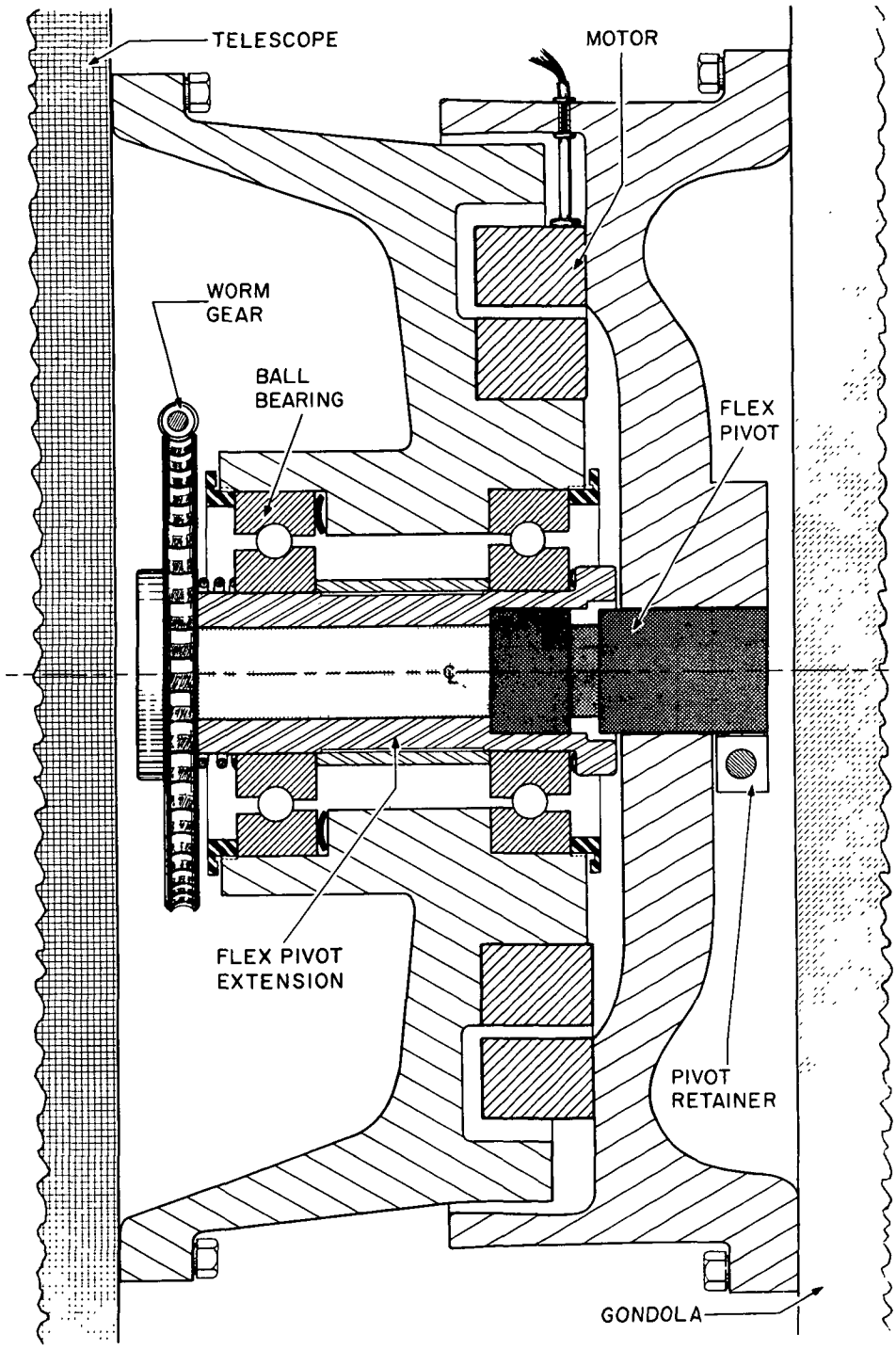

Figure 2.4-2. Telescope Gimbal Design

remains the same, keeping the spring constant invariant. The spring constant can be held fairly small.

The cross-elevation axis, being the inner gimbal, changes its relationship with the gravitational vector. As the orientation of the load changes (with changes in elevation angle) the flex-pivot spring constant varies (Figure 2.4-1). This problem can be minimized but it cannot be avoided. The isolation in this axis varies.

The motor that crosses the gimbal couples the telescope to the gondola in a way that is dictated by the control system. It acts to drive momentum from the telescope/reaction wheel system into the gondola.

The reaction wheels are attached directly to the telescope. The proposed units use a brushless motor and magnetic bearings. This assures that the torque noise they generate while spinning and changing direction is low.

2.4.4 Pointing System Control Laws and Predicted Performance

a) Fine Pointing (Inertial) Mode

The control system performs a number of tasks: 1) it stabilizes the telescope orientation; 2) it rejects errors in pointing due to external torques on the telescope; 3) it maintains the speed of the reaction wheel within its operational band.

Control Loop Descriptions -- Both Axes

The two fine-control axes (elevation and cross-elevation) are slightly different. The fine-control loop configuration is identical for both but the way they interact with the gondola differs. The two loops are laid out in block diagrams in Figures 2.4-3 and 2.4-4.

The fine control on each pointing axis is split into two coupled loops. The primary loop stabilizes the telescope. This loop contains the reaction wheel motor as the actuator, the star tracker/gyro as a sensor and is closed with a simple proportional plus rate compensation approach. The secondary loop contains a gimbal motor as actuator and reaction wheel tachometer as sensor. The gimbal motor in the secondary loop delivers torque proportional to the speed of the reaction wheel. The primary loop rejects quickly varying torques while the gimbal motor loop removes momentum from the telescope/reaction wheel combination. One of the benefits of this design is that the secondary loop acts as integral compensation in telescope positioning, rejecting slowly varying or steady-state torques and eliminating what otherwise would be steady-state offsets. Without this feature a steady offset or external torque would quickly cause the reaction wheel to saturate.

An analysis of this in general form is presented in Appendix B. In summary this analysis shows that the telescope proceeds to a commanded orientation with zero steady-state error regardless of the flex-pivot's

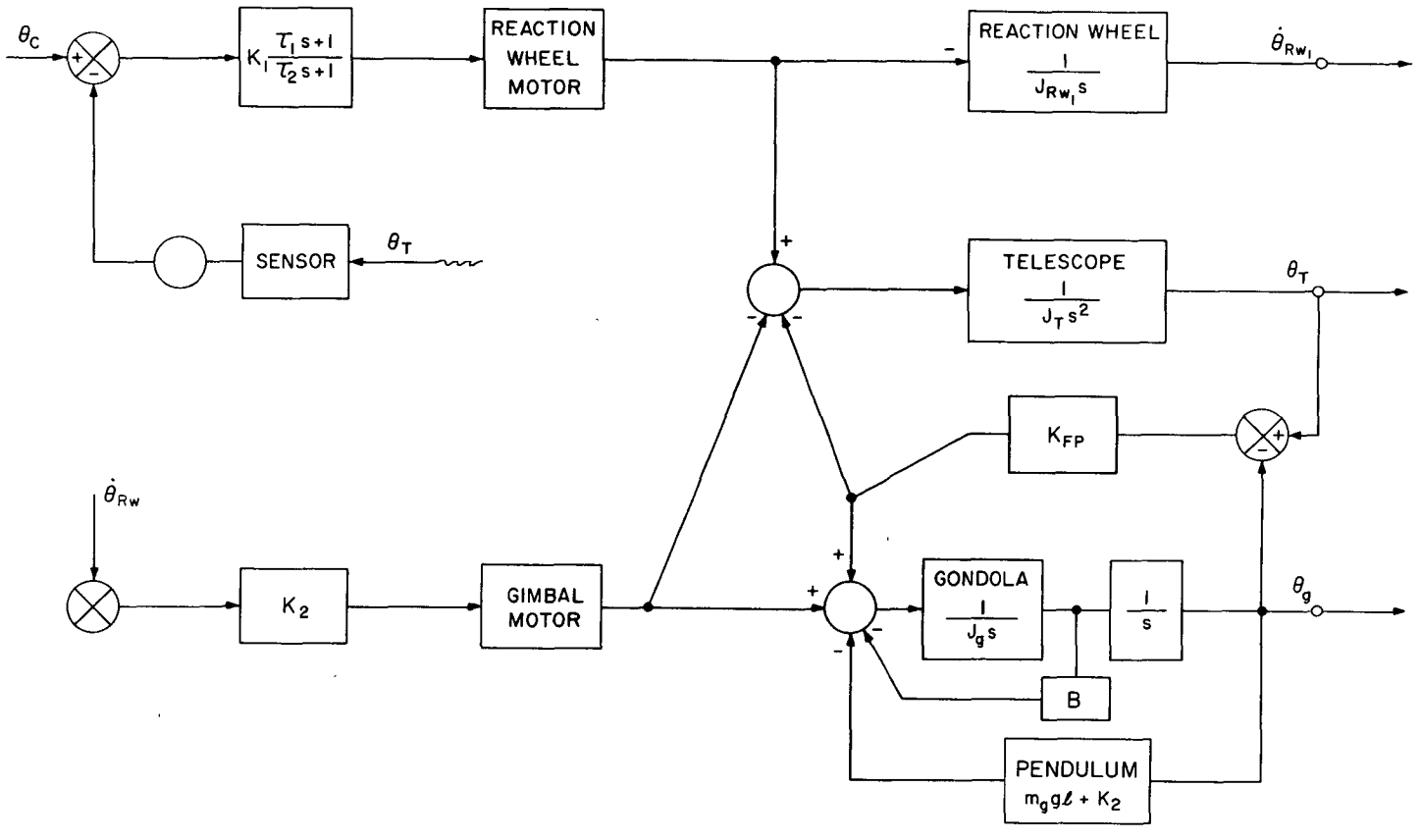

Figure 2.4-3. Block Diagram of Elevation Servo

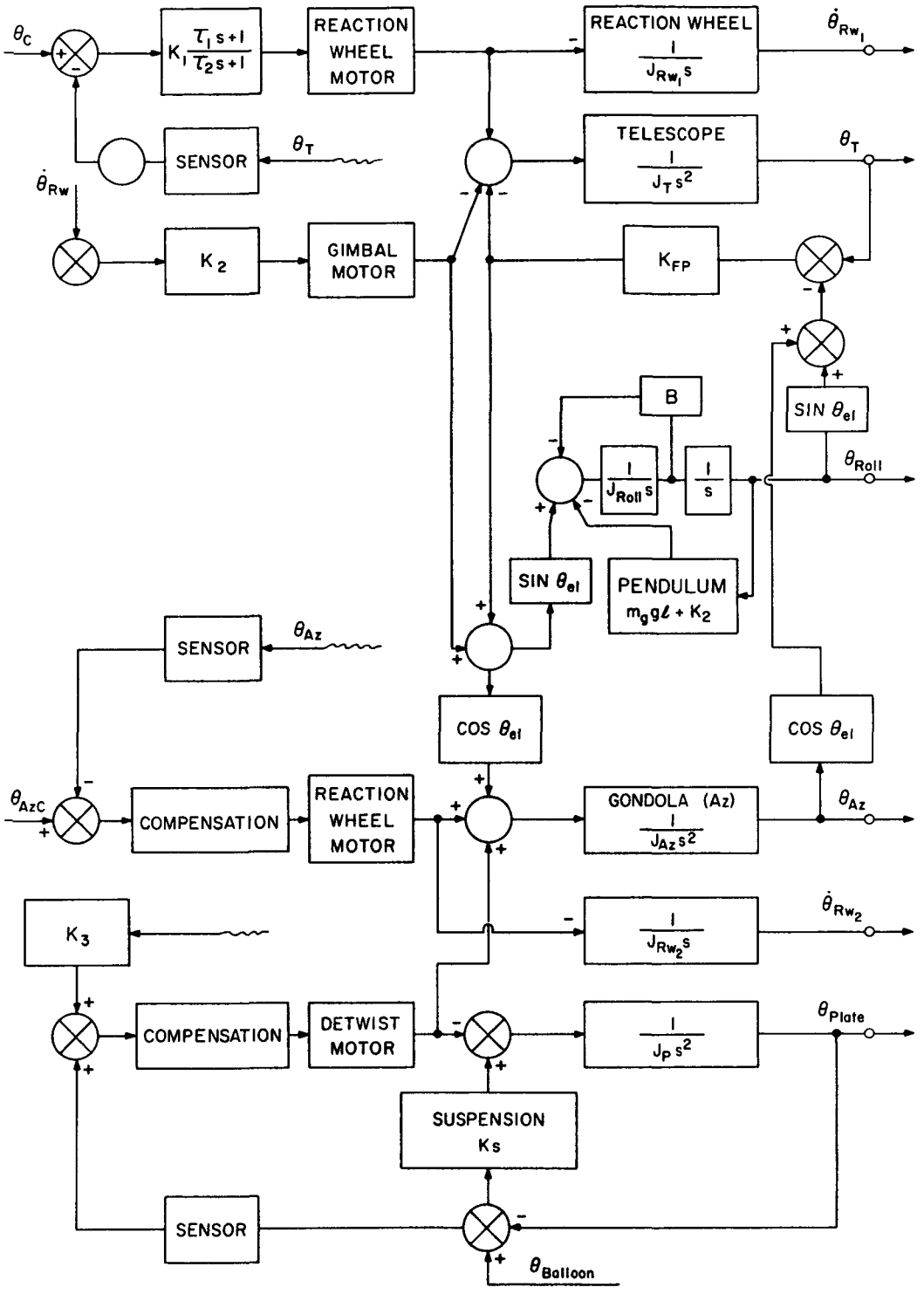

Figure 2.4-4. Block Diagram of Cross-Elevation Servo

spring constant or steady-state external torque (e.g., imbalance, wind load, etc.). The reaction wheel ends up at a steady-state speed proportional to both the external torque applied and the flex-pivot constant. This analysis holds for both axes. The differences between the axes manifest themselves in the way the individual axes transfer momentum to the gondola. When the elevation axis control system excites the gimbal motor and dumps momentum the gondola is forced into a compound pendulum mode about an axis parallel to the elevation gimbal. This could be a problem but only if the amplitude became large. It would not be a fundamental flaw in the design if it were not addressed because the telescope is isolated from movement of the gondola about this axis. These motions become a problem if they excite nonlinearities in the drive or bearing components. Methods for dealing with this gondola energy are dealt with later.

When the cross-elevation reaction wheel is dumped it excites two modes in the gondola. One mode is about the balloon suspension lines (see Figure 2.1-1 for the definition of the axes) and the other is about the gondola roll axis. The vertical axis or twisting mode is excited proportionally to the cosine of the elevation while the roll mode is excited proportionally to the sine of the elevation angle. The telescope is only isolated from gondola motion around the cross-elevation axis. The compound rotation that dumping cross-elevation momentum sets up is not around this axis. The component of gondola rotation around an axis perpendicular to the cross-elevation (around the telescope optical or roll axis) will affect the telescope. The extent to which this is a problem is related to the elevation angle and is worst at 45 degrees.

The momentum in the gondola about the optical axis will cause a problem if ignored because the telescope will probably not be tracking on the same star it is viewing. As the telescope rolls about its optical axis the control system keeps the guide star stationary in the tracker telescope. However, the orientation of the star field changes with this motion. The viewed star describes a circle in the main telescope whose center is the tracked star. The larger the product of the offset angle and the roll amplitude, the larger is the pointing error on the viewed object. Thus to maintain precise pointing the amplitude of telescope roll and the tracking offset must be limited.

To control these motions the energy in each gondola mode must be dissipated. The momentum in the two gondola axes is handled differently. The twisting mode is managed by the azimuth coarse control loop which remains active during fine pointing. The energy is driven from the gondola into a third reaction wheel leaving the gondola in commanded orientation. The reaction wheel energy is then sent into the balloon by means of a system that twists the suspension lines (discussed below). The roll energy is dissipated using passive elements similar to shock absorbers mounted between the gondola and the suspension. This arrangement can also dissipate motion caused by the elevation axis dump.

The gondola itself is isolated from the balloon suspension by a system that untwists the suspension lines. The torque created by the balloon rotation is measured at the gondola and a motor is activated to compensate for it. The system further acts to desaturate the azimuth reaction wheel. This it accomplishes by twisting the lines and driving a moment into the

gondola. This causes the azimuth loop to slow the reaction wheel as it compensates for the new torque.

Predicted Performance

The predicted servo-loop performance is outlined below using calculated system characteristics. A detailed derivation of the equations and the numbers is given in Appendix B.

Each loop is assigned compensation as if it were uncoupled. The dynamics of the sensor are assumed to have little effect on the control system design. These assumptions make each loop second order. We can then write the dynamics equation for each loop with an unknown compensation zero.

$$\ddot{\theta}_T + \frac{K_G \tau}{J_T} \dot{\theta}_T + \left(\frac{K_{FP} + K_G}{J_T} \right) \theta_T = \frac{K_{FP}}{J_T} \theta_C \qquad (1)$$

where K_G is servo gain

τ is servo zero

K_{FP} is flex-pivot spring constant

J_T is telescope inertia.

By writing the generic form of a second order oscillator:

$$\ddot{\theta} + 2\omega_n \zeta \dot{\theta} + \omega_n^2 \theta = \omega_n^2 \theta_C \qquad (2)$$

where ω_n is the undamped natural frequency

ζ is the damping ratio

we can compare it to the equation for each individual loop. Given the system parameters (inertia, spring constant, etc.) and the desired controlled dynamics (bandwidth, damping) the coefficients of the two equations can be matched and the control determined.

The compensation used in the study is a simple analog lead network though the system can just as well be digitally controlled. Thus, apart from the zero, there is a pole to select. The pole is placed at 10 times the frequency of its associated zero; all the control-related gains are lumped together for the analysis.

The constant of proportionality between the reaction wheel angular velocity and the gimbal (or twist) motor torque are set so that the wheel will not saturate under expected steady torque loads.

The detailed system response characteristics are determined by collecting the individual loop equations with their coupling and generating a system of equations that describes the whole system. These are then transformed into a set of first-order equations and coded on the computer for simulation. The code yields various frequency and step responses. The behavior thus predicted is adjusted using the results of the generic analysis mentioned earlier until the specifications are met.

The primary servo loops are closed at a bandwidth of 3 Hz, and a damping ratio of 0.7. The frequency response is shown in Figure 2.4-5. This response is almost identical to a true second-order system, justifying the approximation used in the design and testifying to the high degree of isolation that actually exists between the telescope and the gondola. The maximum loop sensitivity to noise generated at various points in the system was polled and the results are listed in Table 2.4-1.

Table 2.4-1. Gondola Servo System Control Sensitivities

Measured Affect	Noise Applied by	Peak Sensitivity	Unit	Frequency of Peak (rad/sec)
Telescope Pointing (both axes)	Telescope Torques	.616	arcsec/Nm	12
" "	Gondola Motion	$1 * 10^{-5}$	arcsec/arcsec	12
" "	Gondola Torques	.01	arcsec/Nm	12
Telescope Pointing (Cross-elevation)	Balloon Motion	$3 * 10^{-6}$	arcsec/arcsec	1
Gondola Position	Gondola Torques	3.4	arcmin/Nm	1
Gondola Position	Balloon Motion	$5 * 10^{-2}$	deg/deg	1

The most important sensitivity is that of the telescope to on-board torque noise. The sensitivity indicated for both fine loops yields a maximum total torque noise specification of 2.4 Nm at 3 Hz for 1-arcsecond peak-to-peak precision. The identifiable sources of noise are:

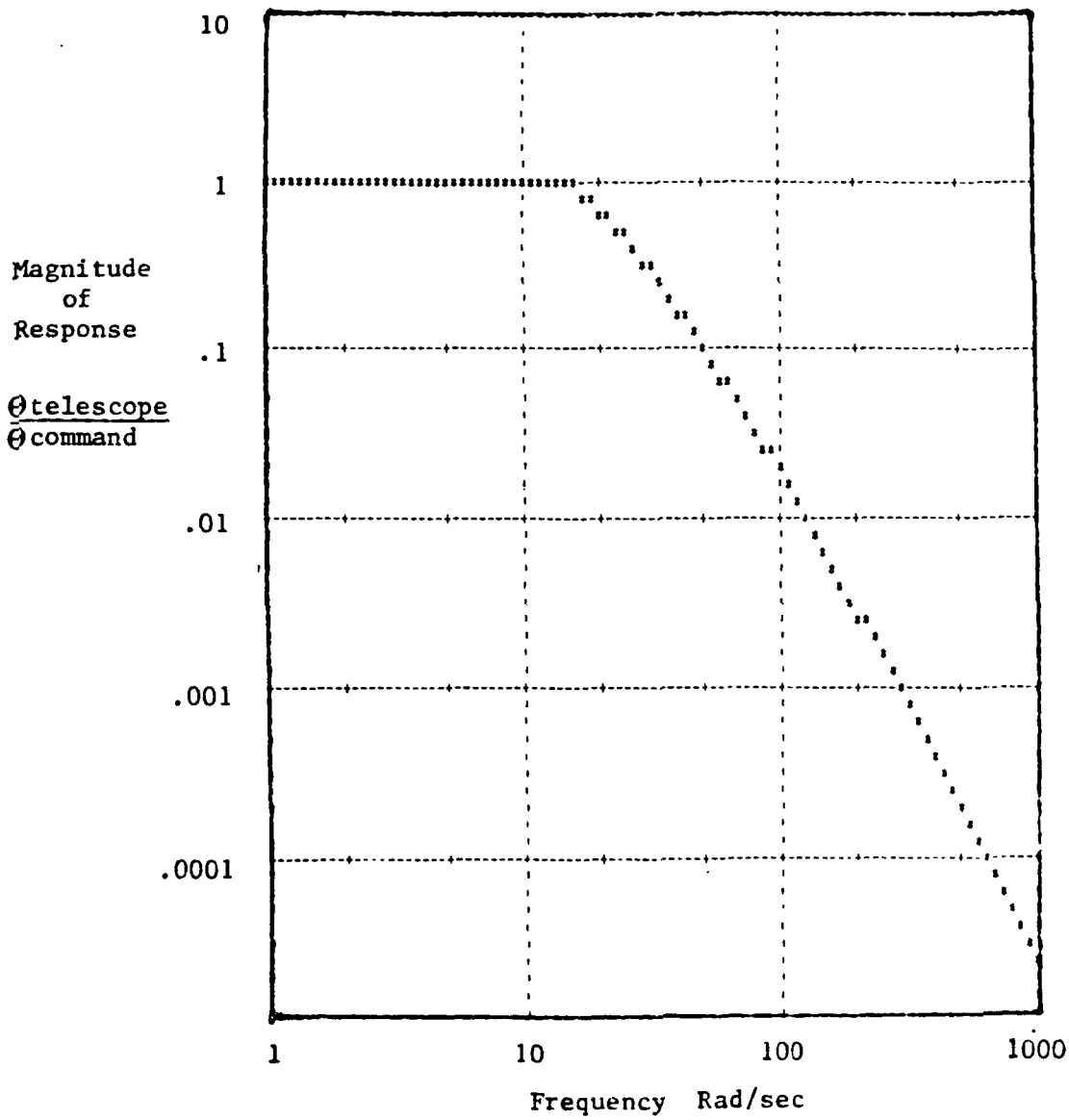

Figure 2.4-5. Fine Pointing Control System Response to a Sinusoidal Command Signal

1) Motor nonlinearity
2) Bearing nonlinearity
3) Cross coupling
4) Gondola displacement transferred through the flex-pivots
5) Telescope imbalance driven by balloon dynamics
6) Reaction wheel rumble
7) Chopper system imbalance
8) Sensor noise
9) Experiment movable devices

The largest source of noise is the motors and to a large degree they are the limiting factor in ultimate precision. The specifications on the motors that were selected had a total nonlinearity during operation as high as 0.13 Nm or, while just "windmilling," of 0.016 Nm. These specifications apply to both the reaction wheel motor and the gimbal motor. The expected values for the other sources of noise are shown in Table 2.4-2.

Table 2.4-2. Gondola Servo System Noise Sources

Noise Source	Peak-to-Peak Amplitude	Frequency [rad/sec]
Motor Anomaly	.01-.13 Nm	18
Bearing Nonlinearity	nil, pivots always near center	
Cross Coupling	10^{-4} Nm	18
Gondola Motion	.02 Nm	6
Telescope Imbalance	$2 * 10^{-4}$ Nm	6
Reaction Wheel Rumble	.02 Nm	6 - 18
Chopper	---	Higher frequency rumble
Sensor Noise	.04 arcseconds	18
Experiment Movable Devices	---	Time-lined for least effect
Total Control Pointing Error	.045-.1 arcsecond	18

The total torque noise expected around 3 Hz is 0.135 Nm. This is less than the maximum noise specification calculated above. This noise level has less effect on the system in final configuration then the previous calculation predicted as the bandwidth is higher. The predicted impact on preci-

sion of the control components based on these noise levels plus the sensor noise if it were all at 3 Hz is +/- 0.1 arcseconds. This noise is neither white nor clumped at 3 Hz but it is very conservative to base the noise prediction on the assumption that all the noise is at the maximum bandwidth and so, while there are undoubtedly other sources of noise in the system not included in this estimate, the actual system error should approach this prediction.

Once hardware is being tested the actual system operation may be improved in spite of any unexpected shortfall of the predicted behavior. There are a number of ways this might be done. The most obvious is to use the frequency response to our advantage. The frequency content of some of the noise sources is more or less controllable. By moving the frequency of the noise from these sources to a band that the system is less sensitive to, the overall accuracy of the system will improve. Another method commonly employed is to increase the passive damping of the gondola and thus keep the system components less active. The less active the motor, the less it generates noise to jitter the telescope. Yet another method for improving the system behavior is to design the system using modern control methods specifically meant to produce control regulators with low noise sensitivity. This usually is done to the detriment of the system step response. The telescope does not require a very fast step response so this is not a large loss. Further, there are methods to improve system step response without affecting the closed-loop control law. This is done by including dynamics in the command leg of the control block. These methods will be examined in the upcoming year and will be easy to implement at any time in the project, especially if the system is digitally controlled.

b) Coarse Pointing (Magnetometer) Mode:

The Magnetometer Mode is a coarse servo system for pointing the telescope at a celestial object to an accuracy of ±30 arcminutes in elevation and azimuth with jitter of ±5 arcminutes or less at a bandwidth of approximately 1/4 Hz. This will allow recognition of a star field in the five-degree field-of-view aspect camera and thus permit confirmation of the telescope celestial orientation. Modern sensors can make stars as dim as ninth magnitude visible to the ground telescope operator.

The Magnetometer Mode uses the gravity vector measured on the gondola as an elevation reference and the earth's magnetic field as the azimuthal reference. These signals are switched into the inertial servo system discussed above to replace the inertial error signals, thereby utilizing the same drive systems to control the telescope's line-of-sight. This system is similar in many respects to the successful approach taken in our One-Meter Balloon program.

The elevation loop remains similar to the fine-mode loop in that it is a simple position loop. The position error voltage is derived from an optical encoder mounted on the elevation trunnion concentric with the elevation torque motor. Damping is achieved by feedback from a tachometer also mounted on the elevation trunnion. The position loop is calculated to have 1/4 Hz bandwidth and it is a type-1 loop (single kinematic integration) having zero position error.

Position commands are transmitted via the telemetry link as 12-bit words (LSB = 1.3 arcminute) and converted to analog voltages by an on-board digital-to-analog converter (DAC). To minimize acceleration and transient effects on the system which might excite high-frequency mechanical resonances or compound pendulum motion, the output of the DAC is rate-limited and filtered before being fed to the error summing junction. A reduced block diagram of the elevation position loop is shown in Figure 2.4-6.

The azimuth loop is constructed using a Schonstedt, MND-5C, null magnetometer as the error sensor. It provides a voltage proportional to rotational offset which is positive or negative depending on rotational direction. This voltage is used to stabilize the gondola at the desired azimuthal angle. The sensor in turn is mounted on a turntable which is controlled by a standard stepper motor-encoder position loop. This allows selection of azimuthal angles with a step size of 5.3 arcminutes over the full 360° azimuthal angle. The desired azimuth angle is commanded via a 12-bit data word and is compared to the encoder reading. If a difference exists the stepper motor activates to bring them to equality. The sensor rotation simultaneously creates an error signal to the gondola azimuth loop which drives the gondola to the new angle. A rate limiting circuit will be used to limit the gondola acceleration, possible overshoot and subsequent oscillation.

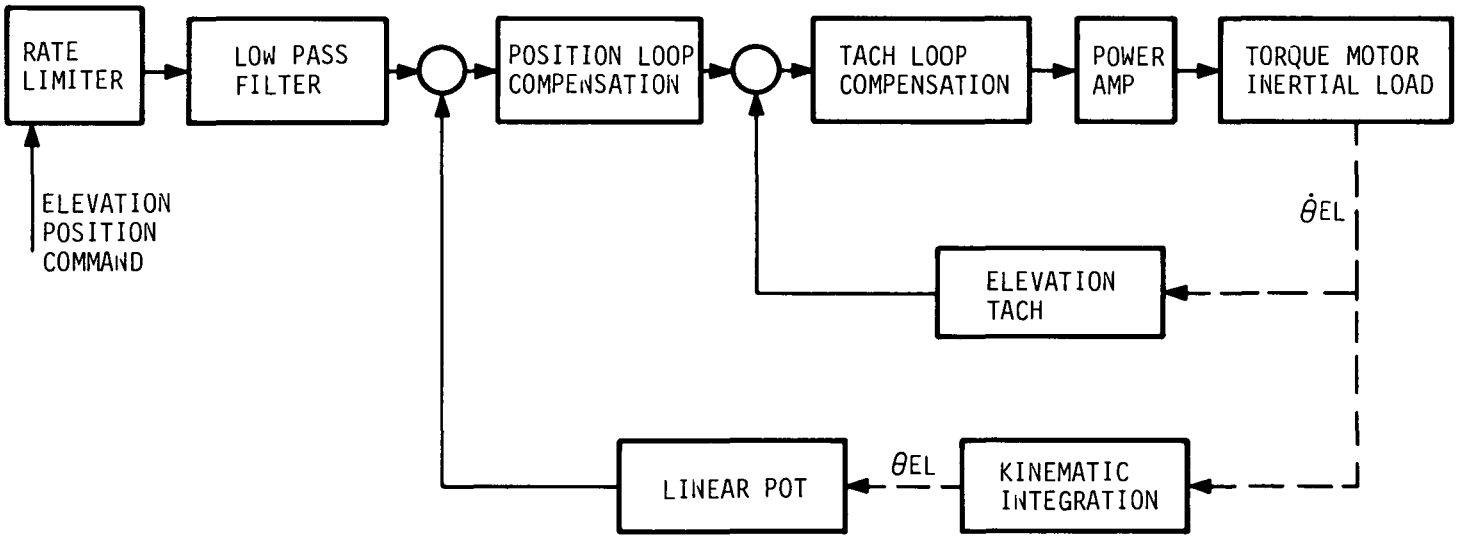

Figure 2.4-6. Elevation Position Reduced Block Diagram -- Position Mode.

2.5 Aspect System Design

Pointing of the telescope at a desired astronomical object is achieved through the use of three intensified-CCD television cameras. One camera is used for acquisition, one for fine guiding, and one can be used for both if necessary. The primary acquisition camera, with a 5° field of view (FOV) and a limiting stellar magnitude of approximately 8, is used to identify the initial star field. The primary tracking function is performed by a 10' FOV camera, with the backup camera having a 1° FOV. These cameras are coupled to 20-inch and 12-inch telescopes, respectively.

In a 10' field of view, dead-reckoning can be used to compute the rotation angle (after determination of a constant offset) with sufficient accuracy to permit single-star tracking. (In this size field, no correction would be required for the pendulum motion of the gondola.) Two-star tracking and scans over large angular fields would be possible using the 10' camera. Gyro drift rates should be small enough to permit tracking for time scales of minutes without updating from the star sensors, if required.

Because the optical imaging quality of the primary three-meter mirror may be poor (although we plan to try developing a mirror of useful optical quality), we may not be able to use a focal-plane television camera. Its functions, such as monitoring the chopper performance and boresighting the tracking cameras, could be performed by the far-infrared photometer/camera and by an optical chopper position sensor, in which an image at the focal plane is projected on the secondary mirror and reflected back to the focal plane. This type of system has the following advantages:

1. Since the optical images in the tracking cameras could be as small as 0.5 arcsecond and the field would not be chopped, it may be possible to go to fainter limiting magnitudes than with the main telescope mirror.

2. Guiding on the small, unchopped images would be more accurate.

3. The tracking cameras necessary for guiding could be developed, constructed, and tested independently.

4. The tracking cameras can have a larger field of view than an offset guider operating in the focal plane of the main telescope.

The camera being considered at this time for aspect determination is the Fairchild intensified CCD camera Model CCD 3000I. This camera has a pixel format of 488 lines by 380 columns. The wafer-type intensifier used increases the camera sensitivity by a factor of 1,000. The camera has two types of outputs. One is a standard composite video signal; the second output provides all the timing waveforms and video level for each pixel. The latter output, when coupled to a computer, can be used, by centroiding, to determine the image coordinates of the guide star to at least 1/10 pixel accuracy (0.2" position accuracy in 10' FOV camera). The intensified CCD camera offers the advantages of fixed pixel structure, high sensitivity, insensitivity to magnetic fields, lack of high voltage requirements, and small size, all of which make it ideal for this application. Such a camera

is presently being evaluated in the OIR Division of the Smithsonian Astrophysical Observatory. Advances in technology (lower readout noise) may also make it possible to use unintensified CCD cameras in the star trackers. This approach is currently being investigated at the University of Chicago on ground-based telescopes. The ASTROS CCD tracker, developed by Jet Propulsion Laboratory (JPL) for operation from the Space Shuttle bay on the Instrument Pointing System (IPS), provides extremely precise measurements of star image coordinates as inputs to the Image Motion Compensation system used to stabilize the science instrument focal planes. ASTROS can determine star image position to an accuracy of 0.2" over a field of view of 2°.2 x 2°.5. This requires consistent star image position determination to an accuracy of 1/100 pixel. The ASTROS tracker will be used in early 1986 on the first Astro mission of the Space Shuttle to observe Halley's Comet and a variety of other astronomical targets. If it is possible to approach this performance, our 1° camera could track as accurately as the 10' camera.

2.6 Electrical Systems Design

2.6.1 Command and Telemetry System

The command and telemetry system will be very similar to the system already in use at NSBF and compatible with it. The heart of the telemetry system is the NSBF Consolidated Instrument Package (CIP II) (see Figure 2.6-1). It consists of subcarrier oscillators used to FM/FM modulate the UHF L BAND telemetry transmitters for efficient use of the authorized bandwidth. Standard IRIG VCO channels of 1, 3, 5, 7, 8, 9, 10, 11, 12, B, E, H, or HH are used. The channel HH (referred to as wide band H or WBH) is used on most flights for PCM data rates of up to 80 kilobits of NRZ or 40 kilobits biphase. There are six of the IRIG channels available for the user.

The main PCM command system provides for 80 discrete functions and a 16-bit parallel data word with strobes. These would be used for control of the gondola. A second command decoder can is provided with a different address. This provides 48 discrete commands and a 16-bit parallel data word with strobes for the experiments.

The PCM data encoder format is controlled by an EPROM. There are 128 inputs available, which can be programmed for either analog single ended, analog differential input, parallel digital input or serial digital input. The bit rate is 80.92-kilobits under internal control and 256-kilobit under external control (planned for the future). The gondola would require about 50 digital inputs (5 at 10 bits each) and 30 analog inputs. The remaining 48 inputs would be available for the experimenter.

2.6.2 Gondola Electronics System

Conceptual design of the most critical of these systems, the pointing and stabilization systems, is complete and discussed in detail in Section 2.4 of this report. The balance of the systems are straightforward extensions of existing designs in use on the Smithsonian One-Meter Balloon Infrared Telescope. For flexibility, the designs of the primary experiment controller will be microprocessor based. Low power technology will be used throughout the gondola electronics systems. A block diagram of these systems is shown in Figure 2.6-2.

2.6.3 Gondola Power Requirements

Power requirements are summarized in Table 2.6-1. For the first flights the primary power will come from lithium/sulfur dioxide cells. Power Conversion, Inc., produces a lithium pack rated at 36 volts open circuit and 30 volts under rated load (2a) and at rated capacity (35 ampere-hours). The gondola would require seven packs in parallel. The battery complement for each mission will depend on the experiments flown.

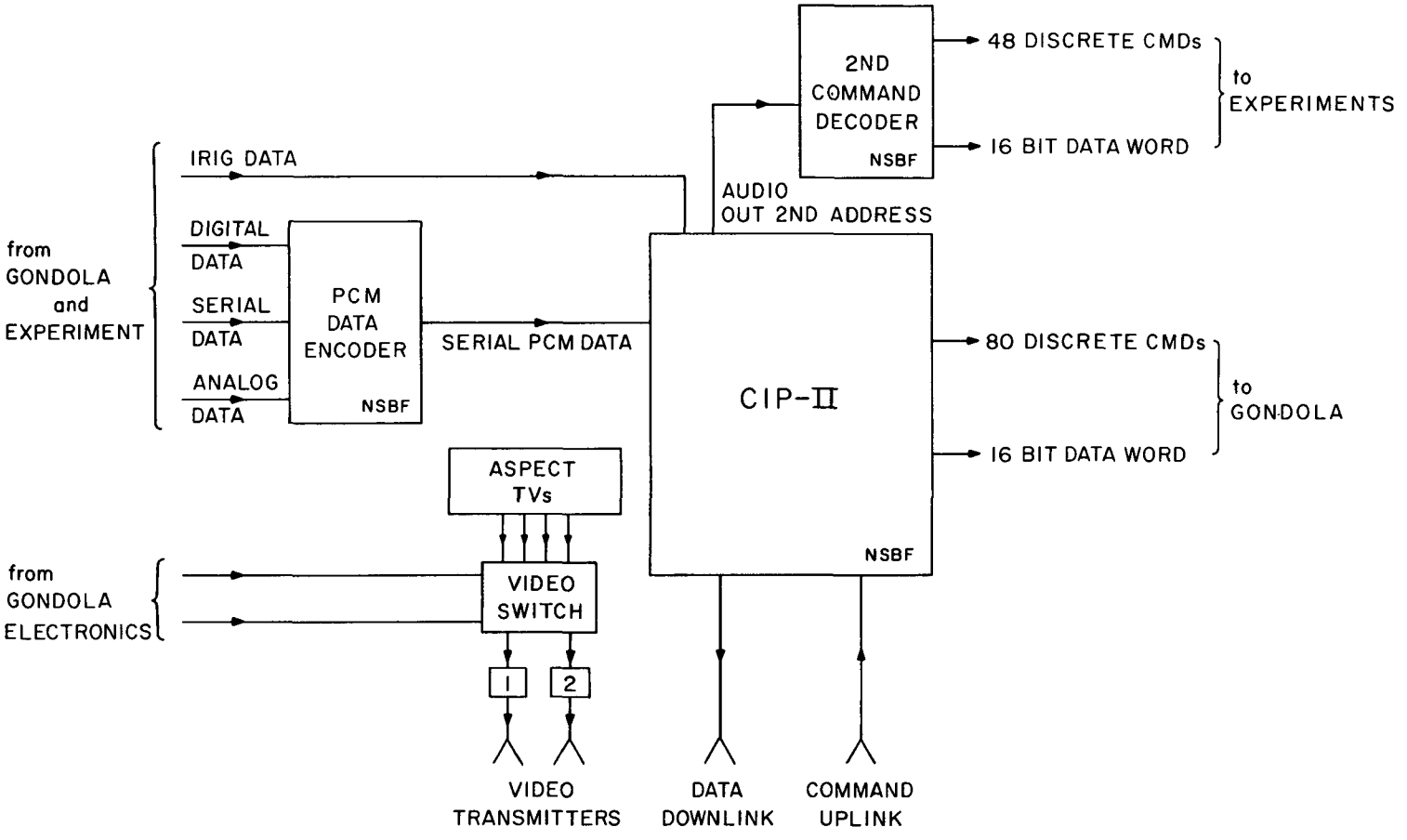

Figure 2.6-1. On-Board Command and Telemetry System for the Balloon-Borne Three-Meter Infrared Telescope

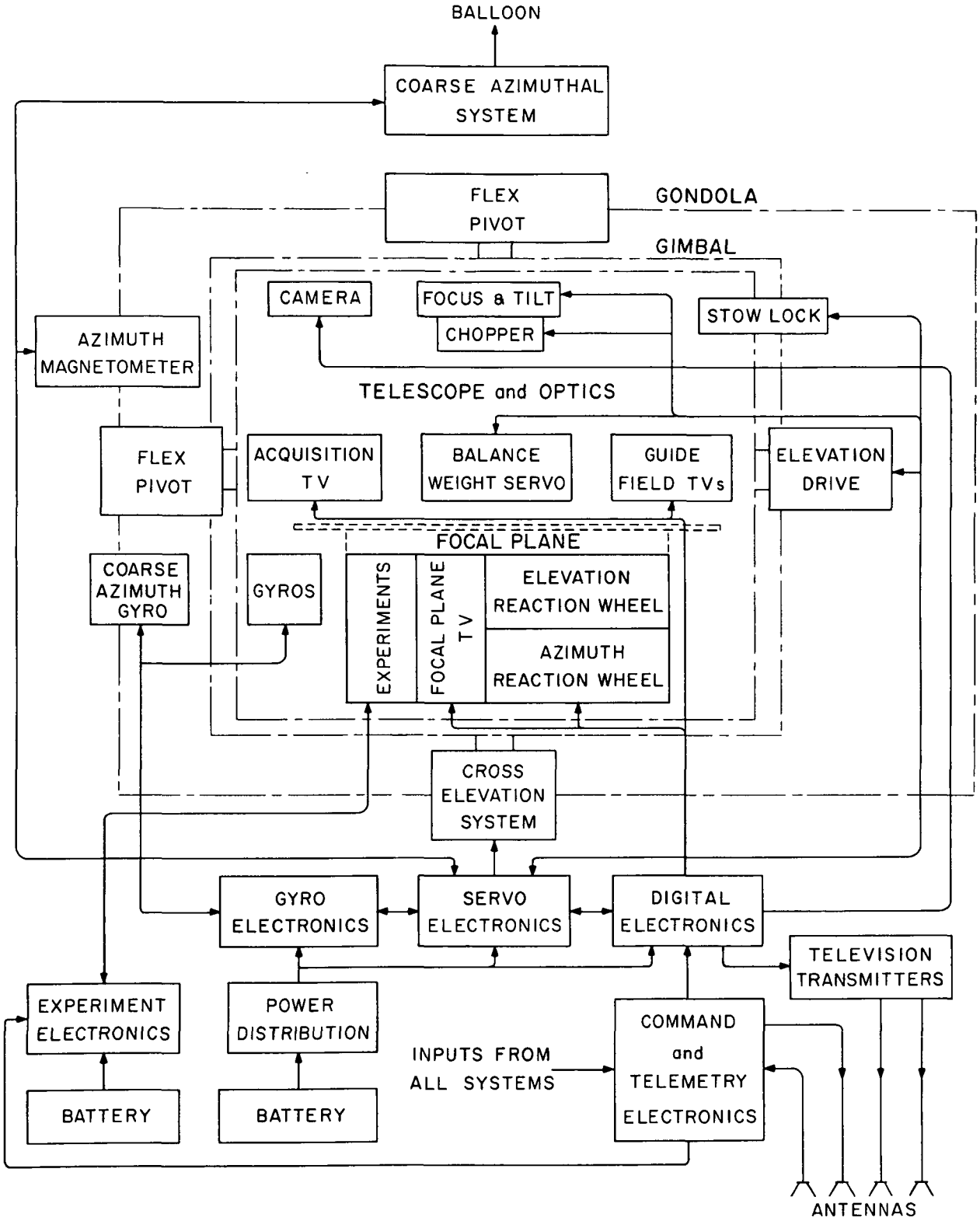

Figure 2.6-2. Gondola Electronics Systems

When the Three-Meter Balloon-Borne Telescope becomes fully operational, a silver-zinc battery set is planned which would greatly reduce the cost per flight without a significant weight increase.

2.6.4 Electronics Packaging

The yoke frame has been sized to provide an electronics cavity on each side of the gondola that can be thermally controlled, maintain atmospheric pressure and utilize standard 19-inch electronic racks. These enclosures begin just below the telescope elevation drive at a level easily accessible for ground maintenance and checkout. The volume available $0.34m^3$ ($12\ ft^3$) is more than sufficient to hold all system electronics, including any NSBF batteries which must be flown. The left side will be used for gondola equipment while the right side will be dedicated to experiments/hardware.

Table 2.6-1. Estimated Power Requirements

Assembly	Average Steady-State Power (Watts)
Azimuth Stabilization Drives	168
Elevation Stabilization Drives	56
Pointing and Guidance	84
Command System	28
Experiments	140*
Other Systems	84
. Chopping Secondary	
. Focus Drive	
. Heaters	
. Miscellaneous (Power Supply, Losses, etc.)	
Total Steady-State Power	560 watts

Estimated Power per Flight

. Preflight Checkout	1 hour = 560 watt-hours
. Ascent Power	1.5 hours = 252 watt-hours
. Experiment Power	11 hours = 6160 watt-hours
Total Energy Required	6972 watt-hours at 28 volts (249 ampere-hours)

*Will vary with experiment packages; quoted number is for dual photometer instrument, but can be as high as 425 watts for a heterodyne spectrometer.

3.0 MIRROR DEVELOPMENT PROGRAM

3.1 Approach and Scope

A number of unique requirements for the Three-Meter Balloon-Borne Telescope primary mirror have caused it to be identified as one of the critical items for attention during the definition study. It must:

1. be very lightweight. Preferably approximately 70 kg (10 kg per square meter).

2. maintain its figure at an operating temperature of -40 to -50 degrees Centigrade.

3. come to rapid thermal equilibrium during a two hour ascent from high summer temperatures through the tropopause to the operating temperature at 30-km altitude.

4. survive the high gravity loading during launch and at the time of parachute opening on descent and survive the landing impact shock.

An additional unique feature of this telescope is its 30-μm diffraction-limited performance requirement which places it in a domain between radio reflectors of considerably lower accuracy and optical telescopes of considerably higher accuracy, a domain which has had little attention for either ground-based or space applications. Because of the very similar reflector requirements for the Large Deployable Reflector (LDR), the balloon telescope development and test effort has potential impact on that future space facility.

The thrust of the mirror development program has been to measure the low temperature performance of state-of-the-art lightweight mirror materials and to work with manufacturers to further develop the technology. Initially we have been concerned more with the surface thermal stability, rather than the surface accuracy, other than being adequate for 10-μm interferometry. Our activities include:

1. Designing and constructing a thermally controlled test chamber for optical evaluation of very lightweight mirrors at low temperatures.

2. Testing a series of four 0.5-m replicated Carbon Fiber Reinforced Plastic (CFRP) 6-cm-thick aluminum honeycomb core sandwich mirror panels procured from Dornier Systems of West Germany. The panels are replicated from a convex Pyrex template with a 10-m radius of curvature. They were tested both for low temperature distortion and for deformation under mechanical load.

3. Testing additional Dornier CFRP panels procured by JPL in a complementary development effort.

4. Testing a CFRP sandwich panel with additional pyrex facesheets.

5. Testing a series of lightweight replicated CFRP panels made by Hexcel Corp. in a collaborative JPL/Hexcel/University of Arizona (UA) program.

6. Collaborating with United Technology Research Center in the development and testing of very lightweight "egg crate" mirror panels made of carbon fiber reinforced glass (TSC).

7. Procuring and testing an aluminum facesheet, foamed aluminum core mirror made by Energy Resources Group.

8. Evaluating a lightweight welded Pyrex mirror produced by the mirror group at the UA.

This overall program is partially supported by the definition study funds. At the time of preparing this report, item 1 above has been completed and is in operation. Items 2, 3 and 4 have produced test results on three mirror panels; items 5, 6 and 7 have been initiated; and item 8 has been pursued with regard to thermal transfer behavior as discussed in Section 2.2.4 and has been tested for low temperature performance in a separate NASA Ames Research Center (ARC) LDR-related program.

3.2 Preliminary Conclusions from Mirror Development Program

The mirrors that have been tested are:

1. QUAD 21, a 50-cm CFRP Dornier mirror panel

2. JPL #1, a 50-cm CFRP Dornier mirror panel

3. Pyrex/CFRP panel, a composite formed from a CFRP Sandwich with additional pyrex facesheets.

The Pyrex/CFRP composite demonstrated excessive low temperature deformation and, as constructed, is not a useful balloon-borne telescope mirror candidate. The two Dornier mirror panels gave less than 1 μm rms small-scale surface deformation at -60°C. Quad 21 low-temperature deformation was dominated by astigmatism while JPL #1 showed mainly a change in focus which agreed with the theoretical prediction. We conclude from these measurements that the state-of-the-art CFRP replicated mirror panels meet our requirement for small-scale thermal deformations and exhibit predictable large-scale deformation which can, in principle, be corrected for in the manufacturing design.

3.3 Low Temperature Test Chamber and CO_2 Laser Interferometer

At the initiation of this study, we were unable to find any facility for expeditious measurement of mirrors in the temperature range 20° to -60°C with an optical precision suitable for 30-μm diffraction-limited imaging. For that reason we set about to create such a test capability. We were encouraged in this by the availability at the KPNO of an optical test vacuum chamber large enough for containing a cooling shroud and the approximately 10-m long radius of curvature of test mirrors, and the availability from the UA Optical Sciences Center of a 10.6-μm CO_2 laser interferometer which is ideal for optical testing of mirrors of 30-μm diffraction-limited quality.

The specific requirements of the cooling chamber were that it accept a test mirror up to 50-cm square with a radius of curvature of approximately ten meters, that it cool the test mirror to any temperature from room temperature down to -60°C, that the mirror be cooled to a temperature uniformity of 0.1°C, that the nonuniformity of the radiative load from either the cooling chamber or from the window through which the optical beam passes be small enough not to compromise the temperature uniformity, and that the chamber itself be capable of -80°C to expedite cooling of the mirror.

During the design and fabrication of the cooling shroud, we concluded that operation in a vacuum was not essential, and that we could effectively and far more conveniently achieve the required goals with a foam insulated vertically oriented chamber which operates at atmospheric pressure. The following sections describe the design, fabrication, and performance of the resulting temperature controlled chamber.

3.3.1 General Design Considerations

Figure 3.3-1 shows the chamber as it is used to test mirrors with an infrared interferometer. A cross-section of the chamber is shown in Figure 3.3-2. This shows the plywood base, aluminum walls with U-channel clamps, copper headers for the cooling tubes, and coolant hoses with their threaded union fittings. The specifications are given in Table 3.3-1. An additional 30-cm height of insulation provides the transition region between the cooled walls and the room temperature window at the top of the chamber. A coolant, supplied by flexible tubing, circulates through the walls and base. Mirrors are lowered into the chamber by removing the window at the top.

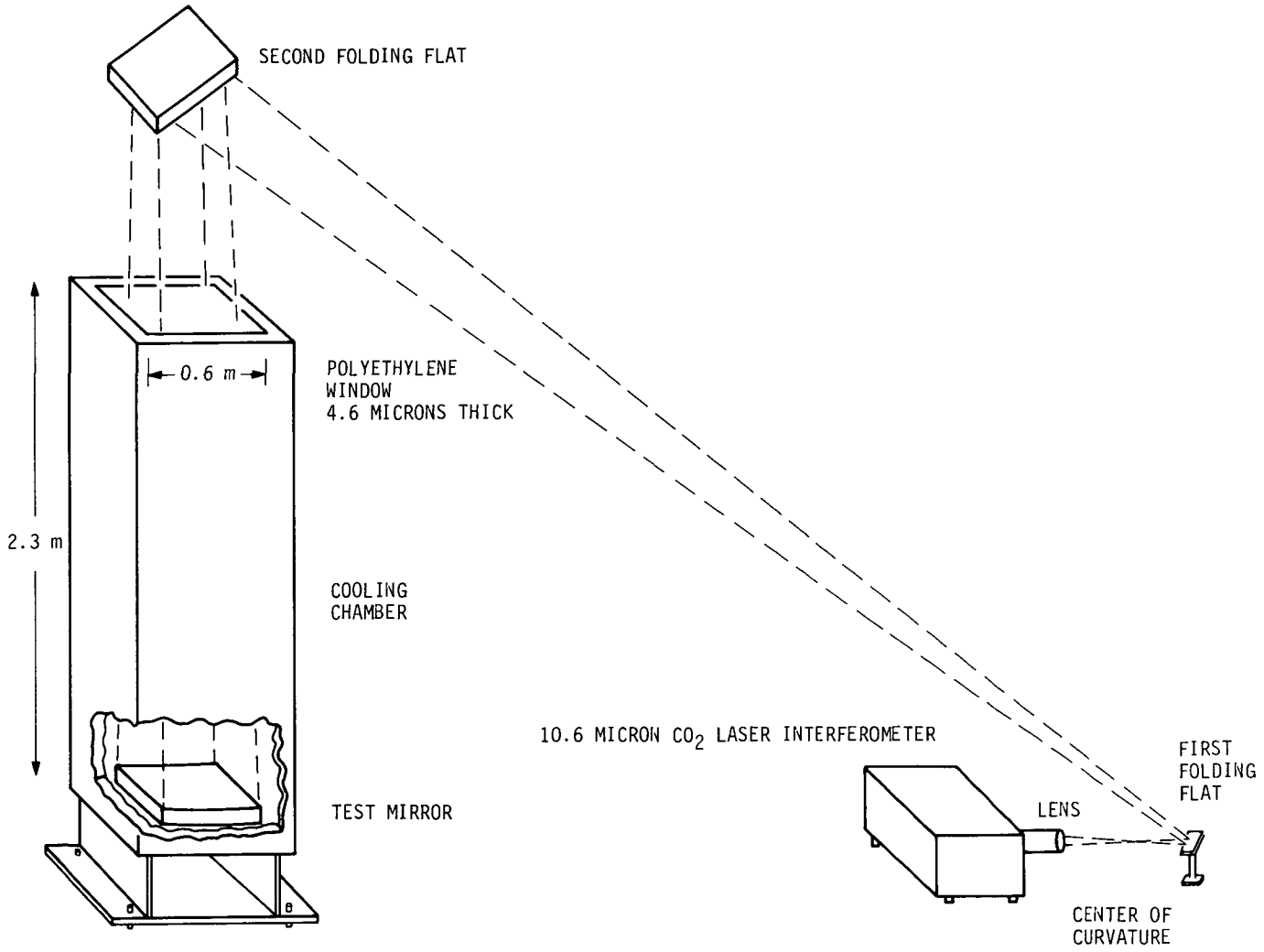

Figure 3.3-1. Mirror Test Configuration

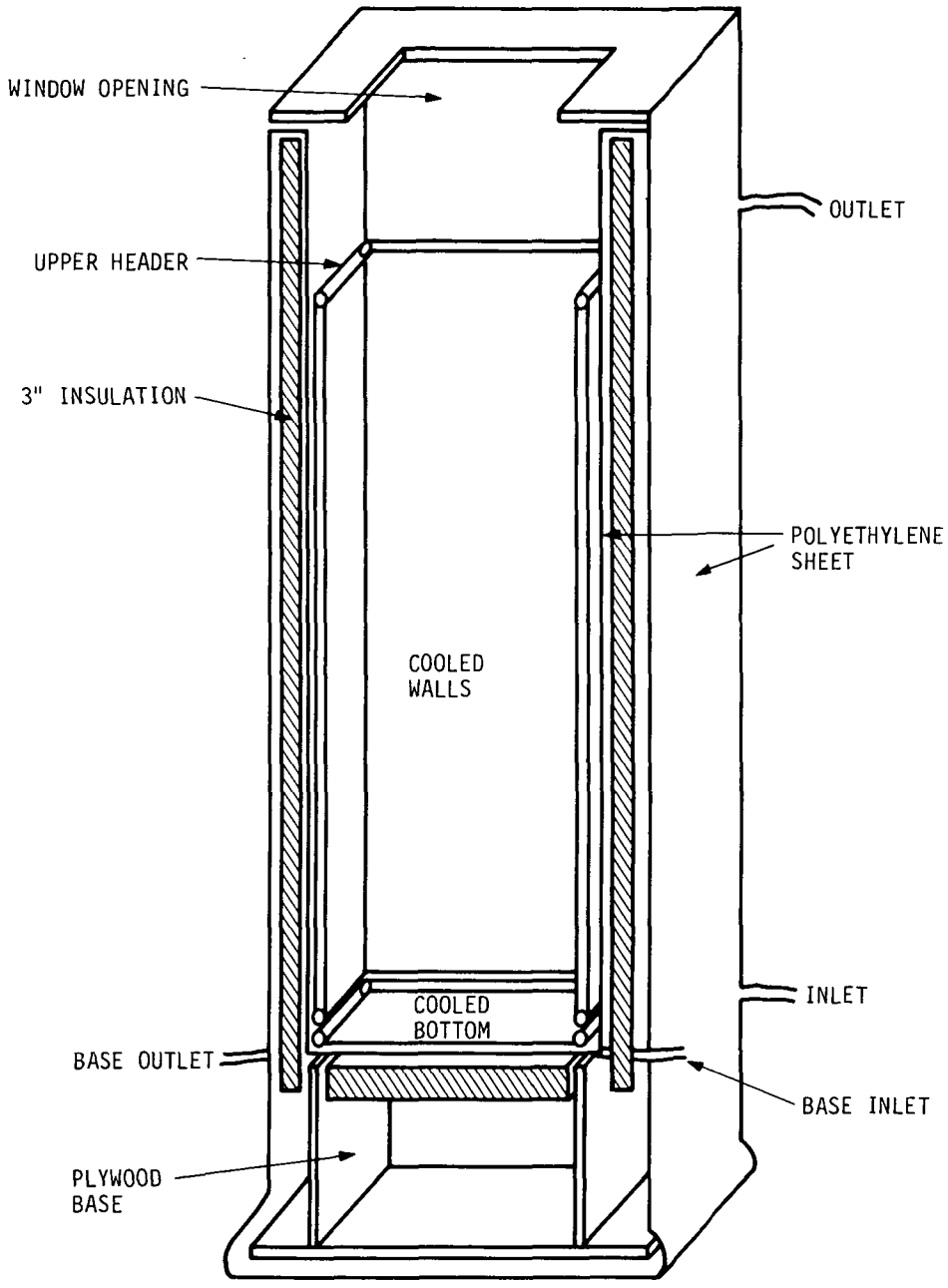

Figure 3.3-2. Mirror Test Chamber Cross Section

Table 3.3-1. Chamber Specifications

Cooled Volume	60 x 60 x 200 cm
Minimum Temperature	-80°C
Temperature Uniformity	± 0.1°C
Cooling and Heating Rate	2°C/minute
Window Size	53 cm square

Several general considerations have led to this configuration.

1. Atmospheric pressure operation. Most low temperature environmental chambers operate with a vacuum in order to provide thermal isolation, temperature uniformity, freedom from moisture condensation, and freedom from circulating air currents. However, it is possible to achieve these goals without a vacuum if the following requirements are met: 1) the chamber is vertical with a room temperature window at the top; 2) the chamber is operated always at or below room temperature; 3) the cooled part of the temperature chamber has walls of uniform temperature with no horizontal temperature gradients and, if it exists, only a positive vertical temperature gradient; 4) the chamber is well insulated and has no air leaks which would permit low density warm air to stream into the chamber; and 5) the chamber is adequately dried with a desiccant before using. In this way the chamber acts much like a vacuum thermos bottle with a cold fluid at the bottom and a stable non-convective layer of air from the surface of the fluid to the top of the flask.

2. Cooled walls. The only satisfactory way to achieve high temperature uniformity is to surround the chamber with an isothermal conducting wall rather than circulating cooled air through it. We have chosen two sheets of aluminum for the walls with copper coolant tubing sandwiched between them.

3. High flow-rate coolant. To achieve temperature uniformity of the chamber walls in close contact with the coolant, the coolant must exit at nearly the same temperature it enters the chamber. This requires a very high mass flow rate of coolant to ensure the heat load can be absorbed with a very small temperature increase in the coolant.

4. Turbulent flow. A second aspect of providing uniform wall temperatures is to ensure that the temperature difference between the coolant fluid and the chamber wall is small. This can be achieved by maintaining turbulent flow in the cooling tubes so that the coolant makes maximum contact with the wall of the tubes.

5. Liquid nitrogen as the cooling source. For intermittent use it is far more convenient and economical to utilize liquid nitrogen for the cooling rather than a closed circuit refrigeration system. We achieve this with a tube and shell counter flow heat exchanger between the liquid nitrogen supply and the circulating coolant.

3.3.2 Insulation and Heat Load

The chamber bottom and sides are insulated with polyisocyanurate foam sheets one-inch thick with reflecting aluminum foil on both faces. The wall insulation consists of three layers taped at all the joints. On the bottom there are three layers. In addition, to ensure no air leaks, the metal walls of the chamber are sealed with RTV or aluminum tape at each joint and the chamber is enclosed in a sealed polyethylene "bag" fitting between the chamber walls and the insulation. The top of the chamber is insulated by 36 cm of dead air between the upper edge of the cooled walls and a 4.6-μm-thick polyethylene window. To prevent moisture from penetrating the insulation or condensing on cold plumbing, the entire assembly is wrapped in a second polyethylene bag. The polyethylene used for sealing is typically 0.1-mm thick.

3.3.3 Desiccant

Adequate drying of the chamber before use is critical. We have chosen calcium sulfate, using 6 kg in sausage-shaped fiberglass bags hung in the corners of the chamber and an additional 3 kg around the base within the outer polyethylene bag. At room temperature calcium sulfate can reduce the moisture content of the air to .005 mg per liter, which represents a dew point near -80°C. Calcium sulfate can absorb .1 g of water per gram of desiccant. The moisture contained in the .92 cubic meters of air at 100% relative humidity, room temperature, is 18 g, much less than the 600-g capacity of 6 kg of calcium sulfide. We have found that in Tucson the chamber is adequately dried in a few hours (to <1% relative humidity). This approach appears to be simpler and more convenient than attempts to purge with a dry gas. To purge with dry gas from 30% relative humidity at room temperature (5.4 mg per liter) to the required .005 mg per liter would require replacing all but 0.1% of the atmosphere with the purging gas, a difficult level to achieve without vacuum purging. In addition, the purge would have to be continuous because of the release of moisture from the surfaces within the chamber.

3.3.4 Chamber Walls

A photograph of a short prototype section of the chamber walls is shown in Figure 3.3-3. This shows two 1.6-mm-thick sheets of aluminum sheet separated by the copper tubing and clamped together with 3/4- by 1/2-inch aluminum U channels and nylon screws. Each side of the walls contains five vertical copper tubes of 1/4-inch OD and 3/16-inch ID. The spacing between tubes on the walls was chosen so that with the expected heat load the temperature difference over the wall from midway between the two tubes to the tubing would be less than 0.1°C on the aluminum sheet intercepting the heat load.

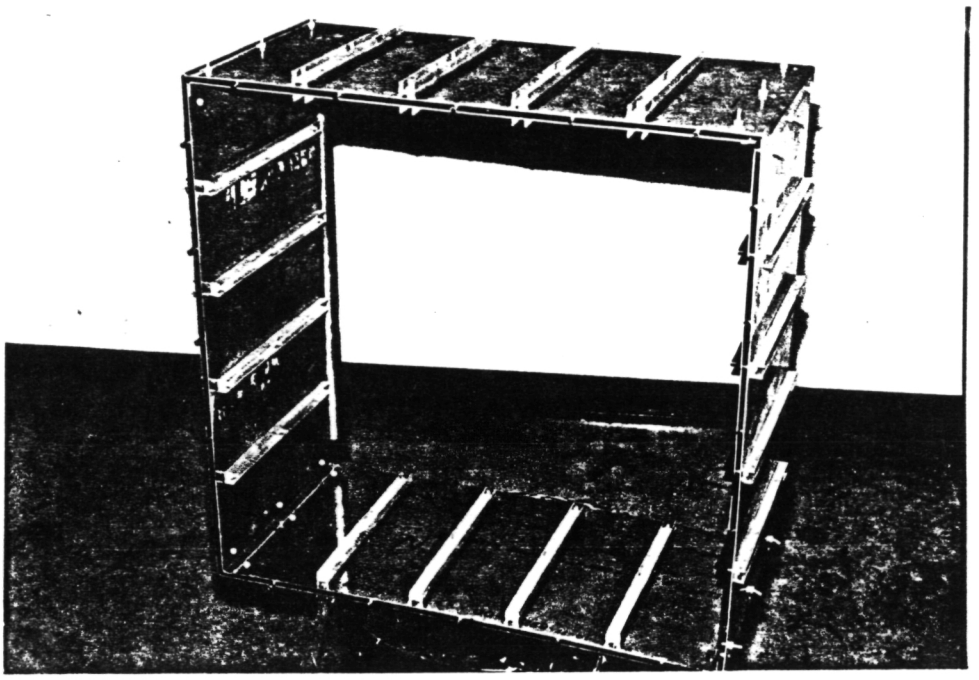

Figure 3.3-3. Photograph of a Prototype Section of the Chamber Wall Showing Cooling Tubes and U-Channel Clamps.

3.3.5 The Coolant Circulation

We have considered a number of potential coolants which have satisfactory heat transfer properties and viscosity over our temperature range -80°C to room temperature, such as Dowtherm J and Freon 11. For our initial operation, for convenience, we have chosen a mixture of 80% ethyl - 20% methyl alcohols. The mixture permits us to operate about 20° lower in temperature than pure ethyl alcohol and is satisfactory to -80°C. The properties of the mixture as a coolant are given in Table 3.3-2. In addition, to assure the effective transfer of heat from the copper tube to the circulating coolant we chose to have the coolant in turbulent flow through the cooling tubes. This dictated the tube size choices and velocity rates. With the mass flow rate given in Table 3.3-2 and required tubing sizes for turbulent flow we expect a pressure drop throughout the system of 10 to 40 lbs. psi over the operating temperature range. To provide the flow with this pressure drop we have chosen a positive displacement gear pump Teel model IP776 which provides a flow rate of 1,500 cubic centimeters per second at 1725 RPM. It is driven by a 3/4 horsepower electric motor. The coolant is maintained at a 2 psi overall positive pressure with an elevated supply reservoir. This is shown in Figure 3.3-4.

Table 3.3-2. Properties of Coolant 80% Ethyl - 20% Methyl Alcohols

Density (grams/cc) @ 20°C	0.79	0.79
Heat capacity (Joules/g°C)	2.6	2.5
Viscosity (centipoise)		
20°C	1.2	0.6
-60°C	8.4	3.0
Mass flow rate required by coolant to remove 241 W with .1° temperature change (g/sec)	960	
Volume flow rate required by coolant (cc/sec)	1,200	

3.3.6 Cooling and Heating

The cooling is provided with liquid nitrogen in a heat exchanger shown schematically in Figure 3.3-4. The coolant flows through 31 3/16-inch ID tubes in the heat exchanger. Liquid nitrogen is fed into the bottom of the heat exchanger shell around the tubes where it quickly evaporates. The nitrogen gas is vented at the top of the heat exchanger through a flow rate control valve and a cryogenic solenoid on/off valve that provides duty cycle cooling control. A pop valve defines the upper pressure limit for the shell side of the heat exchanger. The heat is provided by two 100-ft.

lengths of insulated resistance wire wrapped on two 30-inch-long 1-inch-diameter copper tubes in the circulation system. They are capable of 2,000 W each.

3.3.7 Temperature Measurement and Control

Throughout the system we use YSI 44003A 1K thermistors for temperature measurement. The thermistors are manufactured with sufficient quality control that those from a single batch track the standard calibration provided by the manufacturer together to within less than a 0.1°C difference. A General Automation 16/65 mini-computer is used for monitoring and controlling the chamber temperature. The monitoring is accomplished by sampling the voltages from the temperature sensors once per second with a 16-bit A/D converter. The temperature of the chamber is controlled by a variable duty cycle on the cryogenic solenoid and a heater control relay. In addition, a feedback term equal to the integral past differences is included to assure zero error during steady-state controlling conditions.

3.3.8 Chamber Performance

The chamber has achieved a temperature uniformity of 0.1°C over the range 21°C to -60°C. It can be readily heated or cooled at 2°C per minute and operated satisfactorily from room temperature down to -80°C. In cooling we normally run the chamber to 15° cooler than the desired mirror temperature to accelerate cooling of the mirror until it has nearly reached the desired temperature. Then the chamber temperature is raised to the final mirror temperature. Typically, the entire cycle from cooling from one temperature to another and reaching stable 0.1°C isothermal conditions on the mirror is one hour. The total consumption of liquid nitrogen for optical measurements at a sequence of 5 or 6 different temperatures over a period of 6 hours is approximately 100 liters.

3.3.9 10.6-Micron Laser Phase Modulated Interferometer

The mirror test configuration is shown in Figure 3.3-1. Measurements of the surface error are made with a phase modulated 10.6-μm CO_2 laser interferometer constructed by the UA Optical Sciences Center. The interferometer provides a comparison between the curved mirror surface and a spherical wave front generated by the diverger lens in the interferometer. It is shown in Figure 3.3-5.

The test procedure involves photographing a number of interferograms for each temperature setting of the chamber. Subsequently, the interferograms are digitized and analyzed by the FRINGE program of the Optical Sciences Center. This program fits the fringe pattern to a set of up to 36 Zernike polynomials which provides for convenient smoothing, data manipula-

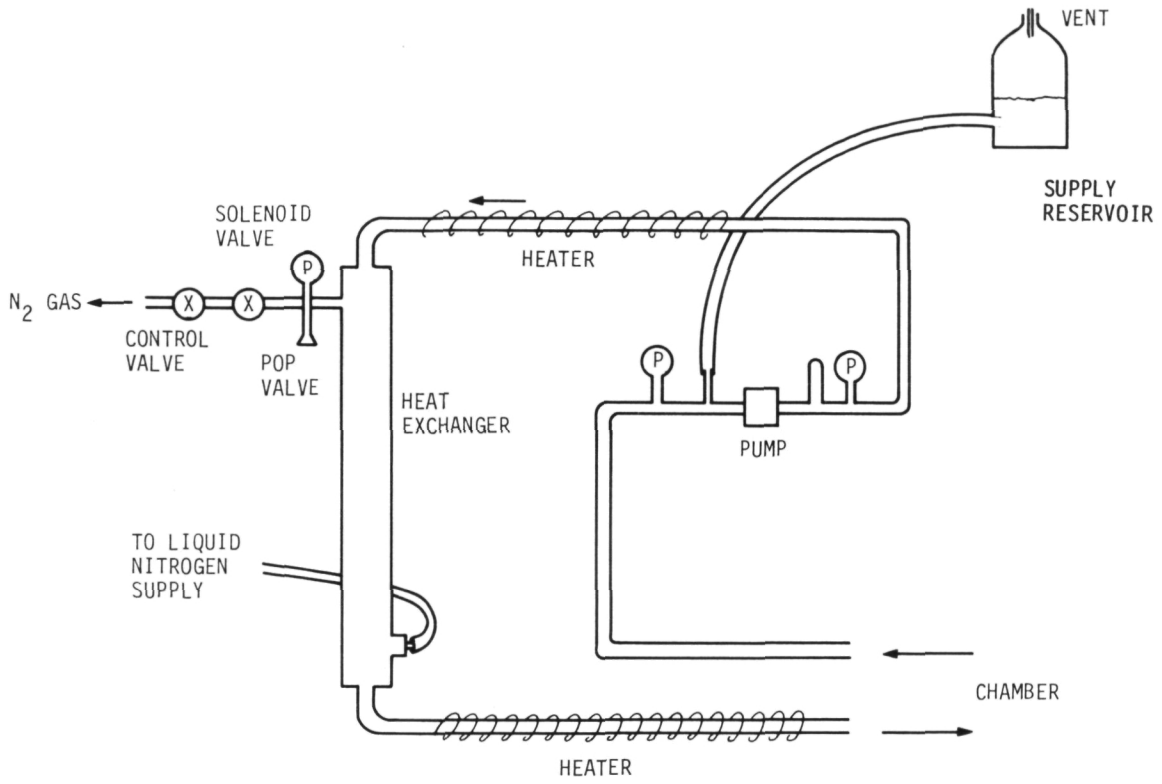

Figure 3.3-4. Schematic Diagram of Coolant Circuit

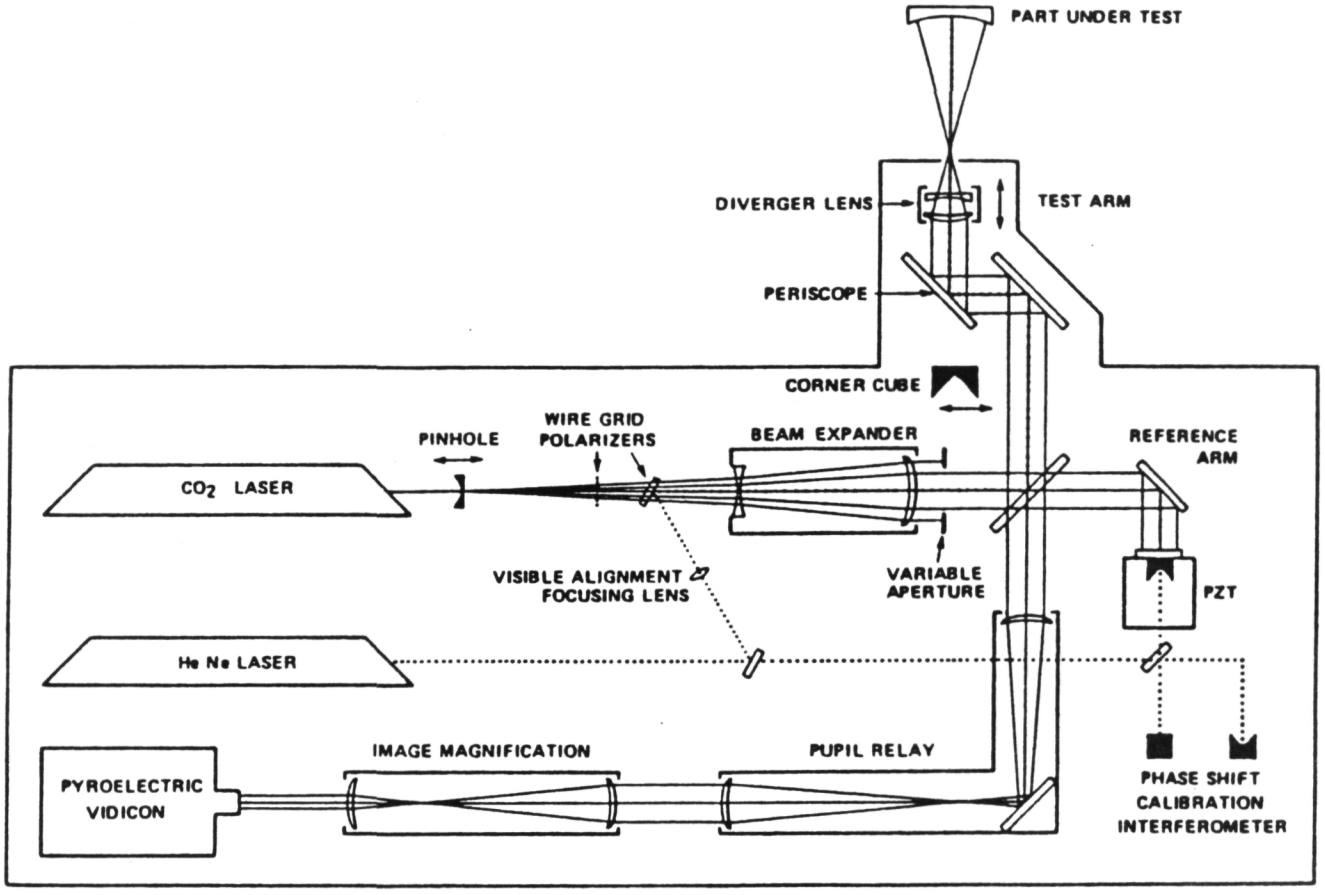

Figure 3.3-5. Phase Modulated Interferometer

tion, and evaluation of the large-scale distortions. In particular, it is possible to remove the effect of an arbitrary tilt of the mirror prior to evaluating the distortion of its shape and to remove specific large-scale distortions such as astigmatism and focus before calculating the rms deviation of the residual errors. In addition, it is convenient to obtain differences of interferograms to observe changes in the surface errors with temperature. The 36 polynomials can represent surface deformation with up to six waves across the diameter and five waves azimuthally.

3.4 Figure Stability of Carbon Fiber Reinforced Plastic Mirror Panels

3.4.1 Low Temperature Performance of Dornier Panel "Quad 21"

Tests of Dornier panel Quad 21 were carried out October 18, 1984. Interferograms were obtained at five temperatures with three interferograms each at 24.4°C, -1.4°C, -33.6°C, -56.4°C, and two additional interferograms obtained after the mirror returned to room temperature at 24.3°C. All interferograms were analyzed over a circle tangent to the edges of the square panel. The Zernike polynomial coefficients beyond the 15th term were all small (typically 0.2 μm) and less than or equal to the standard deviation of the average. Therefore, we have used only 15-term fit in our analysis. This includes radial distortions across the diameter of 4 waves and azimuthal distortions of 4 waves. Since we are primarily interested in the figure changes with temperature, we have used the first room temperature measurement as a baseline, subtracting this surface shape from those of the remaining observations. The second room temperature measurement provides an indication of the consistency of the measurements and potential hysteresis.

The results are shown in Table 3.4-1 and Figures 3.4-1 and 3.4-2. Figure 3.4-3 gives the initial mirror figure error as replicated. Figure 3.4-4 shows a sample of the interferograms. These include errors due to the second folding flat, a non-optical quality sheet of plate glass. Table 3.4-1 and Figure 3.4-1 give the astigmatism, astigmatism angle, focus change (not including the effect of astigmatism), and the residual rms surface error after removing astigmatism and defocus. The error bars in Figure 3.4-1 are determined from the standard deviation from the three interferograms at each temperature. From Figure 3.4-1 we can see the following:

Table 3.4-1. Quad 21 Mirror Figure Change with Temperature

Temperature (°C)	-1.4	-33.6	-56.4	24.3
Astigmatism (μm)	15.0±1	32.4±3.4	45.2±1.2	2.2±2.8
Astigmatism Angle (degrees)	54±3	51±4.0	46±1	-57
Focus (μm)	-.46±.6	-2.8±1.8	-6.6±.8	.06±1
Residual Error rms (μm)	.5±.3	1.2±0.5	1.6±.4	1.4±1.4

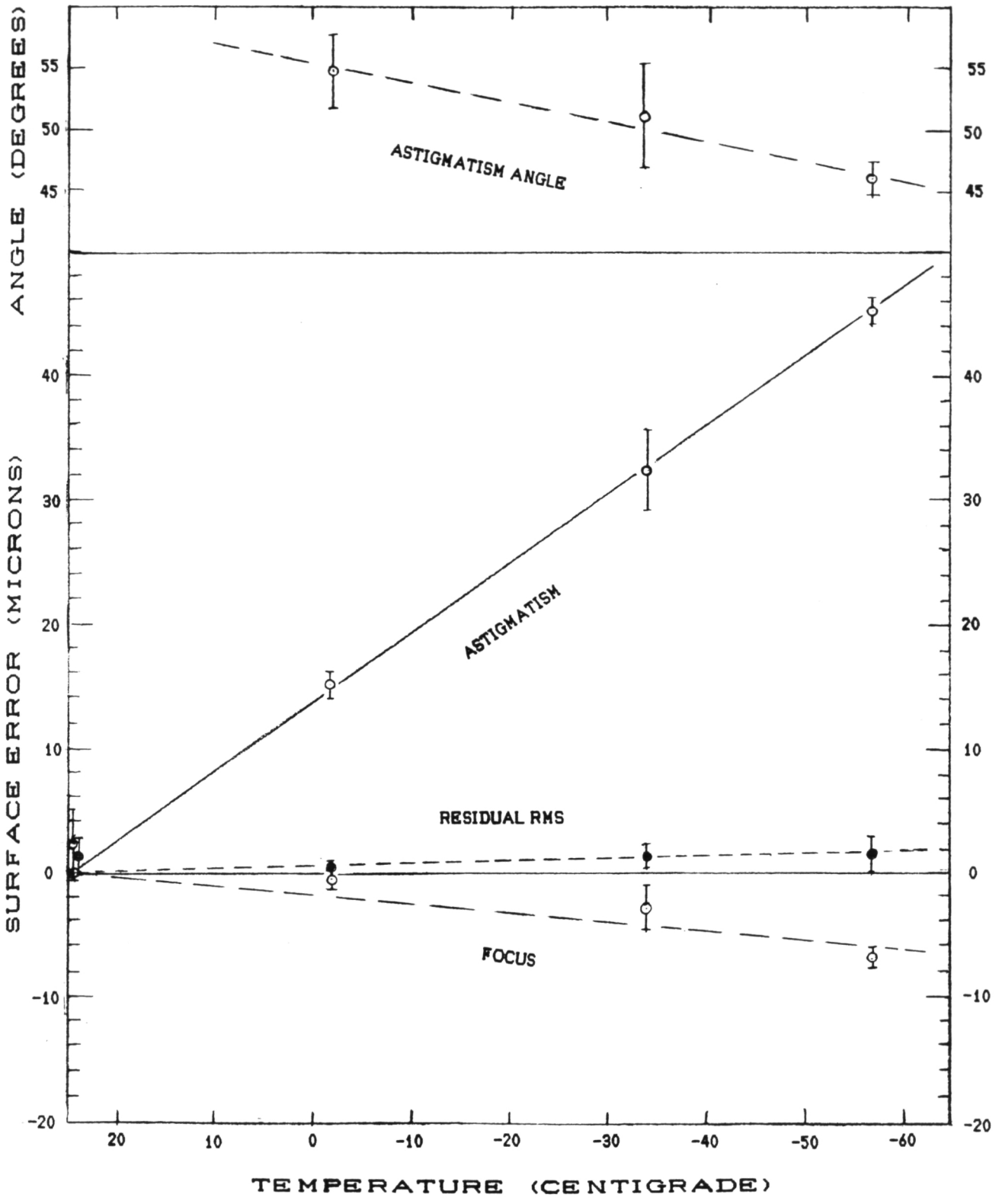

Figure 3.4-1. Quad 21 Test Panel Figure Change with Temperature

QUAD 21
DOMINER

CONTOUR LEVELS

	Waves	Microns
3	2.9	30.7
2	2.7	28.6
1	2.5	26.5
0	2.3	24.4
Z	2.1	22.3
Y	1.9	20.1
X	1.7	18.0
W	1.5	15.9
V	1.3	13.8
U	1.1	11.7
T	.9	9.5
S	.7	7.4
R	.5	5.3
Q	.3	3.2
P	.1	1.1
N	-.1	-1.1
M	-.3	-3.2
L	-.5	-5.3
K	-.7	-7.4
J	-.9	-9.5
I	-1.1	-11.7
H	-1.3	-13.8

Figure 3.4-2. Example of Quad 21 Performance at Coldest Test Temperature

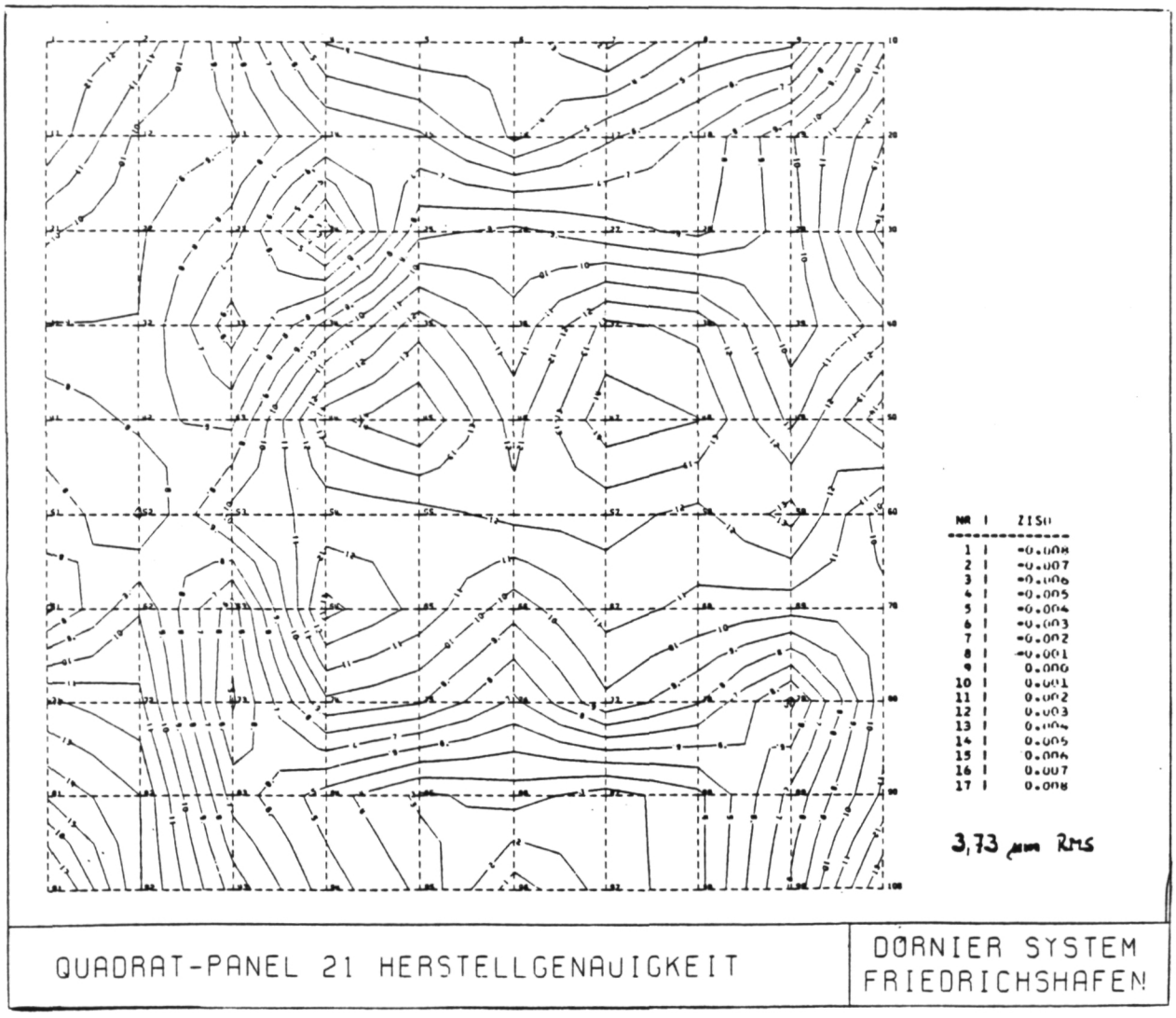

Figure 3.4-3. Initial Quad 21 Mirror Test Panel Figure as Replicated

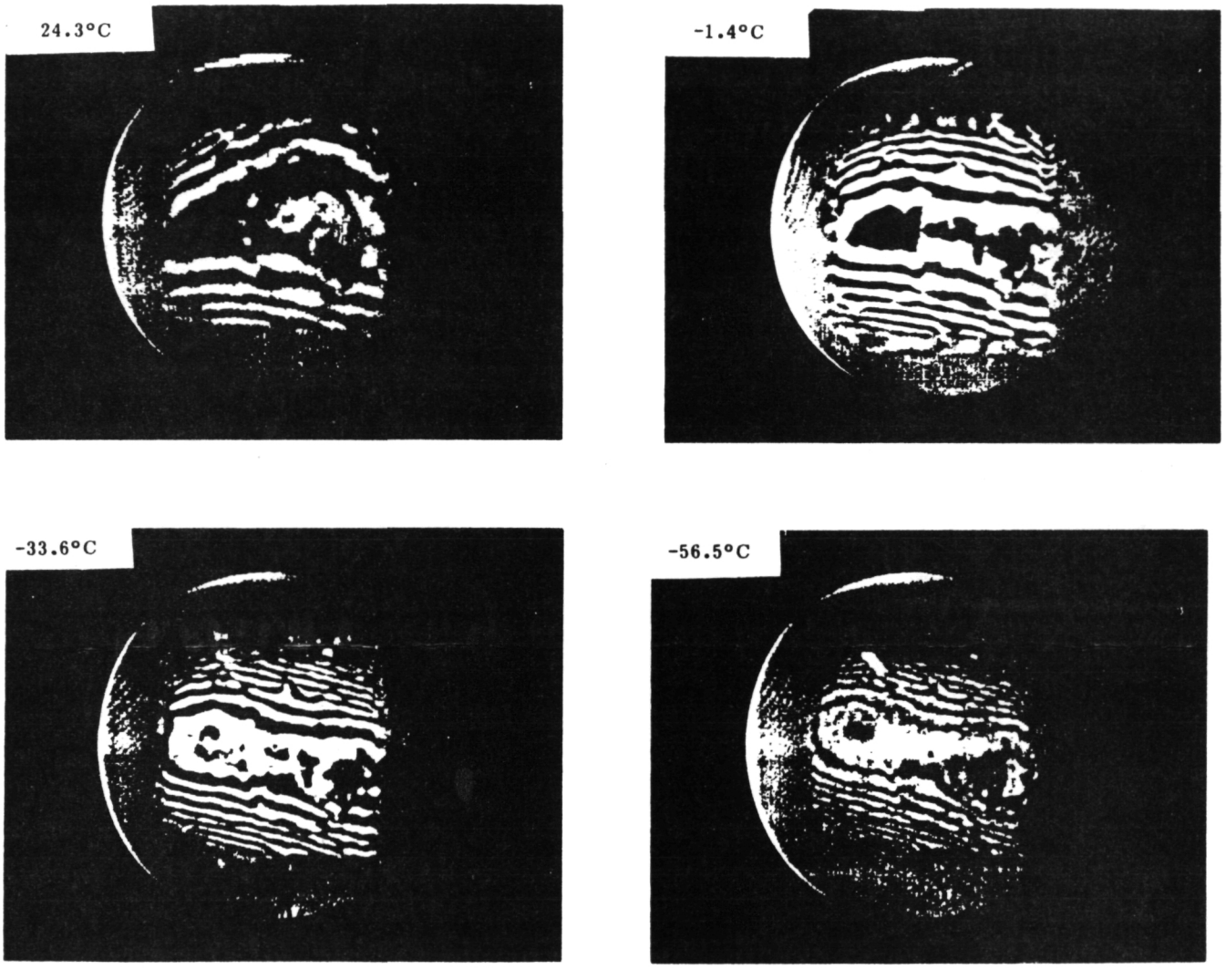

Figure 3.4-4. Interferograms of Mirror Quad 21

1) The distortion is dominated by a cylindrical warping of the panel which produces the astigmatism. It is 45.2-μm deep at -57°. The astigmatism angle changes slowly with temperature. The sense of the warping is for two opposite edges to curl up.

2) In addition to the cylindrical warping there is a saddle distortion (see Figure 3.4-2), which gives rise to a focus change in the sense of flattening the mirror. This focus change is, within the noise, nearly linear.

3) The residual rms error increases linearly to 1.6-μm rms at -56.4°C. The contour map for the second room temperature measurement is dominated by the 9th and 10th Zernike polynomials. Both have standard deviations larger than the coefficient and hence represent measurement noise.

Conclusions from thermal test of Quad 21: We are able to cool a CFRP mirror to -60° with a uniformity of $\pm$.05°C. The mirror distortion is dominated by the large-scale effect of cylindrical warping. The focus change could be a secondary effect of the cylindrical warping. The only evidence for higher order distortions is the residual rms surface error which increases with temperature (1.6 μm at -56.4°C). The mirror distortion is thus mainly large scale and due to the design, rather than quality control material uniformity.

3.4.2 Performance Under Mechanical Load of Dornier Panel "Quad 21"

We believe that the thermal distortion measured in Quad 21 at -60°C is largely due to the aluminum core and in particular the anisotropy of the core in the plane of the mirror. This causes an anisotropic stress in the mirror as the aluminum contracts differentially more than the CFRP facesheets. In response to the stress, the anisotropic core results in an even stronger anisotropic strain revealed as the cylindrical warping. As a consequence of this belief, we felt it desirable to also measure the panel under a symmetrical mechanical load to observe the anisotropy of its deformation.

Tests were carried out with the same CO_2 laser interferometer system used for the thermal tests. In this case, all the measurements were made at room temperature. The panel was supported on a bicycle inner tube of overall diameter 44.6 cm and tube diameter 2.9 cm to provide a uniform circular edge support. A 10-cm diameter foam pad and plywood disk was placed at the center of the pane for lead weights to rest on.

The tests of the deformation of Dornier panel Quad 21 under load were carried out on November 27, 1984. Interferograms were obtained for four conditions: initial unloaded mirror, a loading of 11 kg, a loading of 22 kg and final unloaded mirror. These loads are to be compared with the weight of the panel itself of 2.3 kg. All interferograms were analyzed over a 46-cm diameter circle centered on the square panel. As with previous analysis only the first fifteen terms of the Zernike polynomial coefficients were utilized in the analysis. The results are shown in Table 3.4-2, and Figures 3.4-5 and 3.4-6. Figure 3.4-5 is an interferogram of the

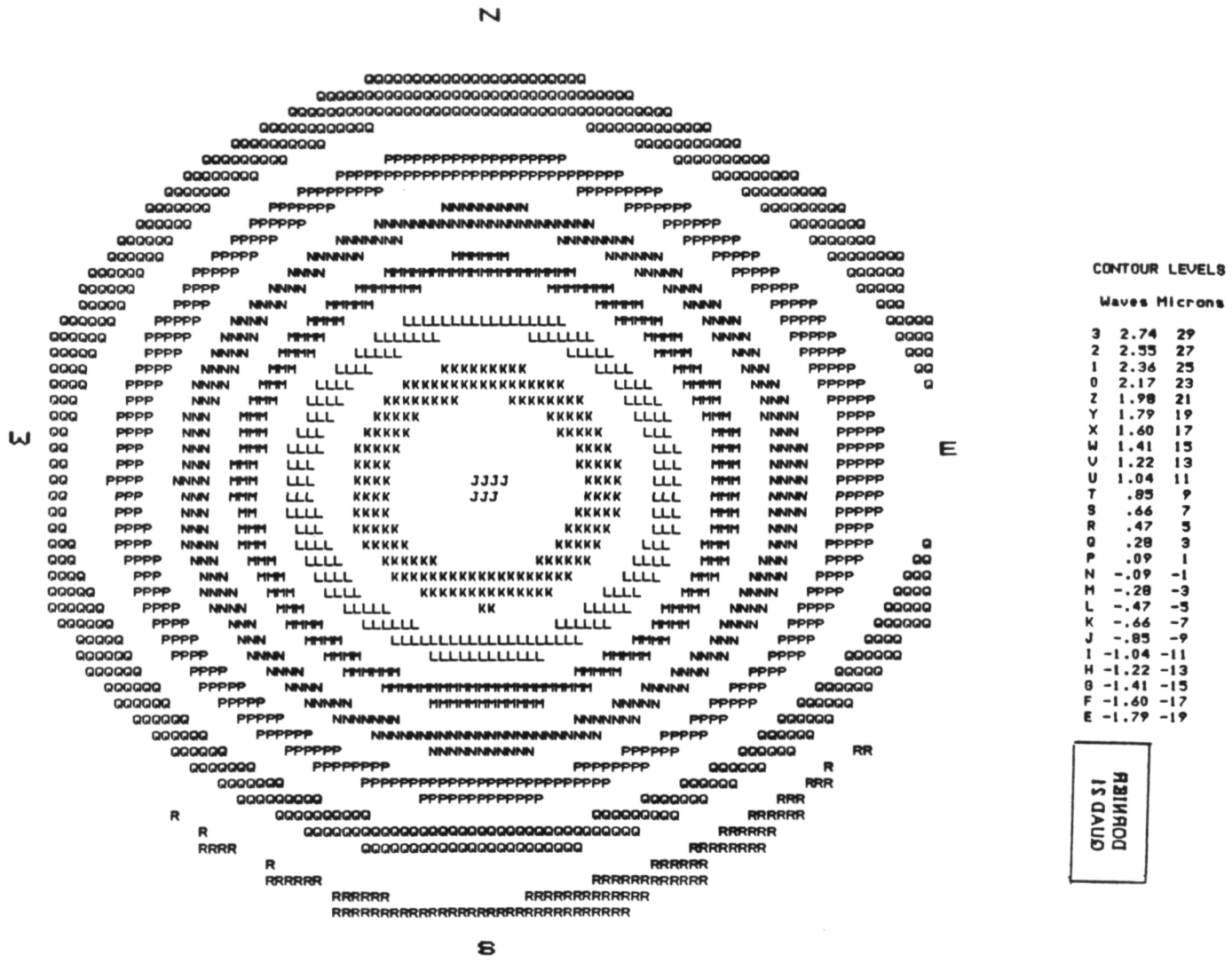

Figure 3.4-5. Quad 21 Figure Change with 22-kg Center Load Relative to No Load

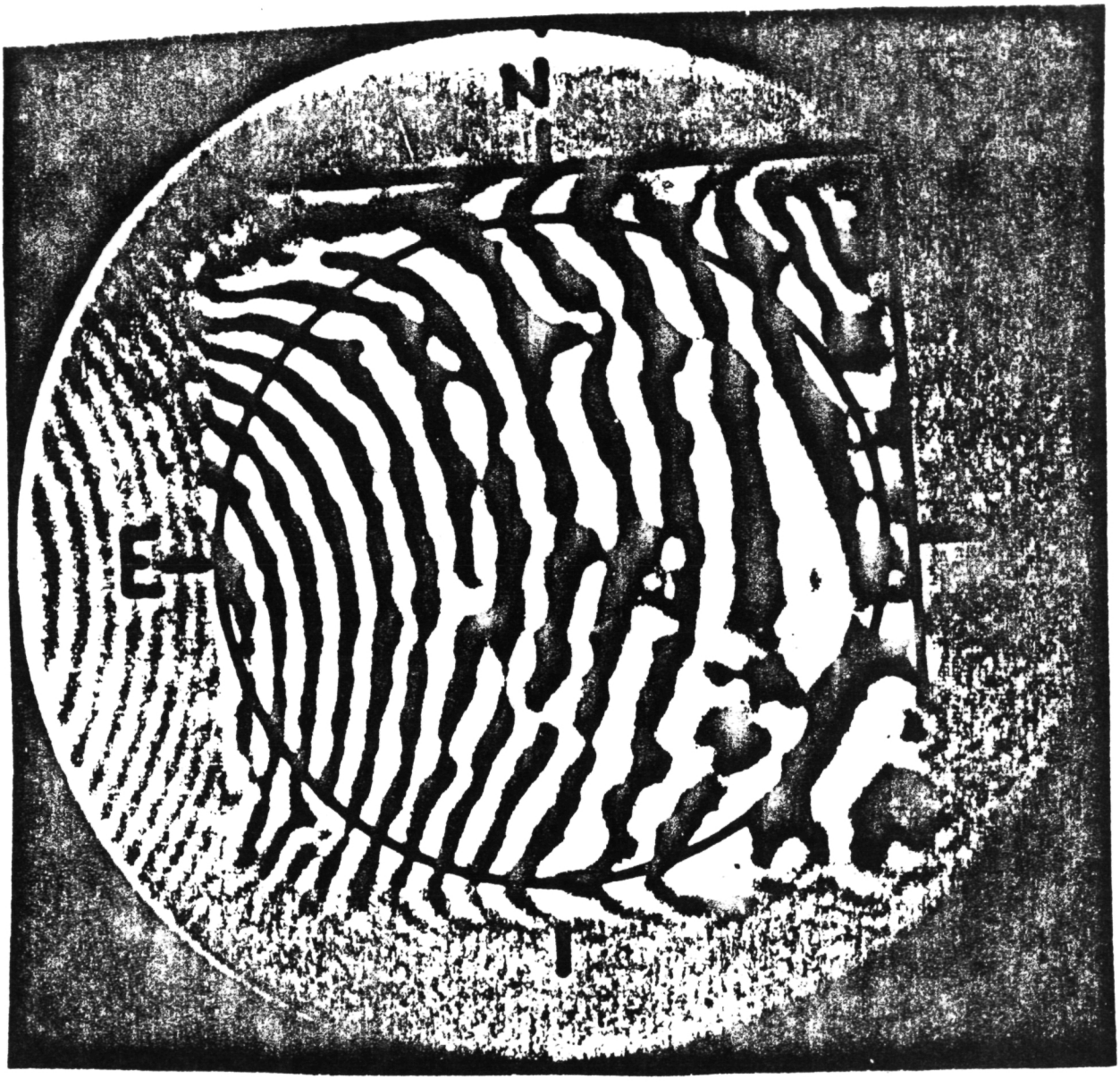

Figure 3.4-6. Interferogram of Unloaded Mirror Quad 21 Showing Circle Over Which Fringes Are Analyzed

unloaded panel showing the circle over which the fringes were analyzed. Table 3.4-2 gives the focus change, spherical aberration, astigmatism, and astigmatism angle. The errors are determined from the standard deviation from two interferograms which were averaged for each configuration. Algebraic expressions for the Zernike polynomials with their coefficients and expressions for the items in Table 3.4-2 are given in Table 3.4-3. The focus term has been corrected for the motion of the panel caused by the squeezing of the inner tube as the panel is loaded. This reduces the focus term by 1.4 μm. It has not been applied to Figure 3.4-5.

From these data we can see the following:

1) The distortion is dominated by a symmetrical dishing in the panel resulting in primarily a focus change which is 10.8-μm deep at the maximum load of 22 kg.
2) In addition, there is a symmetrical spherical aberration term of peak-to-peak 3.2 μm at the 22-kg load.

Under symmetrical load, the panel Quad 21 deforms in a remarkably symmetrical manner showing mainly focus and spherical aberration change. Thus, under symmetrical mechanical load, Quad 21 provides no evidence for the asymmetrical properties which give rise to asymmetrical deformation under thermal load. The panel is very stiff, deflecting only 10.8 μm with a 22-kg load.

Table 3.4-2. Quad 21 Mirror Figure Change With Load

Load (kg)	11	22	0
Focus change (μm)	5.5 $\pm$ .5	10.8 $\pm$ .8	1.2 $\pm$ 1.0
Spherical Aberration (μm)	-1.2 $\pm$ .2	-3.2 $\pm$ .3	.4 $\pm$ .4
Astigmatism (μm)	.52 $\pm$ 1.0	2.3 $\pm$ 1.9	2.0 $\pm$ 3
Astigmatism Angle (degrees)	-27	+4	-52

Table 3.4-3. Dominant Zernike Polynomials and Their Coefficients for Quad 21 Under Load

Term	Coefficient (μm)			
	11 kg	22 kg	0 kg	Polynomial
A3	2.76	5.4	.61	$2r^2-1$
A4	-.23	-1.17	-.61	$r^2\cos(2\theta)$
A5	.12	-.07	.76	$r^2\sin(2\theta)$
A8	-.77	-2.11	.25	$6r^4-6r^2+1$

Focus = 2A3

Astigmatism = $\sqrt{(2A4)^2 + (2A5)^2}$

Spherical Aberration = (3/2)A8

3.4.3 Low Temperature Performance of Dornier Panel JPL #1

Tests of the Dornier panel JPL #1 were carried out November 30, 1984, with the assistance of JPL. Four interferograms were obtained at each of the five temperatures 21.3°C, -7.5°C, -34.5°C, -56.2°C, and 21.0°C. All interferograms were analyzed over a circle approximately tangent to the edges of the square panel. As with Quad 21, we have used only the first 15 terms of the Zernike polynomial coefficients in the analysis. Again, since we are primarily interested in the figure changes with temperature, we have used the first room temperature measurement as a baseline, subtracting this surface shape from those of the remaining observations. The second room temperature measurement provides an indication of the consistency of the measurements and the potential hysteresis.

The results are shown in Table 3.4-4 and Figures 3.4-7 and 3.4-8. Figure 3.4-9 shows an interferogram with the "tangent" circle drawn. This figure also shows the problems with the replication accuracy near the edge of the mirror which was not usable for interferometry. Figure 3.4-8 shows the surface deviation from the initial room temperature surface to the surface at -56.2°C. Table 3.4-4 and Figure 3.4-7 give the focus change astigmatism, astigmatism angle, and rms surface change both including focus and astigmatism and with these terms removed. The errors shown in Table 3.4-4 and in Figure 3.4-7 are determined from the standard deviations from the interferograms averaged for each temperature. Although four interferograms were taken for each temperature, only two have been analyzed for this report.

Table 3.4-4. JPL #1 Mirror Figure Change with Temperature

Temperature (°C)	-7.5	-34.5	-56.2	20.0
Focus (μm)	3.0±.5	2.9±0.9	7.8±1.8	-0.4±0.5
Astigmatism (μm)	1.7±1.2	2.8±1.8	3.1±2.8	0.9±0.6
Astigmatism angle (degrees)	-58	-60	4	19
RMS Figure change including Astigmatism and Focus (μm)	1.0	1.2	2.5	0.3
RMS Figure change with Astigmatism and Focus removed (μm)	0.4	0.6	0.8	0.2

From Figure 3.4-7 and Table 3.4-4 we can see the following:

1) The uncertainty in the values of the focus and astigmatism change are large, in some cases larger than the terms themselves. The astigmatism angle probably has no significance. This appears to be partly due to the poor replication accuracy of the panel which causes a breakup of the fringes as shown in Figure 3.4-8, resulting in difficulty in following the fringe pattern. This problem is worse at the lower

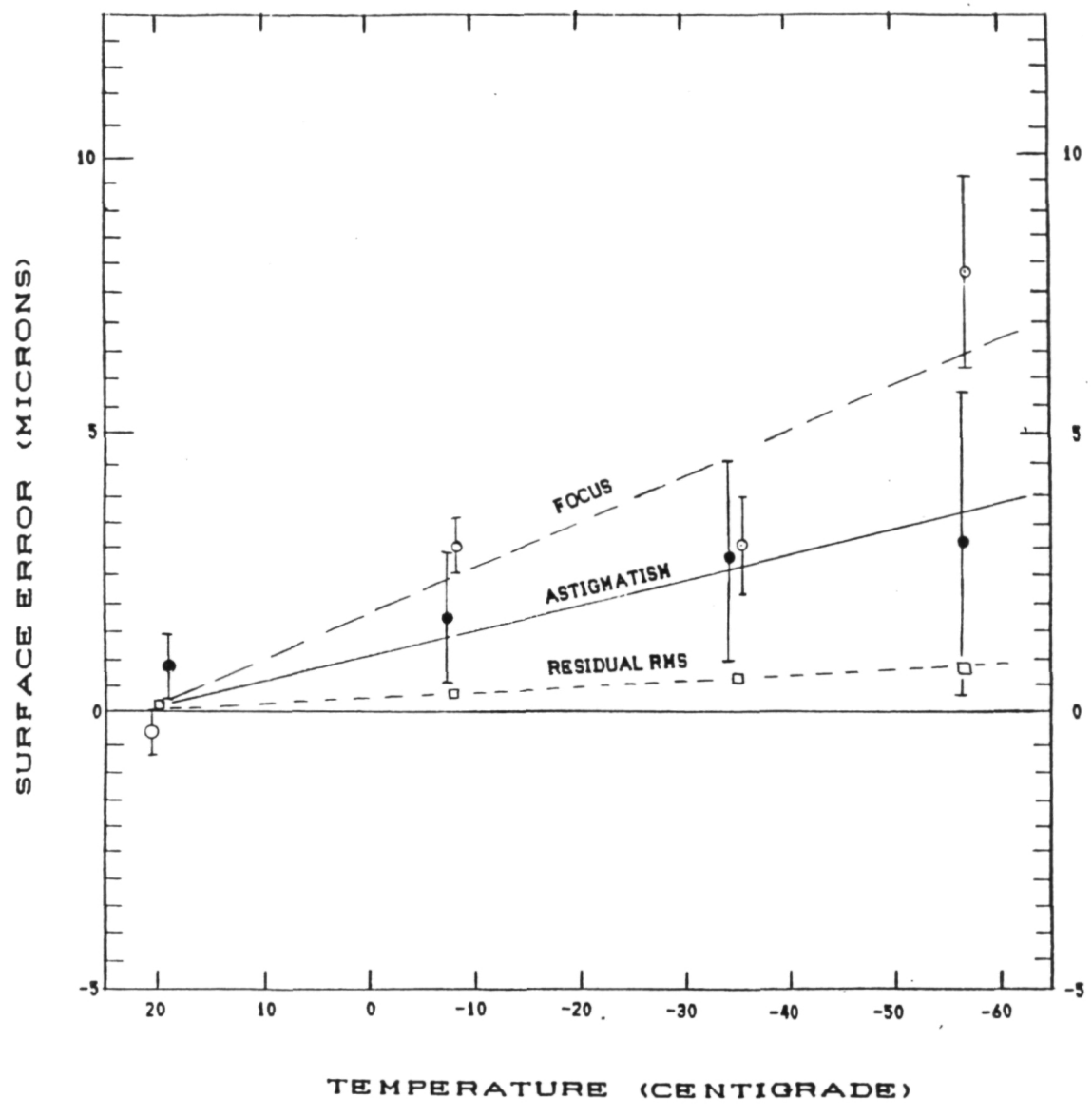

Figure 3.4-7. JPL #1 Mirror Figure Change with Temperature

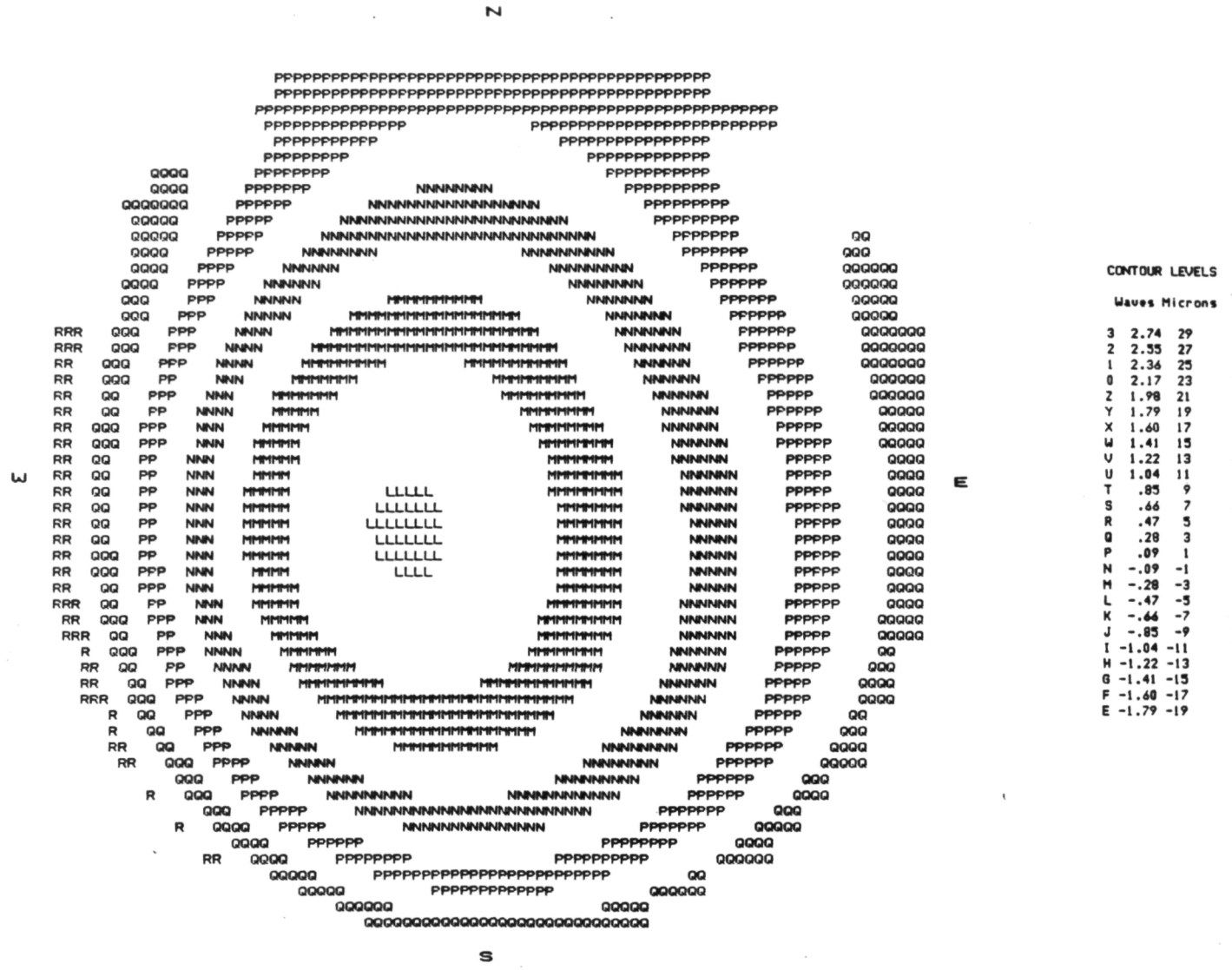

Figure 3.4-8. JPL #1 Mirror Figure at -56.2°C Relative to 21.3°C

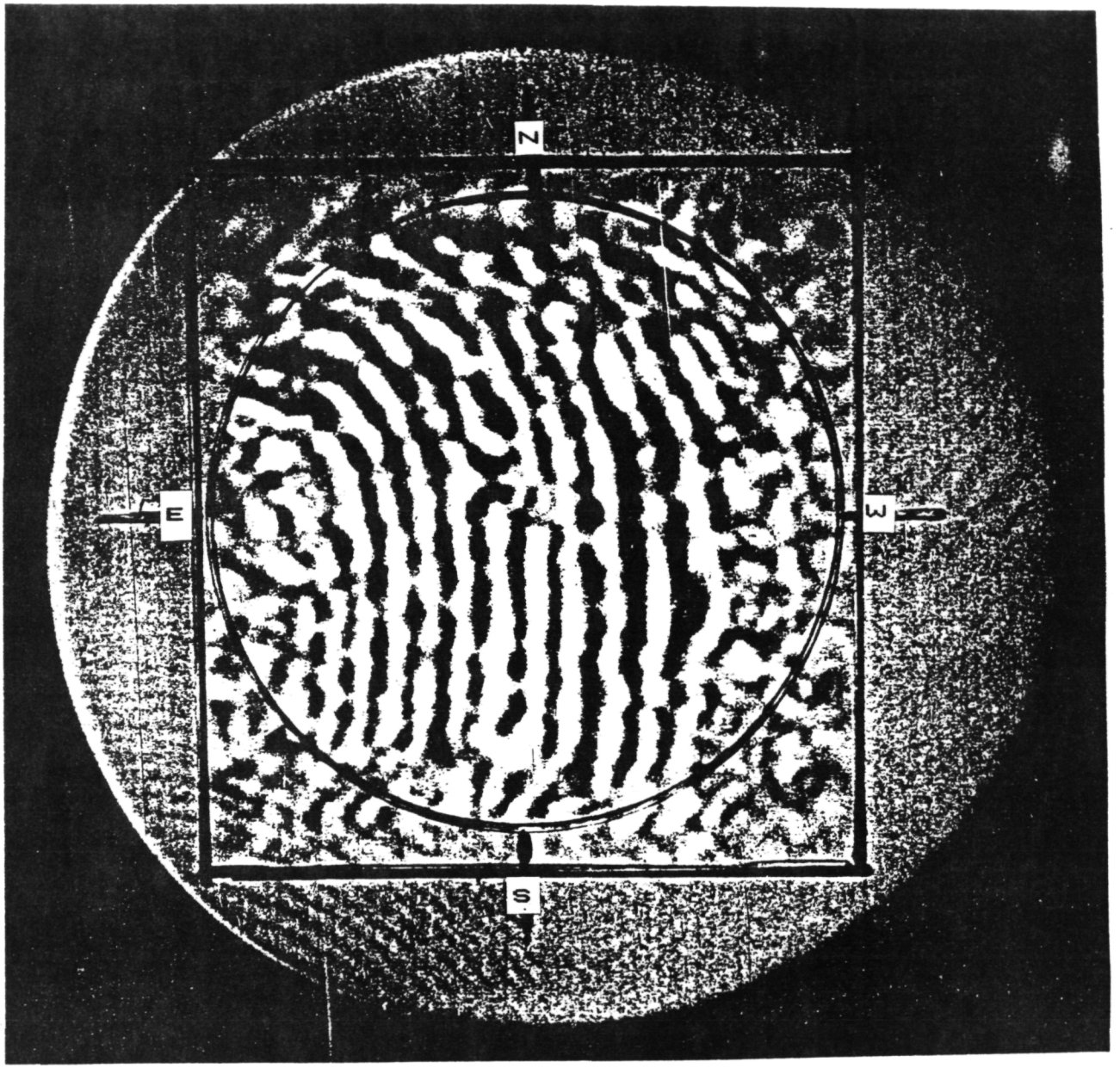

Figure 3.4-9. Interferogram of Mirror JPL #1 at -34.5°C

temperatures.

2) The large-scale distortion of this panel, although not accurately determined, is clearly much less than that of Quad 21. The astigmatism appears to be about one-sixth as large.
3) There is very little hysteresis. The panel returns very closely to its original figure at room temperature.

Conclusion from thermal test of JPL #1: The panel Dornier JPL #1, although of poorer replication quality, represents a large (factor of six) improvement over Quad 21 in large-scale deformation. If another such factor were possible, these panels would be adequately stable against large-scale thermal distortions.

3.5 Low Temperature Performance of Pyrex Facesheet/CFRP Panel Mirror.

As a by-product of the development of precision replicated carbon-fiber-reinforced plastic sandwich panels for the Sub-Millimeter Telescope of the University of Arizona and the Max-Planck Institute for Radioastronomie in Bonn, West Germany, a small test mirror with Pyrex facesheets added to the CFRP sandwich panel was constructed. The purpose of this experiment was to attempt to combine the very lightweight properties of the CFRP sandwich panel with the ease of optically figuring a glass surface.

The mirror is shown in Figure 3.5-1. It has an overall diameter of 30 cm and thickness of 8.6 cm. It is composed of an aluminum honeycomb core 6-cm thick with carbon-fiber-reinforced epoxy facesheets each 1.3-mm thick. An additional aluminum honeycomb sheet 8-mm thick supporting 3-mm thick glass front and back plates are bonded to the CFRP sandwich substrate. The resulting mirror weighs 1.9 kg.

The experiment was successful in that the facesheets were successfully ground and polished to a flat surface and a spherical surface to within one or two waves (optical) using standard optical techniques. To further evaluate the usefulness of this approach, we have tested the figure stability of the mirror over a temperature range from room temperature to -60°C. We have utilized the test chamber and 10.6-μm interferometer described in Section 3.3.

Tests of the Pyrex composite panel were carried out on November 1, 1984. Two interferograms were utilized at each of six temperatures: 21.8°C, .7°C, -22.7°C, -40.1°C, -63.5°C, and 21.1°C. The interferograms were analyzed utilizing the Optical Sciences Center program FRINGE. Only the first fifteen terms of the Zernike polynomial coefficients were used in the analysis. Since we are primarily interested in the figure changes with temperature, we have used the first room temperature measurement as a baseline, subtracting this surface shape from those of the remaining observations. The second room temperature measurement provides an indication of the consistency of the measurements and the potential hysteresis.

The results are shown in Table 3.5-1 and Figures 3.5-2 through 3.5-4. Figure 3.5-4 shows an interferogram taken at -40.1°C. The interferogram has an east-west reversal relative to the panel.

Table 3.5-1 gives the focus change (depth of the spherical distortion of the mirror surface), astigmatism (peak-to-peak range of the saddle-shaped distortion), spherical aberration (peak-to-peak), value of the radial ripple in the surface with center and edge high and an intermediate radius low, and the rms surface change including these terms as well as the higher order Zernike terms in the analysis.

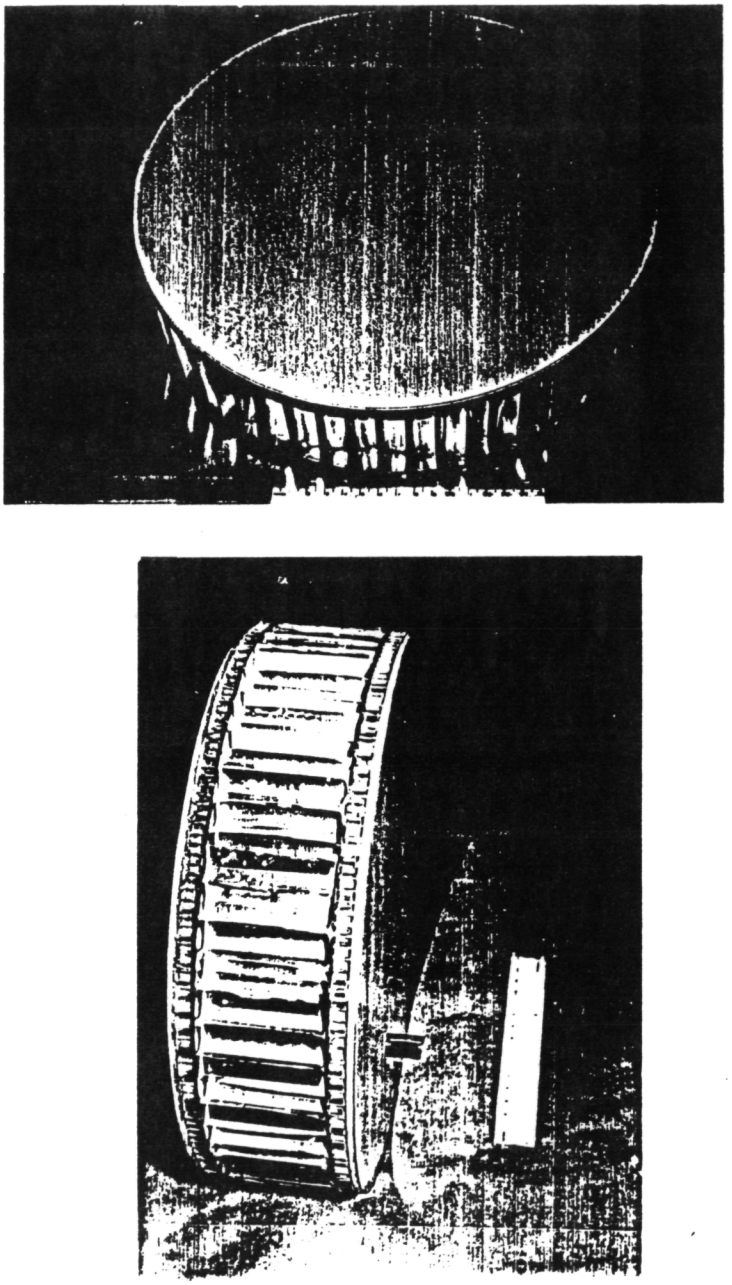

Figure 3.5-1. 30-cm-Diameter Mirror Formed from a CFRP Sandwich Panel with 3-m-Thick Pyrex Front and Back Plates

Table 3.5-1. CFRP/Pyrex Mirror Figure Changes

Temperature (°C)	0.7	-22.7	-40.1	-63.5	21.1
Focus (μm)	3.2±1.3	3.5±0.9	1.9±1.1	0.7±2.4	2.5±1.2
Astigmatism (μm)	5.0±4.7	2.3±4.5	2.7±4.0	5.3±5.0	2.4±5.6
Spherical	3.0±0.7	4.4±0.3	6.4±0.6	5.5±0.2	0.6±0.3
RMS Figure Change	1.8	2.3	2.5	3.4	1.0

The focus, spherical aberration, and rms surface change are plotted in Figure 3.5-2. The spherical aberration is the largest and most systematic of the distortions. It increases more or less linearly to -40°C, then decreases to -63°C. The focus exhibits a rather abrupt change, then decreases toward the low temperatures with a second room temperature value considerably different from the first.

From these results we can see that:

1. Unlike the CFRP sandwich panels that distorted primarily with the lowest order distortions of focus and to a lesser extent astigmatism, the Pyrex facesheet mirror dominantly distorts with spherical aberration indicating a more complex internal stress in the panel.

2. The erratic variation of the distortion coefficients with temperature and the failure for them to return to zero for the second room temperature measurement suggests permanent changes in the Pyrex facesheet panel perhaps due to stress relieving fractures in the bonding.

Conclusion for CFRP/Pyrex mirror: When undergoing temperature change this Pyrex facesheet CFRP lightweight mirror exhibits substantial distortion of higher order than curvature (focus) and astigmatism. In addition, it appears to suffer from hysteresis and permanent change. While the surface can indeed be polished very accurately by optical techniques, it appears that for this particular construction approach, the figure is not adequately stable under temperature change.

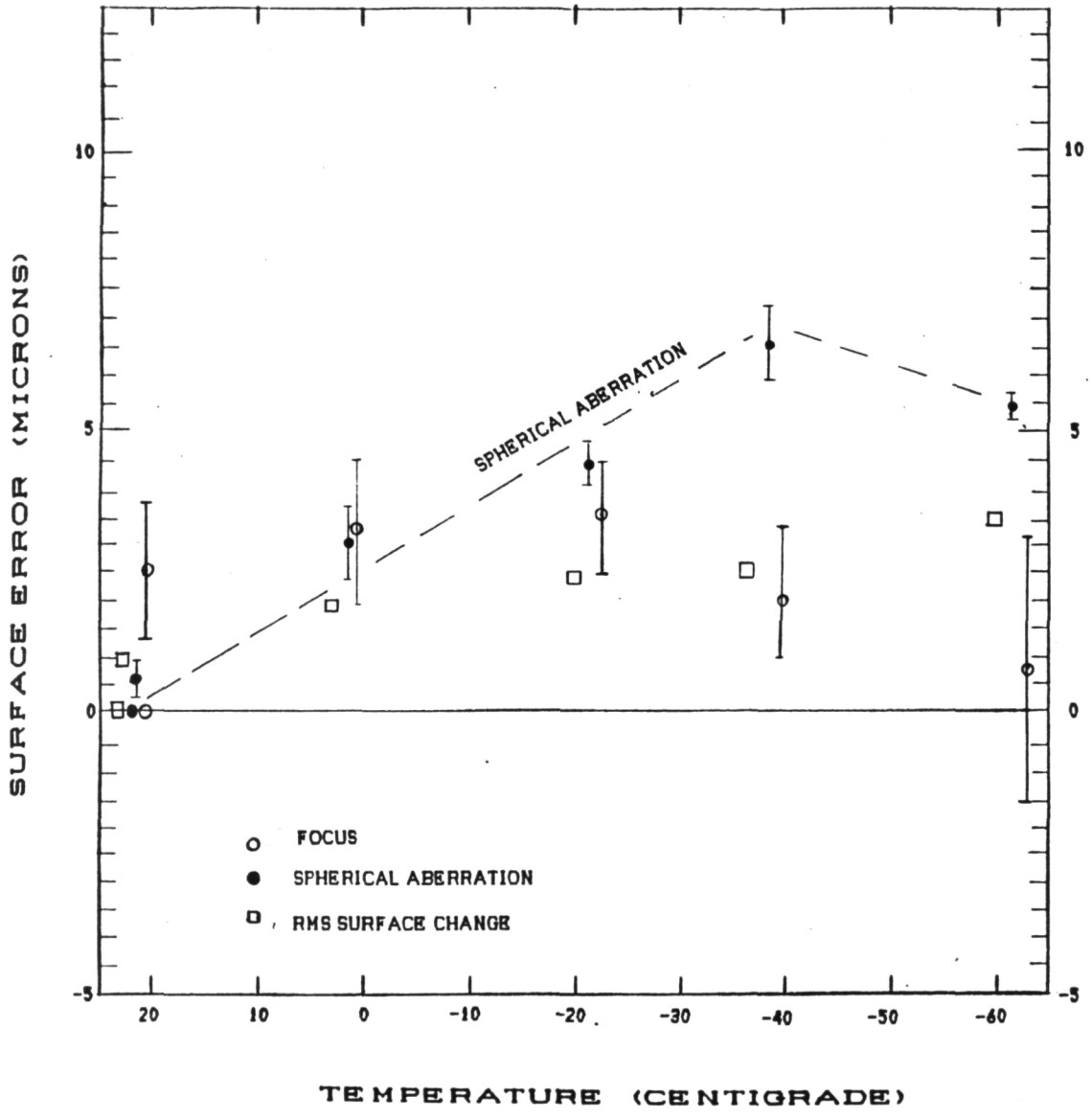

Figure 3.5-2. CFRP/Pyrex Mirror Figure Change with Temperature

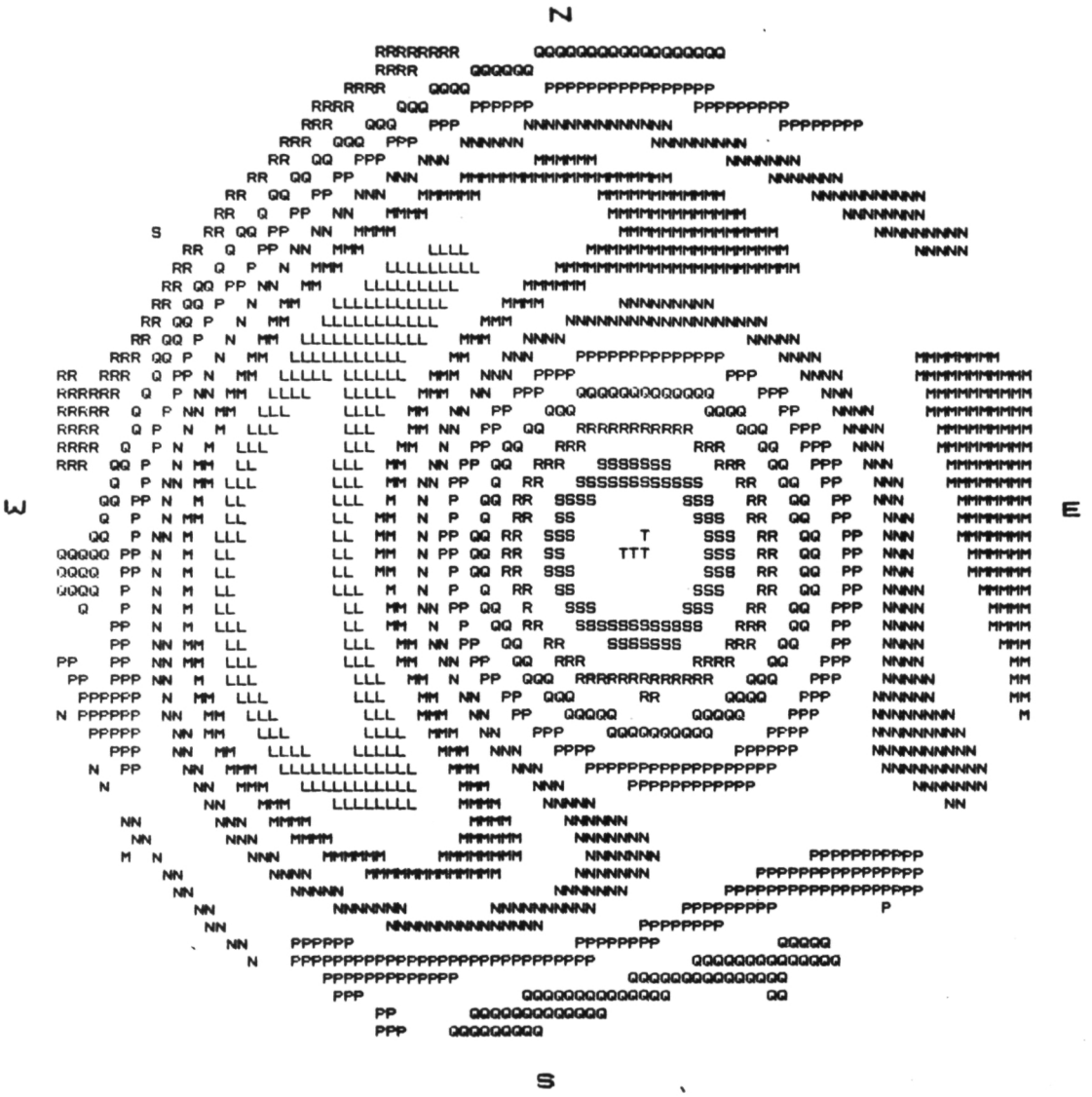

CONTOUR LEVELS

	Waves	Microns
3	2.9	30.7
2	2.7	28.6
1	2.5	26.5
0	2.3	24.4
Z	2.1	22.3
Y	1.9	20.1
X	1.7	18.0
W	1.5	15.9
V	1.3	13.8
U	1.1	11.7
T	.9	9.5
S	.7	7.4
R	.5	5.3
Q	.3	3.2
P	.1	1.1
N	-.1	-1.1
M	-.3	-3.2
L	-.5	-5.3
K	-.7	-7.4
J	-.9	-9.5
I	-1.1	-11.7
H	-1.3	-13.8

Figure 3.5-3. CFRP/Pyrex Mirror Figure at −63.5°C Relative to 21.8°C

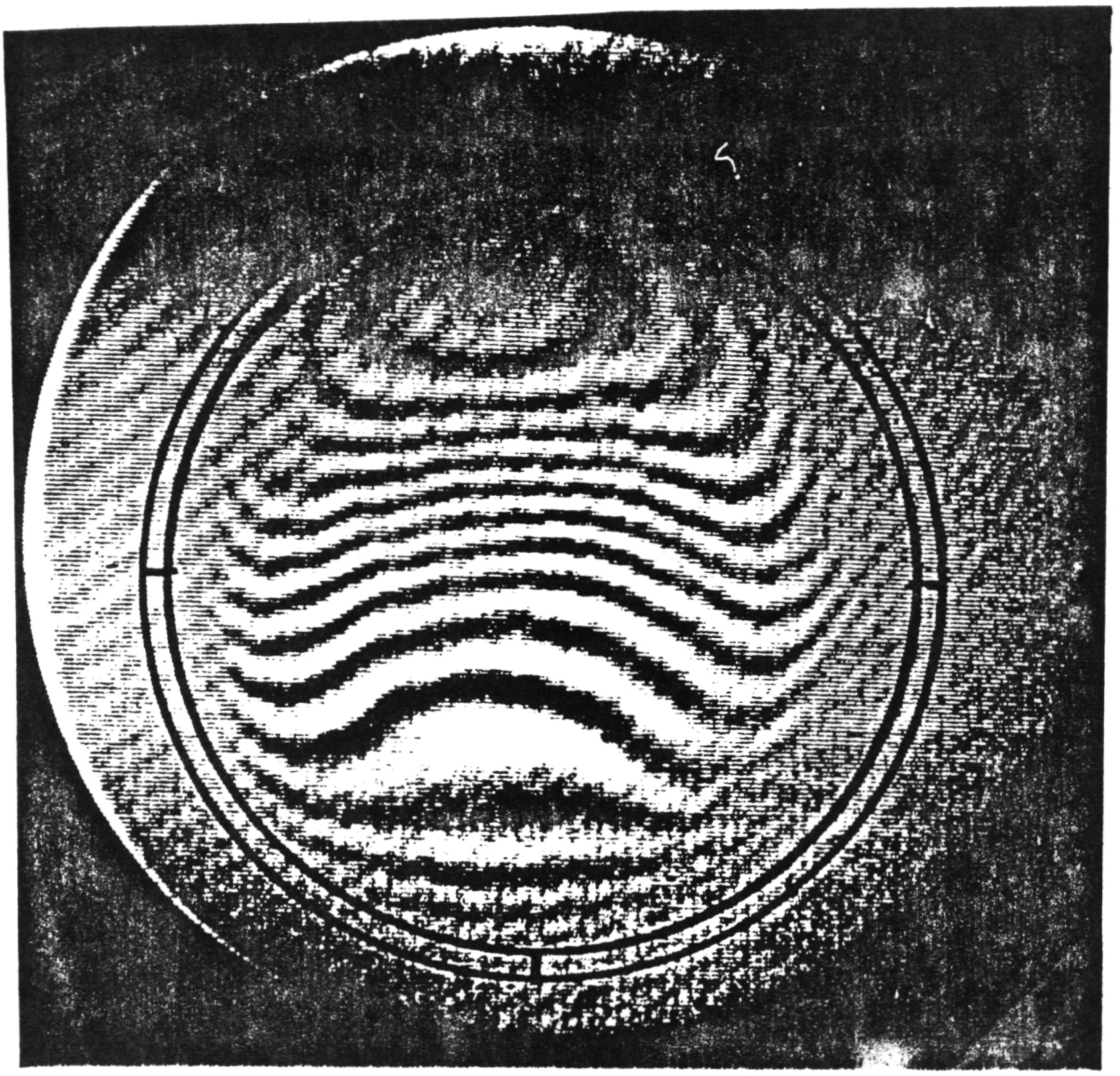

Figure 3.5-4. Interferogram of CFRP/Pyrex Mirror at -40.1°C

3.6 Status of "Lightweighted" Glass Mirror Technology

The development of lightweight welded borosilicate mirror blanks is being carried out at Steward Observatory with partial NASA support. The approach is to use low-melting-point glasses which can be melted in an electrically heated oven and which maintain viscosity when soft to permit welding without collapse of the structure. This approach permits assembling large, lightweight mirrors at a relatively low cost. The lightweight glass provides an option for the balloon telescope that can with certainty meet the figure and figure stability requirements. It is considered to be a backup option relative to composites because of the greater weight (20 to 30 kg/m^2) and greater fragility.

Two products of this development are shown in Figure 3.6-1 and Figure 3.6-2. The mirror in Figure 3.6-1 is made of borosilicate glass (thermal expansion coefficient $3 \times 10^{-6}/°C$) and has diameter 38 cm, overall thickness 11 cm, and density 53 kg/m^2. It is fabricated from 1.3-cm thick front and back plates and a core of 7.5-cm diameter 2.4-mm wall thickness tubes. The tubes are deformed into a fully fused hexagonal structure by applying air pressure to a manifold attached to holes in the back plate while the glass is soft. This mirror was slumped, the faceplates ground to 6 mm thickness and figured as an f/3 sphere to an accuracy of $\lambda/20$ (6328Å) rms. It has been tested at 77°K in the Ames Research Center mirror test chamber and found to depart from a sphere when cooled to $\lambda/10$ rms.

The mirror in Figure 3.6-2 is made from Vycor, a 96% silica glass made by Corning which has a thermal expansion coefficient of $8 \times 10^{-7}/°C$. It has a diameter of 15 cm, overall thickness of 5 cm and density of 32.4 kg/m^2. It is fabricated from .5-cm thick front and back plates and a core of 4.5-cm diameter 2.4-mm wall thickness tubes. This mirror proves the possibility of fabricating welded lightweight mirrors from a material of considerably lower thermal expansion coefficient than borosilicate glass (Pyrex).

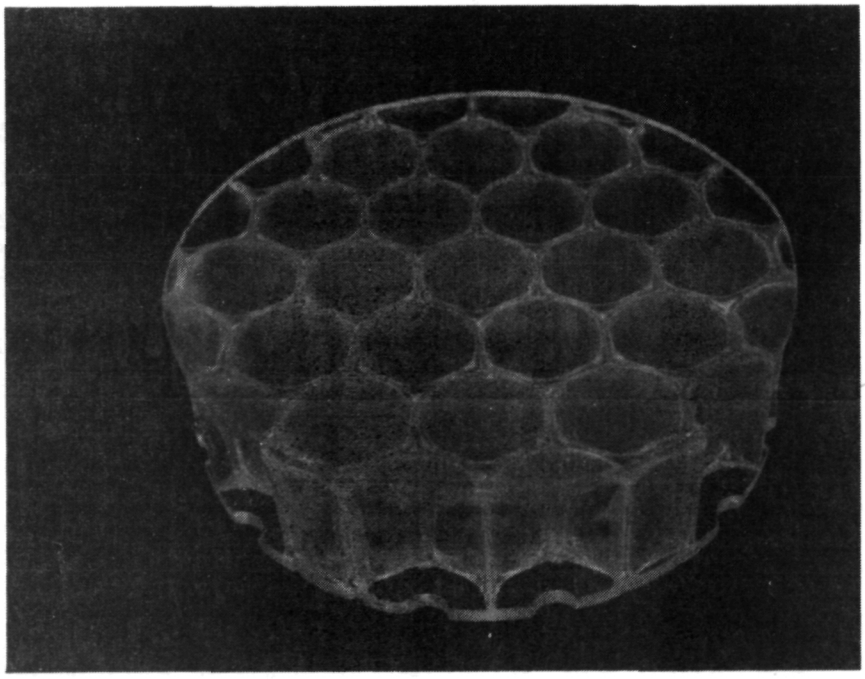

Figure 3.6-1. Welded Borosilicate Glass Mirror 38-cm Diameter.

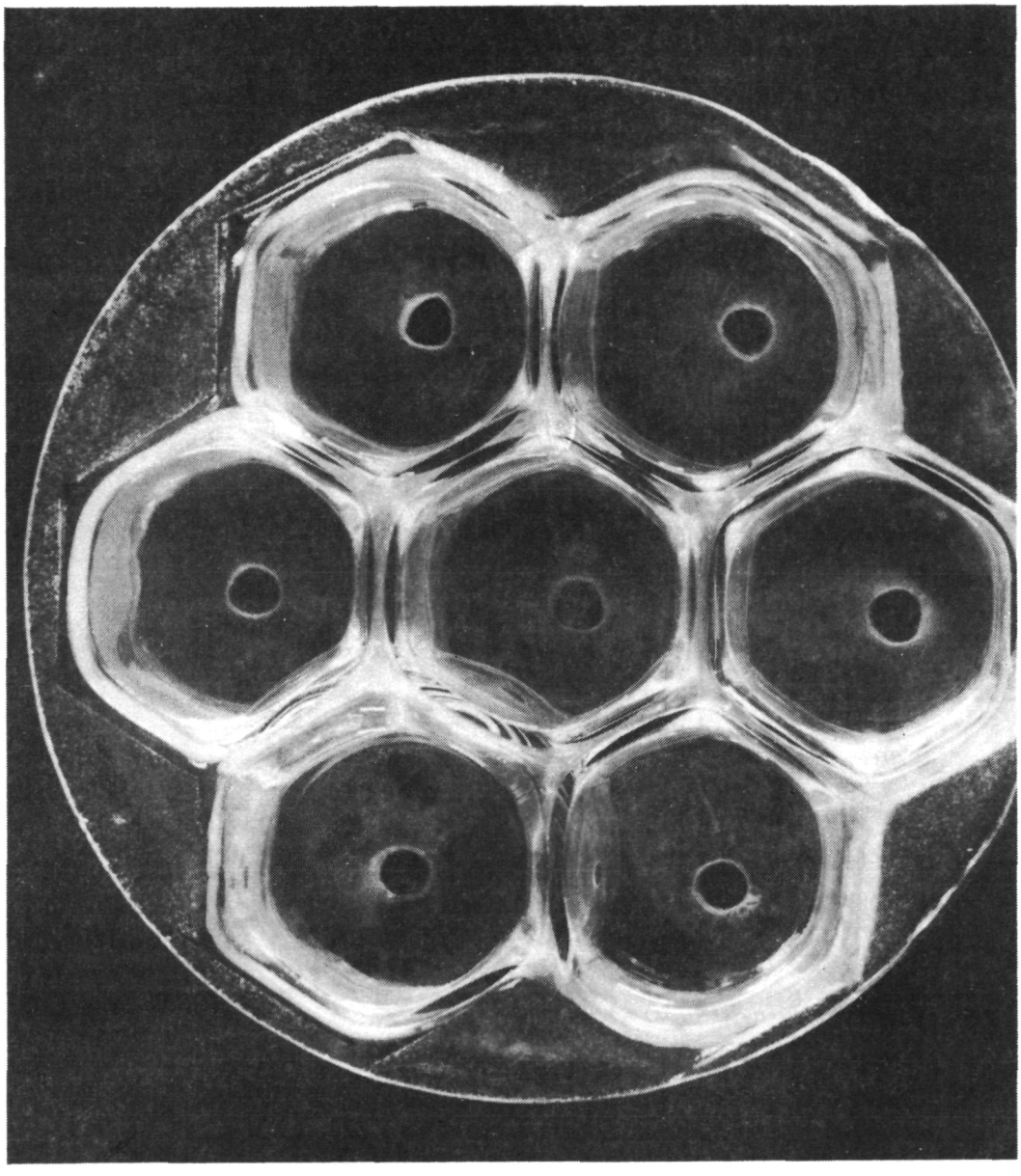

Figure 3.6-2. Welded Vycor Glass Mirror 15-cm Diameter.

3.7 Foamed Aluminum Core Energy Resources Group Mirror

We are procuring and testing a lightweight aluminum mirror using as a core material "Duocel" aluminum foam made by Energy Resources Group, Inc. (ERG). This mirror will be fabricated by dip-brazing aluminum facesheets to the foamed aluminum core forming a lightweight homogeneous aluminum structure. The choice of the aluminum Alloy 5083 or 5086 should provide good stability with aging and temperature cycling and a surface which can be directly figured. The test mirror will be 0.5 meters in size and have an areal density of approximately 20 kg/m^2.

In a preliminary design study in support of this procurement, we accomplished two major tasks: a) we verified that ERG's data for shear modulus (for 6% core density) is correct for very small deflections; b) we constructed a finite-element structural model of a sandwich-construction 3-meter-diameter mirror, and investigated effects of support spacing, core density and facesheet thickness on mirror deflection under gravity load.

Deflection of a sandwich panel under load has bending and shear components. Shear is expected to be a major contributor, and knowledge of the shear modulus is essential. ERG supplied shear modulus data for 6, 8 and 10% density material, but verifying that the data was valid for very small deflections was needed. We obtained three samples of sandwich panels with 6%-density core from ERG, and tested them as center-loaded simply supported beams. Because the bending component depends on known facesheet properties and measured dimensions, we could calculate G_c directly from the experimental load and deflection. A further verification was provided by using different lengths, which changes the ratio of bending and shear and allows them to be separated.

Tests on two of the three samples confirmed (within 20%) ERG's shear modulus data for 6% density. One sample yielded results that were a factor of 4 lower in modulus; this sample was only one inch wide, and upon ERG's suggestion that edge effects could be significant, we ignored this data. Lacking samples of other densities, we assumed the ERG data to be valid for 8% and 10% density as well, and extrapolated that data to 4% and 12% density.

To investigate performance under gravity loading we constructed a finite-element computer model of a 120-inch-diameter (~3 meter) sandwich. We used a flat-panel model; concavity of an actual mirror was not modeled. Various facesheet and core thicknesses were used, holding constant the mass per unit area at 4.1 lb/ft^2 (20 kg/m^2). Beginning with three support points, a case which evidenced deflections of order 100 μm, we increased the number of supports in steps to nine, fifteen, and finally nineteen (one at the center, six at 20-inch radius, and twelve at 45-inch radius). At this support spacing of 20-25 inches the deflections were of order 2-5 μm. Facesheets of 0.025, 0.05 and 0.075 inches thickness, and shear moduli representing densities of 4-12% were used (although not with all combinations).

Results showed that decreasing facesheet thickness (and therefore increasing core thickness, at constant area density) reduced deflection.

Increasing core density also decreased deflection in spite of decreasing core thickness, probably because shear modulus increases as roughly the second power of density. (This implies that shear dominates at the support spacing chosen, because the bending component would increase as roughly the inverse square of sandwich thickness. This is confirmed by increased deflection with increasing core density at the unsupported outer diameter.) There is evidence of a deflection minimum in the vicinity of 10-12% density with 0.025-inch facesheets, although this was not confirmed further. Maximum deflection change between grid points in the model implies slope changes of order 10-20 microradians. These should be viewed with some caution because of the coarseness of the model (roughly 3-6 inches between grid points). Differences among results for 0.025- and 0.050-inch facesheets and 10-12% density cores were not large, and in this range selection of parameters for a sample mirror should be based on other criteria such as ease of fabrication.

4.0 EXPERIMENT ACCOMMODATIONS

4.1 Photometric Camera Description

The baseline focal-plane instrument is a 64-channel photometer/camera similar in overall concept to a 32-channel system which has recently been flown on the KAO. The detector will be an 8 x 8 array of ^{3}He-cooled silicon bolometers, each having individual light concentrating optics. The system will include three interchangeable sets of re-imaging optics (each consisting of a field-lens/pupil-lens pair) which can be used to vary the telescope image scale; pixel sizes will be 4", 8", or 16", corresponding to diffraction-limited fields of view (FWHM $\sim$ 1.2 λ/D) for wavelengths of 50, 100, and 200 μm, respectively. Transmission filters mounted on a cooled filter wheel will provide bandpasses of $0.1 < \Delta\lambda/\lambda < 0.5$ covering the range 38-300 μm.

Signals from individual detectors will be conditioned with N_2-cooled JFET's, amplified, filtered, digitized, and then synchronously demodulated in an on-board microcomputer. Data "frames" consisting of one or several chopper cycles will be transmitted to the ground at a rate of 1-5 frames per second, providing real-time imagery of an 8 x 8 pixel field of 32" x 32", 64" x 64", or 128" x 128", depending on the optics selected. Signal-processing electronics at the ground station will be able to synthesize larger and/or higher signal-to-noise images by co-adding, interpolating, and smoothing sequences of data frames.

The far-infrared camera/photometer will be the principal experiment during the first flights of the telescope and will be available as a backup and infrared focal-plane monitor on subsequent flights with other types of instruments. The total weight of the camera plus electronics should be $\lesssim$ 50 kg and power consumption should be $\lesssim$ 100 W.

4.2 Candidate Experiment Compatibility

We conducted an informal survey of possible candidate instruments by contacting groups with existing instruments (e.g., instruments flown on the KAO or the SAO One-Meter Balloon Infrared Telescope) or groups who have made studies for possible space experiments (e.g., the JPL "Orion" study of submillimeter experiments for a "Spartan" payload). We focused primarily on data rates, volume, weight, and power requirements and did not attempt to assess the readiness or suitability of various types of experiments for remote operation in the balloon environment. Types of instruments considered included photometers, cameras, grating spectrometers with resolution up to 10^4, Fabry-Perot spectrometers, and heterodyne systems using a variety of receivers and local oscillators. The responses we received suggest that the proposed gondola and telescope design would not exclude flying any of those classes of devices. Also, the baseline optical configuration appears to be a workable compromise that could accommodate most potential users.

5.0 GROUND SUPPORT EQUIPMENT REQUIREMENTS

The Three-Meter Balloon-Borne Telescope gondola is a complex and versatile experiment and requires certain specialized equipment throughout the program to support assembly, development testing, subsystem testing and finally full flight level system testing including experiment testing and calibration. This section identifies, in general terms, the GSE required to support these assembly and test activities.

5.1 Optical GSE

Primary and secondary mirror handling, transport and alignment fixtures will be required. These will be supplied by the mirror contractor. Once assembled, the telescope will require the following specialized equipment for shipping and its alignment and installation into the gondola:

- o Shipping container
- o Telescope optical alignment fixture
- o Star tracker and aspect TV co-alignment fixtures
- o Alignment telescope with accessories
- o Laser alignment system
- o Miscellaneous optical accessories (mirrors, beamsplitters, corner cubes, etc.)
- o Automatic auto-collimator for stability testing

Experiment optical alignment and calibration with the telescope will require the following optical/mechanical GSE:

- o Light sources
- o IR sources
- o Experiment FOV beam mapping device
- o Experiment installation/handling fixture

NOTE: The telescope alignment fixtures can also serve to optically align experiments.

5.2 Mechanical GSE

Mechanical GSE is required for assembly, handling, and recovery of the gondola. Gondola assembly will employ several fixtures for handling such large components as the telescope, structural members, crash rings and experiments. Gondola assembly and test will also require portable staging for access to the telescope and both servo-driven gimbal axes.

Handling fixtures are required for positioning and/or transporting major assemblies to facilitate independent testing or repair. The gondola, for example, will require a large base frame with soft (balloon tires) wheels to maintain it in an upright position when not attached to the crane.

Recovery will require several shipping containers for critical items, such as: Experiments, star tracker, aspect TV's, secondary mirror assembly, servo components, etc. Also a standard, 36-foot flat-bed trailer with air suspension and crane is desirable. This will facilitate gondola disassembly and placement on the trailer for transport back to the NSBF.

5.3 Electrical GSE

The Three-Meter Balloon-Borne Telescope program will have an independent, self-contained telemetry ground station except for the use of the NSBF receiver, discriminators, and directional antennas. Being independent of the NSBF ground station as much as possible permits economical full-time use of the equipment for testing and flight preparation. A permanent facility that doesn't have to be moved in and out of the NSBF control room, or respond to the needs of other payloads, is needed to support the proposed schedule of flights. Only a coax connection is needed to receive the PCM data. The PCM data is patched out to several areas in the setup bay. The serial PCM data is decoded by a D-Pad 3 PCM decommutator and sent to a central minicomputer (e.g., a VAX 11/750) that will provide real-time output of the scientific data and housekeeping information, on strip charts, video consoles, and a printer. We assume NSBF will continue to be responsible for recording the data on digital and analog tapes. The minicomputer will also be used to send commands, and provide star field information for the graphics overlay system. The graphics controller mixes the incoming video signal with a graphics overlay generated by the computer and displays the result on a monitor. This is very helpful in rapid identification of the desired area of the sky. Both the acquisition and focal-plane television information will be displayed and recorded on tape.

A block diagram of the ground support equipment and facilities is illustrated in Figure 5.3-1.

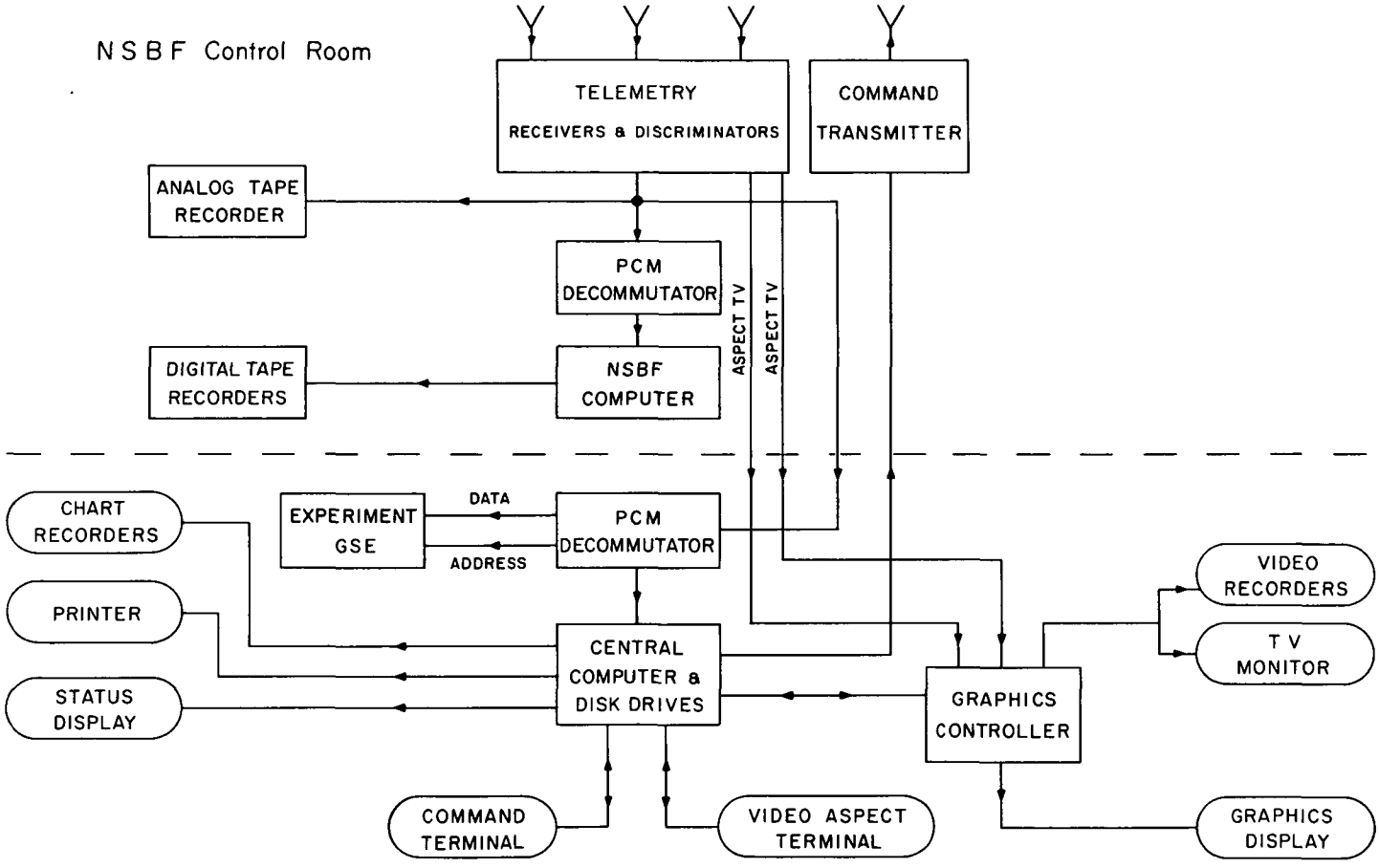

Figure 5.3-1. Gondola Electrical Ground Support Equipment

6.0 NSBF DESIGN DRIVERS AND PAYLOAD SUPPORT REQUIREMENTS

6.1 Payload Support Requirements

Figure 6.1-1 shows the telescope supported within the NSBF high bay experiment staging building.

The NSBF high bay experiment staging building is ideally suited for this program. It has a 3-ton traveling crane with a lift height of 30 ft. and experiment exit doors 27 ft. in height by 14.5 ft. in width. This combination allows gondola suspension for pointing and stabilization testing with access to evening skies and/or within the bay area. The bay's 24-ft. width is more than adequate and if about half the bay's length (30 ft.) is available then this floor area (720 sq. ft.) is adequate for this testing of all operations planned at NSBF. All other staging area facilities are adequate such as lights, power, heat, air conditioning, office space, and so forth.

The gondola also has been designed to operate within the existing NSBF command and telemetry system limitations. This system is adequate for our projected needs at its present 81-kilobit data rate; however, the planned expansion to a 256-kilobit data rate is highly desirable to accommodate efficiently the high bit rates associated with the larger IR imaging arrays now under development (see Section 2.6.1).

Space must also be provided within the high bay building for staging and use of the optical, mechanical and electrical GSE associated with these missions. GSE requirements are identified in Section 5.0.

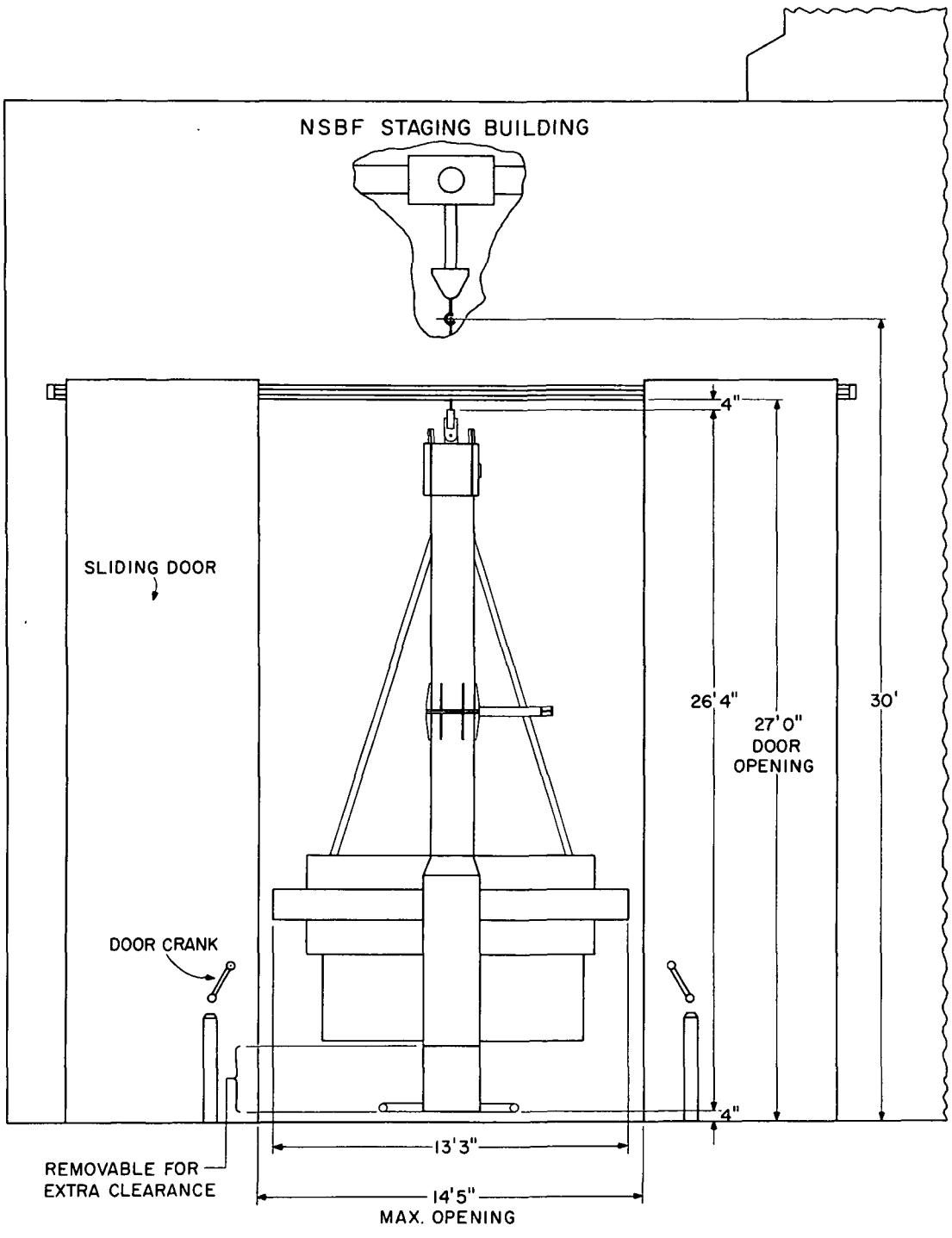

Figure 6.1-1. Gondola Supported Within the NSBF High Bay Experiment Staging Building.

6.2 Launch Requirements

This experiment requires no special and/or different launch requirements than presently employed by the NSBF. The experiment is shown suspended from the launch vehicle in Figure 2.3-1. It requires a suspension height of 34 ft. which is located 11 ft. ahead of the vehicle. This position is easily achievable because of our light weight. All launch vehicle radial clearances with the launch arms are as requested by the NSBF.

Launch requirements relative to science aspects will be similar to those associated with our present One-Meter Balloon Infrared Telescope program. These have been mentioned previously and are summarized below:

Flight Altitude:	28-30 km
Flight Duration:	6-10 hours at altitude
Launch Time:	Local sunset ± 1 hour
Termination Time:	After sunrise at altitude

NASA is currently accessing the safety issues relating to launching heavyweight experiments from the Palestine, Texas, facility. Our understanding is that experiments weighing less than 3,500-4,000 lbs. (limit not determined) will continue to launch as always. Experiments exceeding this limit may be allowed to reach a weight limit of 5,000 lbs. by waiver. The waiver limits the flight trajectory to a westerly float direction. This translates to a six-month launch year of April through October. The Three-Meter Balloon-Borne Telescope fully assembled is expected to weigh less than the 5,000 pound limit.

6.3 Ascent and Float Environment

The gondola will be subjected to a temperature change of 130°F between launch and float altitude with an expected float temperature minimum of -50°F. These environments are well understood and have been successfully managed in numerous balloon payloads including our own One-Meter Balloon Infrared Telescope.

Thermal design does not represent an area of technical concern or development, although stabilization of the mirror temperature is a new design area, which requires diagnostic measurements and testing.

The gondola must also operate in reduced atmospheric pressure (approximately 10 Torr). Operation of balloon payloads in this pressure range is also well understood and therefore is not an area of concern.

Present far-infrared balloon-borne telescopes operate at altitudes of approximately 30±2 km. This altitude is high enough to be above most (>99%) of the water vapor in the earth's atmosphere, yet not so high that it taxes the size of the balloon required. This reduces cost, handling complexity and risk.

The balloon volume required is calculable once the altitude and the suspended weight are specified. For a suspended gondola weight of 4,800 lbs. and a flight altitude of 29-31 km, a 8.52 million cubic ft. (MCF) balloon is required. This is a "small" balloon by NSBF standards and, therefore, should have the highest probability for a flight success.

In the atmospheric region of interest wind velocity also increases with altitude, limiting the time in which the payload will remain within the telemetry range of the base station. Four months a year the wind velocity at 29-31 km is $\leq$ 30 knots. Telemetry range at this altitude is ~300 miles. Therefore, flights of 8-10 hours can be routinely conducted throughout this period. This takes advantage of the full nighttime portion of a standard day.

The gondola has been designed to operate without performance degradation at vibration levels in the 3-5 g rms range, which is well above the 1-2 g rms expected during ground testing, transportation to the launch pad, launch and ascent.

The number of flights that can occur per year depends primarily on the manpower and funds available. A typical time between flights for a recovered and refurnished payload of this complexity is about three weeks assuming adequate spare parts and minimal damage. During the first year we believe that approximately three flights is a reasonable goal with the new gondola. This number of flights will also permit time for gondola modifications that may be necessary during the early stages. During the operational phase six to eight flights per year would be a reasonable goal.

During long duration flights, the increased flight time produces demands on the gondola and ground operations, including the additional weight of ballast, additional thermal problems resulting from both day and night operations, downrange telemetry stations, remote launch operations, additional battery packs, etc. The initial flights are limited to the night, about eight to ten hours at the float altitude, and launching the balloon from the NSBF base site. The next step would be to increase the flight time to observing one night and daytime (approximately 23 hours), followed by eventual cross-country flights of two to three days. Such cross-country flights have already been performed by the NSBF.

6.4 Termination, Landing and Recovery

The task of recovering, loading and transporting gondolas back from remote areas is difficult at best. This size gondola requires that careful attention be paid to recovery operations to assure a safe and straightforward return of the gondola. Our approach to recovery operations is to design a modular gondola that is readily disassembled into easily handled components which can be carried on a standard flat-bed trailer for transport back to NSBF without concern for special routing and/or the need for local road variances.

The modular design also minimizes the damage usually associated with recovery and will keep recovery time to a minimum. Subsequent reassembly

and damage repair can be undertaken simultaneously, facilitating a smooth refurbishment and preparation for the next flight. Flight termination and ground impact are the gondola structural design drivers.

The NSBF requires that a balloon experiment not experience a structural failure resulting in an article or payload free falling from the suspension train. The structural loads are specified as 10 g's (static) along the suspension axis or 5 g's at 45° about a 360° cone located at the attachment point to the NSBF equipment, whichever is limiting. The proposed Three-Meter Balloon-Borne Telescope design meets all these requirements.

7.0 IMPLEMENTATION PHASE SUMMARY DEVELOPMENT PLAN

7.1 Introduction

A plan for designing, building, and flying the Three-Meter Balloon-Borne IR Telescope has been developed based upon the teaming agreement, the assumption that the telescope subassembly and optics would be built by industry and that the gondola would be built by Smithsonian Astrophysical Observatory (SAO). The resulting cost estimate therefore covers the development and initial flights of the entire payload. No assumptions regarding cost sharing with other organizations are included.

In January 1985 we initiated discussions with the Institute of Space and Astronautical Science (ISAS) in Tokyo, Japan, regarding the possibility of their participation in this program. ISAS has expressed interest in participating, possibly by providing the telescope mirrors and CFRP telescope structure, and are preparing, as this report is written, a glass-coated CFRP mirror panel which they will evaluate and then send to the University of Arizona for corroboration of their test results.

Significant reduction in U.S. costs of this project would result from such Japanese participation.

7.2 Statement of Work

The Smithsonian Astrophysical Observatory and its team members -- the University of Arizona (UA) and the University of Chicago -- will design, build, and operate the Three-Meter Balloon-Borne Telescope in accordance with this program plan and NASA requirements. Three flights are planned during the first year of field operations.

Specifically, the Smithsonian Astrophysical Observatory will:

1. Hold overall responsibility for systems design, fabrication, test and integration including integration of the mirrors, secondary mechanisms and primary mirror cover subassembly with the telescope.

2. Hold overall responsibility for program management.

3. Define instrument and telescope interfaces.

4. Be responsible for configuration management, reliability, and quality assurance.

5. Be responsible for field operations, with the support of the University of Arizona and the University of Chicago, including instrument and telescope integration and test.

6. Be responsible for data acquisition and reduction.

7. Perform scientific data analysis and publication of results.

8. Provide the secondary mechanisms and cover mechanisms to the University of Arizona for telescope integration.

The University of Arizona will:

1. Be responsible for optical design, mirror fabrication and test.

2. Provide the telescope assembly to SAO by means of a subcontract to industry.

3. Perform scientific data analysis and publication of results.

4. Support field operations and test.

The University of Chicago will:

1. Define instrument accommodation requirements.

2. Provide the IR photometer for the first missions.

3. Support field operations and test.

4. Perform scientific data analysis and publication of results.

7.3 Schedule

The Implementation Phase is planned as a four-year program as originally proposed, with the final year devoted to field operations (see Figure 7.3-1). Three flights are planned in that year. Completion of the gondola in three years is an ambitious effort, but the schedule is realistic. It will require a heavy front-end loading of engineering personnel to allow the many design tasks to be carried out in parallel. The present SAO Central Engineering organization is ideally suited for working in this manner because it allows us to transfer people into and out of the program as required; only a core staff of engineers will be retained throughout the program for the purpose of providing continuity to the effort.

BALLOON-BORNE THREE-METER TELESCOPE FOR
FAR-INFRARED AND SUBMILLIMETER ASTRONOMY

FIGURE 7.3-1 PROGRAM SCHEDULE

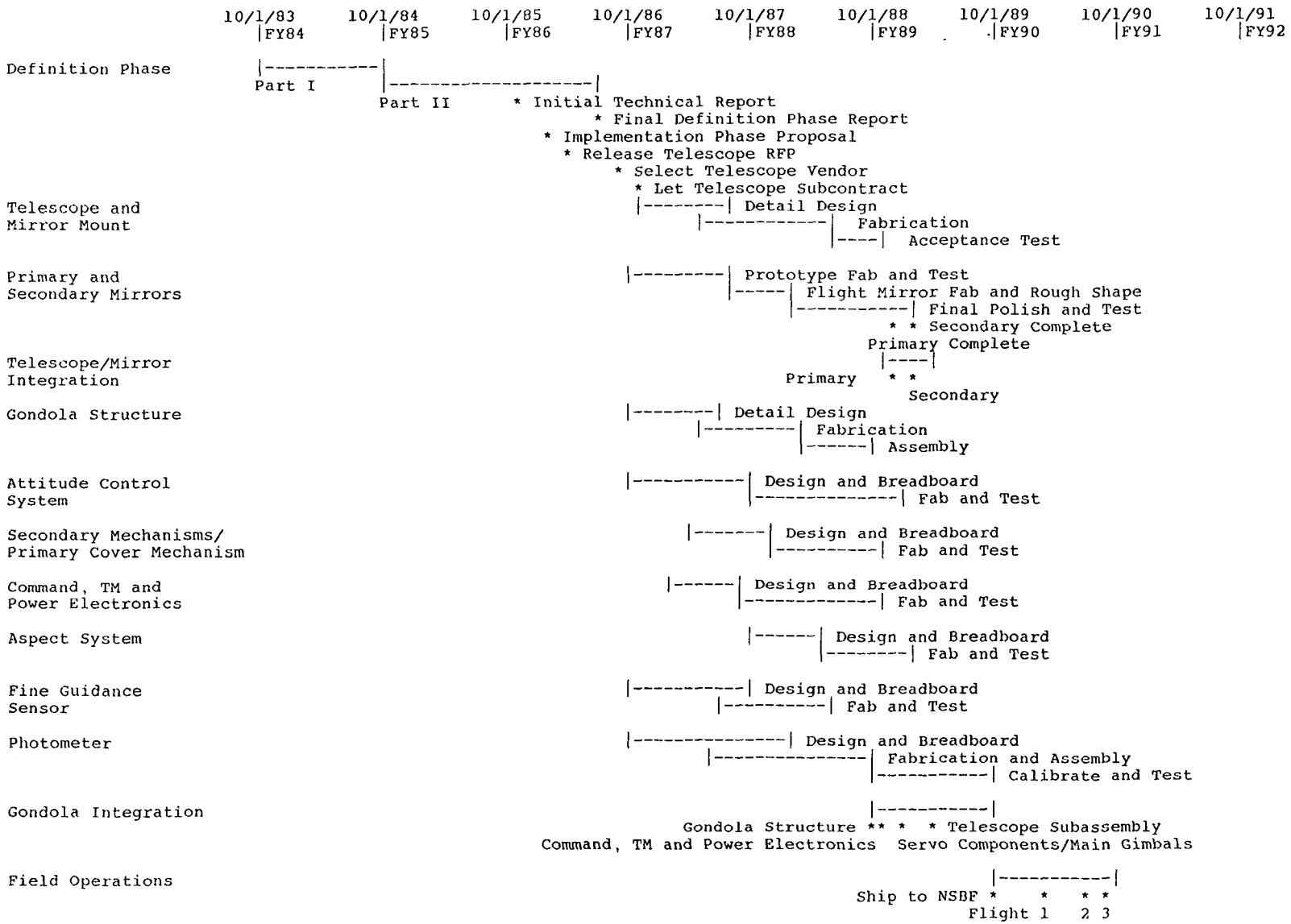

7.4 Implementation Phase Budgetary Cost Estimate

7.4.1 Introduction

For planning purposes we have prepared a budgetary estimate of cost for the Implementation Phase which was developed from the "ground up" as a new estimate in November 1984 and revised in September 1985 to reflect the latest forward projection rates and the salaries currently in effect.

Quotes have been received for most of the largest expenditures.

Dornier GmbH, Friedrichshafen, West Germany, has provided estimates for the primary and secondary mirrors, the telescope structure and telescope GSE; the University of Arizona/Steward Observatory has quoted for the three-meter mirror mold and the University of Arizona/Optical Sciences Center has quoted on the fabrication and optical surface generation of the primary and secondary molds.

Engineering costs and material costs were estimated on a task-by-task basis and combined to develop the total cost estimate.

7.4.2 Status of Cost Estimate

Status of the cost estimate is shown in Table 7.4-1. At the time this estimate was prepared, 79% of the total estimated cost is based on best estimates (task-by-task sum) as quotes from vendors.

Table 7.4-1. Status of Cost Estimate (All Costs Fully Burdened)

Subcontracts			
Telescope		1,769.0K	Quote (Dornier)
Chicago		820.0K	ROM Estimate
Arizona			
Mirror Molds	596.4K		Quote
Mirror Blanks	496.2K		Quote
Optical Design and PGM MGMT	600.0K		ROM Estimate
Mirror Testing	500.0K		ROM Estimate
		2,192.6K	
Engineering		3,495.8K	Best Estimate
Materials and Equipment		1,242.9K	Best Estimate
SAO Science and Management Personnel		849.4K	Best Estimate
Travel		234.2K	ROM Estimate
Other Services		183.8K	ROM Estimate
Other Direct Costs		88.2K	Best Estimate
Total Estimated Cost		10,875.9K	

79% of Total Estimated Cost is based on best estimates or quotes.

Tables 7.4-2 through 7.4-4 present the detailed cost estimate.

One year (FY89) has been allowed for buildup of the gondola and integration of the telescope subassembly. A year has also been allowed for final shaping and polishing of the primary mirror. The gondola structure is scheduled to be complete at the beginning of FY 1989 since it is the base upon which the other components must be assembled. As the various subsystems become available during that year they will be delivered and integrated with the structure. The planned flow is: structure, gondola electronics, main gimbals and other servo components, and the telescope assembly. The telescope, exclusive of the optics, will be delivered directly to SAO from the telescope subcontractor for integration and servo system tests. The primary and secondary optics will go to the UA for optical tests and be integrated with the telescope for final alignment and testing near the end of the overall integration period. Any necessary mirror test fixtures and frames will be defined in consultation with the telescope contractor and the UA and built by SAO.

TABLE 7.4-2. OPTICAL AND INFRARED ASTRONOMY DIVISION
INFRARED ASTRONOMY PROGRAMS
COST PROJECTION

Expense Category and Items	FISCAL YEAR 1986 AND PRIOR TOTALS $	Hours	FISCAL YEAR 1987 TOTALS (PROJECTION) $	Hours	FISCAL YEAR 1988 TOTALS (PROJECTION) $	Hours	FISCAL YEAR 1989 TOTALS (PROJECTION) $	Hours	FISCAL YEAR 1990 TOTALS (PROJECTION) $	Hours	FISCAL YEAR 1991 TOTALS (PROJECTION) $	Hours	THREE-METER BALLOON INFRARED TELESCOPE TOTAL PROGRAM COSTS $	Hours
Personnel Comp.														
	0	0	0	0	0	0	0	0	0	0	0	0	0	0
	0	0	0	0	0	0	0	0	0	0	0	0	0	0
Project Scientist	0	0	29880	1872	31380	1872	32952	1873	34224	1852	0	0	128436	7470
Program Manager	0	0	16728	519	17568	572	18444	519	5376	144	0	0	58116	1755
Secretary	0	0	20196	1872	21204	1871	22260	1871	11688	936	0	0	75348	6550
Mgr/Coordinator	0	0	32532	1872	34152	1872	35520	1872	9336	469	0	0	111540	6085
Programmer	0	0	0	0	0	0	27324	1872	28692	1872	0	0	56016	3744
Data Aide	0	0	0	0	0	0	0	0	0	0	0	0	0	0
	0	0	0	0	0	0	0	0	0	0	0	0	0	0
Ed and Pubs	0	0	1260	80	1323	80	0	0	2778	152	0	0	5361	312
Prior Act/Sub Tot	0	0	0	0	0	0	0	0	0	0	0	0	0	0
WAE Employees	0	0	6330	240	4432	268	0	0	0	0	0	0	10762	508
Total Salaries	$0	0	$106926	6455	$110059	6537	$136500	8007	$92094	5425	$0	0	$445579	26424
Benefits	$0		$53463		$55030		$68079		$46047		$0		$222619	
WAE Ben/Adjust	0		$-2716		$-1901		$0		$0		$0		$-4617	
Travel	0		36000		36000		36000		75000		0		$183000	
Trans. of Things	0		600		600		720		1200		0		$3120	
Property Rental	0		9000		9000		24000		6000		0		$48000	
Equip. Rental*	0		0		0		0		0		0		$0	
Communications	0		3996		4200		4500		4500		0		$17196	
Postage	0		0		0		0		0		0		$0	
Print and Repro	0		537		564		592		1242		0		$2935	
Other Services*	0		78650		21650		21650		21650		0		$143600	
Eng. Services	0		735400		837100		828700		329900		0		$2731100	
Computing-Int.	0		3000		3000		3000		12000		0		$21000	
Computing-Ext.	0		0		0		0		0		0		$0	
Supplies/Mat'ls	0		6000		12000		12000		6000		0		$36000	
Equipment*	0		236040		470760		12000		12000		0		$730800	
Land/Structures	0		0		0		0		0		0		$0	
Total Direct Cost	$0		$1266896		$1558061		$1147741		$607633		$0		$4580332	
Indirect Cost	$0		$354731		$436257		$320416		$170137		$0		$1281542	
Subcontr./Equip. (Cost over $25K)														
Equipment	0		0		307500		0		0		0		$307500	
Dornier	0		559000		1185000		0		0		0		$1744000	
Univ. of Chicago	0		165000		200000		210000		220000		0		$795000	
Univ. of Arizona	0		727585		890000		400000		150000		0		$2167585	
Total Est. Cost	$0		$3073212		$4576818		2078158		$1147770		$0		$10875958	
Cumulative Cost	0		3073212		7650031		9728188		10875958		10875958		$10875958	
Balance	0		-3073212		-7650031		-9728188		********		********		$-10875958	

*First $25,000

TABLE 7.4-3. THREE-METER BALLOON-BORNE INFRARED TELESCOPE
EQUIPMENT, SERVICES AND SUBCONTRACT COST SUMMARY

Mechanical Equipment

Hardware	$6000
Machined Parts	70500
Bearings	11100
Flexpivots	32000
Gimbals	50000
Gimbal Motors	22500
Reaction Wheels (First $25,000)	25000
Mechanical GSE	36000
Stow System	5000
Mechanical Components and Parts	51200
Structure and Telescope Fabrication (First $25,000)	25000
Fixtures	11500
Optical Components	5000
Optical GSE	10000
Miscellaneous	11000
TOTAL	$371800

Electrical Equipment

Wire, Solder and Misc. Supplies	$15200
Racks and Chassis	11500
Fabricated Parts (PC Cards, Cable Assy's. etc.)	24000
DC/DC Converters	3000
Flight Batteries	15000
Connectors	15300
Electronic Components	49500
Electrical Components (Motors, Sensors, Encoders, etc.)	30500
Electrical GSE	33500
Aspect System TV Cameras	20000
Ground Station (Computer, Printer, Tape Drives, etc.)	138500
Power Supplies	3000
TOTAL	$359000

Subcontracts and Equipment over $25,000

Structure and Telescope Support		$102500*
Reaction Wheels		205000*
University of Arizona		
Mirror Mold Blank	596400	
Mirror Mold Generation and Polish	496185	
Optical Design and Program Management	600000	
Mirror Testing	500000	
SUBTOTAL	$2192585	2167585*
University of Chicago		795000*
Dornier (Telescope)		
Development and Prototype	252000	
Engineering	307000	
Fabrication of Mirrors	630000	
Fabrication of Structure	535000	
Handling and Shipping Equipment	45000	
SUBTOTAL	$1769000	1744000*

*Balance over $25,000 TOTAL $5014085

Other Services

University of Arizona (First $25,000)	$25000
University of Chicago (First $25,000)	25000
Dornier (First $25,000)	25000
Computer Maintenance	36000
Software Maintenance	18000
Test Equipment Calibration and Repair	9600
Miscellaneous	5000
TOTAL	$143600

TABLE 7.4-4. THREE-METER BALLOON-BORNE INFRARED TELESCOPE
ENGINEERING COST ESTIMATE

	FY 1987		FY 1988		FY 1989		FY 1990		TOTALS	
	HOURS	$	HOURS	$	HOURS	$	HOURS	$	HOURS	$
Mechanical Engineers	7112	$189.8	7112	$200.7	7112	$210.7	2870	$91.2	24206	692.4
Electrical Engineers	6510	$149.4	5990	$92.7	5658	$87.7	3224	$30.5	21381	360.3
Structural Engineer	520	$11.7	1040	24.5	0	0.0	0	0.0	1560	36.1
Thermal Engineer	520	$15.5	520	16.3	520	17.1	0	0.0	1560	49.0
Mechanical Technicians	0	$0.0	1830	35.4	1830	37.2	1830	39.0	5490	111.6
Electrical Technicians	1560	$18.9	2870	36.5	2870	38.3	1830	25.7	9130	119.4
Mechanical Drafting	1435	$21.9	1830	29.4	1560	26.3	0	0.0	4825	77.6
Electrical Drafting	520	$8.2	1394	23.0	1394	24.2	0	0.0	3308	55.4
Reliability and Quality Assurance	0	$0.0	1040	14.4	1830	26.7	0	0.0	2870	41.1
TOTALS	18177	$415.5	23626	$472.9	22774	$468.2	9754	$186.4	74330	$1543.0
Benefits at 50%		207.7		236.5		234.1		93.2		771.5
Engineering Burden at 18%		112.2		127.7		126.4		50.3		416.6
TOTAL DIRECT ENGINEERING COSTS		$735.4		$837.1		$828.7		$329.9		$2731.1

7.4.3 Cost Estimate Assumptions

The following assumptions were made as a basis for this estimate

- Star tracker and gyro package are assumed to be provided as GFE.
- All shipments are by government bills of lading (GBL's).
- Gondola buildup and test will be done in a rented high bay area at Hanscom Air Force Base, Bedford, MA.
- "WAE" employee is servo system analyst.
- Travel is ROM estimate based on experience with similar programs.
- Effect of potential cost-sharing agreement with ISAS, Tokyo, Japan.
- Engineering salaries are FY87 actuals with 5% average increase per year assumed, full-time employees listed at 88% productivity.

References

Aumann, H.H. 1984, Bull. AAS, **16**, 483.

Aumann, H.H., Gillett, F.C., Beichman, C.A., de Jong, T., Houck, J.R., Low, F.J., Neugebauer, G., Walker, R.G., and Wesselius, P.R. 1984, Ap. J. Lett. **278**, L23.

Gascoigne, S.C.B. 1973, Applied Optics, **12**, 1419.

Harper, D.A., Loewenstein, R.F., and Davidson, J.A. 1984, Ap.J., **285**, 808.

Keene, J., Davidson, J.A., Harper, D.A., Hildebrand, R.H., Jaffe, D.T., Loewenstein, R.F., Low, F.J., and Pernic, R. 1983, Ap. J. Lett., **274**, L43.

Norris, C.H. 1960, Elementary Structural Analysis, (New York: McGraw-Hill), second edition.

Smith, B.A., and Terrile, R.J. 1984, Science, **226**, 1421.

APPENDIX A

Optics Design Tradeoffs

a) Tradeoff Approach

The telescope design is constrained by our desire to provide as large an aperture as possible within the capability of the U.S. Scientific Balloon Launch Facility. This maximum aperture is approximately 3 meters. In addition the overall secondary vertex-to-Cassegrain focus distance is constrained by the launch facilities to approximately 4.9 meters. In the design study we have chosen as the variable parameters the aperture, Cassegrain focal ratio, primary-secondary separation, and primary-to-focal-plane distance. We have considered the required field radius, chopper field amplitude, and maximum operating wavelength to be fixed. The tradeoff studies investigate the impact of varying the input parameters on the focal-plane scale, primary focal ratio, secondary obscuration, chopper-induced and field aberrations, and alignment tolerances. These impacts are examined for five different values of each of the four parameters while the other three are held at the chosen design values. The calculations are based on the third order diffraction theory referred to in Section 2.2.1.

Tables A-1 through A-4 display the results of these calculations. In Table A-1 the aperture is varied from 200 to 400 centimeters. In Table A-2 the Cassegrain focal ratio is varied from f/8.5 to f/18.5. Table A-3 varies this ratio from .2 to .5 while holding the overall distance constant at 490 cm. In the tables the horizontal boxes indicate the varying parameters and the vertical boxes enclose the chosen design. In Table A-4 the overall length from secondary vertex to Cassegrain focal plane is varied from 381 cm to 526 cm while holding the ratio of the primary vertex-Cassegrain focal-plane distance to the primary vertex-secondary vertex distance constant at .4.

The meanings of the items in Tables A-1 through A-4 are as follows*:

---

*Definition/Explanation is given only where it is needed to clarify the item. If the meaning is conventional, or the item has already been defined above, there is no definition. It would burden the text to add definitions which are not needed.

Aperture (cm)	Primary clear diameter.
Cassegrain focal ratio (f/)	
Primary secondary separation (cm)	Distance between primary vertex and secondary vertex.
Primary focal-plane separation (cm)	Distance between primary vertex and Cassegrain focal plane.
Field radius (')	Specified maximum radius of field on the sky in the infrared.
Chop field amplitude (')	Specified maximum amplitude of beam switching on the sky.
Minimum wavelength (microns)	Shortest design wavelength for infrared observations.
Maximum wavelength (microns)	Longest design wavelength for infrared observations.
Diffraction HPFW min (")	1.22λ/D for minimum wavelength where D is the projection of the secondary pupil on the primary.
Diffraction HPFW max (')	1.22λ/D for the maximum wavelength.
Secondary undersize	Fractional undersizing of the secondary diameter relative to the primary to assure that the secondary is the pupil stop of the system. The undersizing is calculated so that for the full infrared field size, the maximum chop amplitude, and the full diffraction width diameter of Airy disk first zero at the maximum wavelength an optical path from the focal plane to the edge of the secondary will intersect the primary surface and not the warm periphery of the primary.
Cassegrain focal length (cm)	
Focal-plane scale ("/mm)	
Primary focal length (cm)	

Primary focal ratio (f/)	
Primary sagitta (cm)	
Primary departure from sphere (cm)	
Primary hole min IR visible (cm)	Minimum size hole in the primary which will not vignette optical paths from the focal plane over the field radius including diffraction to the first Airy disk zero at the maximum wavelength.
Primary hole max (cm)	Maximum size hole in the primary which stays within the shadow of the secondary over the infrared field, chop amplitude, and diffraction to the first Airy disk zero at the maximum wavelength.
Secondary diameter (cm)	
Secondary focal length (cm)	
Secondary conic constant $-e^2$	
Secondary sagitta (cm)	
Secondary departure from sphere (cm)	
Secondary button min (cm)	Diameter of a reflecting button on the secondary required so that no optical ray from the focal plane over the field size, chopper amplitude, and diffraction to the first zero of the Airy disk is returned to the minimum primary hole.
Secondary button max (cm)	Diameter of a reflecting button on the secondary required so that it, rather than the shadow of the secondary, is the central pupil of the system over the infrared field amplitude, chop amplitude, and diffraction to the first zero of the Airy disk.
Secondary axial magnification	Ratio of the change in the location of Cassegrain focus to focussing motion of the secondary.

Secondary angular magnification	Ratio of the angular motion in the sky to the secondary tilt angle.
Range for 1" blur	
Chop (')	Chop amplitude referred to the focal plane at which the coma length is one arcsecond.
Back focus (cm)	Distance from the nominal focus at which the refocussed image blur due to spherical aberration is one arcsecond.
Field coma (')	Field radius at which the coma length is one arcsecond.
Field astigmatism (') (quadratic)	Field radius for which the astigmatism is one arcsecond. The astigmatism blur increases quadratically with field radius.
Field curvature (') (quadratic)	The field radius at which the blur due to field curvature is one arcsecond. The field curvature blur increases quadratically with field radius.
Alignment for 1" blur	
Secondary decenter (mm)	Secondary decenter for which the coma length is one arcsecond.
Secondary tilt (')	Secondary tilt for which the coma length is one arcsecond.
Secondary axial motion (mm)	Secondary axial motion which produces a defocus blur diameter of one arcsecond.
Alignment for 1" motion	
Secondary decenter (mm)	Decenter which produces a one-arcsecond motion on the sky.

Secondary tilt (')	Secondary tilt which produces a one-arcsecond motion in the sky.

Initial alignment

Secondary defocus for 20" blur (mm)	
Secondary decenter for 10" coma (mm)	
Secondary decenter for 1" corrected blur	Maximum secondary decenter for which the coma can be compensated by secondary tilt with a resulting tilt of the focal plane which causes a maximum image blur of one arcsecond at the edge of the field.
Secondary decenter for 2.5' motion (mm)	
Secondary tilt for 2.5' motion (')	
Secondary tilt for 10" coma (')	

Aperture (cm)	200	250	300	350	400
Cassegrain focal ratio (f/)	13.5	13.5	13.5	13.5	13.5
Primary secondary separation (cm)	350	350	350	350	350
Primary focal plane separation (cm)	140	140	140	140	140
Field radius (')	2.5	2.5	2.5	2.5	2.5
Chop field amplitude (')	2.5	2.5	2.5	2.5	2.5
Minimum wave length (microns)	30	30	30	30	30
Maximum wave length (microns)	1000	1000	1000	1000	1000
Diffraction HPFW min (")	3.9267	3.1339	2.6074	2.2324	1.9517
Diffraction HPFW max (')	2.1815	1.7410	1.4486	1.2402	1.0843
Secondary undersize	.03873	.03644	.03491	.03382	.03301
Cassegrain focal length (cm)	2595.4	3252.0	3908.6	4565.2	5221.8
Focal plane scale ("/mm)	7.9470	6.3425	5.2771	4.5181	3.9500
Primary focal length (cm)	431.46	412.09	400.17	392.08	386.24
Primary focal ratio (f/)	2.1573	1.6484	1.3339	1.1202	.96561
Primary sagitta (cm)	5.7943	9.4791	14.057	19.527	25.890
Primary departure from sphere (cm)	.01959	.05515	.12567	.24938	.44905
Primary hole min (cm)	15.420	16.102	16.784	17.466	18.148
Primary hole max (cm)	28.551	27.186	25.822	24.458	23.094
Secondary diameter (cm)	36.296	36.296	36.296	36.296	36.296
Secondary focal length (cm)	-97.70	-71.10	-55.89	-46.04	-39.14
Secondary conic constant (-e^2)	-1.957	-1.665	-1.508	-1.411	-1.345
Secondary sagitta (cm)	.83933	1.1518	1.4634	1.7742	2.0843
Secondary departure from sphere (cm)	.00180	.00463	.00946	.01677	.02703
Secondary button min (cm)	4.8825	3.7988	3.9263	3.6544	3.4510
Secondary button max (cm)	8.3148	6.8416	5.8634	5.1665	4.6449
Secondary axial magnification	-37.19	-63.28	-96.40	-136.6	-183.8
Secondary angular magnification	.37759	.30135	.25073	.21467	.18768
Range for 1" blur					
Chop (')	.85087	.49093	.31966	.22476	.16667
Back focus (cm)	24.990	18.118	14.204	11.678	9.9146
Field coma (')	14.970	15.041	15.089	15.123	15.148
Field astigmatism (') quadratic	18.014	15.865	14.338	13.181	12.266
Field curvature (') quadratic	7.0741	5.4770	4.4708	3.7779	3.2714
Alignment for 1" blur					
Secondary decenter (cm)	-.0534	-.0294	-.0186	-.0128	-.0094
Secondary tilt (')	-2.253	-1.629	-1.275	-1.047	-.8881
Secondary axial motion (cm)	.00439	.00324	.00256	.00211	.00180
Alignment for 1" motion					
Secondary decenter (cm)	-.0025	-.0023	-.0022	-.0021	-.0020
Secondary tilt (')	.04414	.05531	.06647	.07764	.08881
Initial alignment					
Secondary defocus for 20" blur (cm)	.08782	.06482	.05122	.04228	.03597
Secondary decenter for 10" coma (cm)	.53394	.29424	.18605	.12817	.09363
Secondary decenter for 1" corrected blur	1.0984	.64942	.42856	.30386	.22662
Secondary decenter for 2.5' motion (cm)	.37632	.34317	.32420	.31192	.30332
Secondary tilt for 2.5' motion (')	6.6210	8.2960	9.9709	11.646	13.321
Secondary tilt for 10" coma (')	22.534	16.291	12.749	10.470	8.8809

Table A-1. Aperture Tradeoff

Aperture (cm)	300	300	300	300	300
Cassegrain focal ratio (f/)	18.5	16	13.5	11	8.5
Primary secondary separation (cm)	350	350	350	350	350
Primary focal plane separation (cm)	140	140	140	140	140
Field radius (')	2.5	2.5	2.5	2.5	2.5
Chop field amplitude (')	2.5	2.5	2.5	2.5	2.5
Minimum wave length (microns)	30	30	30	30	30
Maximum wave length (microns)	1000	1000	1000	1000	1000
Diffraction HPFW min (")	2.6415	2.6245	2.6074	2.5905	2.5736
Diffraction HPFW max (')	1.4675	1.4580	1.4486	1.4391	1.4298
Secondary undersize	.04737	.04117	.03491	.02859	.02221
Cassegrain focal length (cm)	5287.1	4602.4	3908.6	3205.6	2493.4
Focal plane scale ("/mm)	3.9012	4.4816	5.2771	6.4343	8.2723
Primary focal length (cm)	385.75	391.70	400.17	413.15	435.61
Primary focal ratio (f/)	1.2858	1.3057	1.3339	1.3772	1.4520
Primary sagitta (cm)	14.582	14.360	14.057	13.615	12.913
Primary departure from sphere (cm)	.14048	.13409	.12567	.11406	.09715
Primary hole min (cm)	16.285	16.320	16.784	17.975	20.542
Primary hole max (cm)	12.276	18.273	25.822	35.968	50.985
Secondary diameter (cm)	26.486	30.625	36.296	44.545	57.647
Secondary focal length (cm)	-38.56	-45.58	-55.89	-72.50	-103.7
Secondary conic constant (-e^2)	-1.340	-1.407	-1.508	-1.679	-2.026
Secondary sagitta (cm)	1.1313	1.2786	1.4634	1.6970	1.9826
Secondary departure from sphere (cm)	.00818	.00884	.00946	.00982	.00938
Secondary button min (cm)	3.3353	3.0526	3.9263	4.5678	5.8554
Secondary button max (cm)	3.7717	4.5756	5.8634	8.1202	12.638
Secondary axial magnification	-188.9	-139.1	-96.40	-61.20	-33.76
Secondary angular magnification	.18536	.21293	.25073	.30571	.39304
Range for 1° blur					
Chop (')	.29551	.30529	.31966	.34287	.38662
Back focus (cm)	24.028	18.809	14.204	10.246	6.9852
Field coma (')	27.609	20.920	15.089	10.149	6.1402
Field astigmatism (') quadratic	14.157	14.233	14.338	14.495	14.756
Field curvature (') quadratic	3.7509	4.0614	4.4708	5.0447	5.9324
Alignment for 1° blur					
Secondary decenter (cm)	-.0166	-.0174	-.0186	-.0206	-.0245
Secondary tilt (')	-1.594	-1.434	-1.275	-1.122	-.9837
Secondary axial motion (cm)	.00239	.00246	.00256	.00271	.00298
Alignment for 1° motion					
Secondary decenter (cm)	-.0020	-.0021	-.0022	-.0023	-.0026
Secondary tilt (')	.08992	.07827	.06647	.05452	.04240
Initial alignment					
Secondary defocus for 20° blur (cm)	.04784	.04923	.05122	.05427	.05951
Secondary decenter for 10° coma (cm)	.16579	.17392	.18605	.20603	.24495
Secondary decenter for 1° corrected blur	.29777	.35106	.42856	.55139	.77455
Secondary decenter for 2.5' motion (cm)	.30260	.31135	.32420	.34491	.38384
Secondary tilt for 2.5' motion (')	13.488	11.741	9.9709	8.1777	6.3606
Secondary tilt for 10° coma (')	15.943	14.337	12.749	11.216	9.8366

Table A-2. Cassegrain Focal Ratio Tradeoff

Aperture (cm)	300	300	300	300	300
Cassegrain focal ratio (f/)	13.5	13.5	13.5	13.5	13.5
Primary secondary separation (cm)	330	350	370	390	410
Primary focal plane separation (cm)	160	140	120	100	80
Field radius (')	2.5	2.5	2.5	2.5	2.5
Chop field amplitude (')	2.5	2.5	2.5	2.5	2.5
Minimum wave length (microns)	30	30	30	30	30
Maximum wave length (microns)	1000	1000	1000	1000	1000
Diffraction HPFW min (")	2.6022	2.6074	2.6127	2.6179	2.6232
Diffraction HPFW max (')	1.4457	1.4486	1.4515	1.4544	1.4573
Secondary undersize	.03297	.03491	.03685	.03878	.04071
Cassegrain focal length (cm)	3916.5	3908.6	3900.8	3892.9	3885.1
Focal plane scale ("/mm)	5.2665	5.2771	5.2877	5.2983	5.3090
Primary focal length (cm)	377.19	400.17	423.16	446.16	469.17
Primary focal ratio (f/)	1.2573	1.3339	1.4105	1.4872	1.5639
Primary sagitta (cm)	14.913	14.057	13.293	12.608	11.989
Primary departure from sphere (cm)	.15040	.12567	.10608	.09036	.07760
Primary hole min (cm)	17.907	16.784	15.660	14.536	13.410
Primary hole max (cm)	26.405	25.822	25.241	24.661	24.084
Secondary diameter (cm)	36.296	36.296	36.296	36.296	36.296
Secondary focal length (cm)	-52.22	-55.89	-59.62	-63.43	-67.30
Secondary conic constant (-e^2)	-1.472	-1.508	-1.546	-1.585	-1.625
Secondary sagitta (cm)	1.5655	1.4634	1.3723	1.2904	1.2165
Secondary departure from sphere (cm)	.01156	.00946	.00781	.00650	.00545
Secondary button min (cm)	3.9578	3.4172	3.8941	3.8613	3.8280
Secondary button max (cm)	5.7786	5.8634	5.9482	6.0331	6.1180
Secondary axial magnification	-108.8	-96.40	-85.98	-77.13	-69.57
Secondary angular magnification	.25023	.25073	.25123	.25174	.25224
Range for 1" blur					
Chop (')	.28366	.31966	.35791	.39843	.44125
Back focus (cm)	12.656	14.204	15.839	17.561	19.370
Field coma (')	15.149	15.089	15.028	14.968	14.908
Field astigmatism (') quadratic	14.296	14.338	14.380	14.422	14.465
Field curvature (') quadratic	4.3446	4.4708	4.5934	4.7128	4.8293
Alignment for 1" blur					
Secondary decenter (cm)	-.0156	-.0186	-.0220	-.0259	-.0301
Secondary tilt (')	-1.134	-1.275	-1.425	-1.583	-1.749
Secondary axial motion (cm)	.00228	.00256	.00286	.00318	.00351
Alignment for 1" motion					
Secondary decenter (cm)	-.0020	-.0022	-.0023	-.0024	-.0026
Secondary tilt (')	.06661	.06647	.06634	.06621	.06607
Initial alignment					
Secondary defocus for 20" blur (cm)	.04556	.05122	.05720	.06350	.07012
Secondary decenter for 10" coma (cm)	.15562	.18605	.22028	.25855	.30110
Secondary decenter for 1" corrected blur	.37791	.42856	.48286	.54088	.60274
Secondary decenter for 2.5' motion (cm)	.30353	.32420	.34517	.36645	.38805
Secondary tilt for 2.5' motion (')	9.9910	9.9709	9.9509	9.9309	9.9110
Secondary tilt for 10" coma (')	11.336	12.749	14.246	15.827	17.493

Table A-3. Primary-Focus/Primary-Sec Tradeoff

Aperture (cm)	300	300	300	300	300
Cassegrain focal ratio (f/)	13.5	13.5	13.5	13.5	13.5
Primary secondary separation (cm)	272	298	324	350	376
Primary focal plane separation (cm)	109	119	130	140	150
Field radius (')	2.5	2.5	2.5	2.5	2.5
Chop field amplitude (')	2.5	2.5	2.5	2.5	2.5
Minimum wave length (microns)	30	30	30	30	30
Maximum wave length (microns)	1000	1000	1000	1000	1000
Diffraction HPFW min (")	2.6074	2.6075	2.6074	2.6074	2.6075
Diffraction HPFW max (')	1.4485	1.4486	1.4485	1.4486	1.4486
Secondary undersize	.03490	.03493	.03488	.03491	.03494
Cassegrain focal length (cm)	3908.7	3908.5	3908.7	3908.6	3908.5
Focal plane scale ("/mm)	5.2770	5.2772	5.2769	5.2771	5.2772
Primary focal length (cm)	301.38	333.59	366.58	400.17	434.47
Primary focal ratio (f/)	1.0046	1.1120	1.2219	1.3339	1.4482
Primary sagitta (cm)	18.664	16.862	15.345	14.057	12.947
Primary departure from sphere (cm)	.29829	.21865	.16404	.12567	.09792
Primary hole min (cm)	14.484	15.231	16.038	16.784	17.529
Primary hole max (cm)	17.753	20.410	23.164	25.822	28.481
Secondary diameter (cm)	28.222	30.889	33.630	36.296	38.963
Secondary focal length (cm)	-31.83	-38.91	-46.98	-55.89	-65.78
Secondary conic constant (-e^2)	-1.362	-1.408	-1.457	-1.508	-1.563
Secondary sagitta (cm)	1.5500	1.5202	1.4934	1.4634	1.4335
Secondary departure from sphere (cm)	.01842	.01457	.01168	.00946	.00773
Secondary button min (cm)	2.8280	2.7430	3.5496	3.9263	4.3166
Secondary button max (cm)	3.7714	4.4135	5.1216	5.8634	6.6542
Secondary axial magnification	-169.2	-138.3	-114.7	-96.40	-81.93
Secondary angular magnification	.19495	.21338	.23230	.25073	.26916
Range for 1" blur					
Chop (')	.18049	.22143	.26780	.31966	.37753
Back focus (cm)	8.0207	9.8394	11.901	14.204	16.774
Field coma (')	15.089	15.088	15.089	15.089	15.088
Field astigmatism (') quadratic	12.507	13.131	13.751	14.338	14.910
Field curvature (') quadratic	3.4031	3.7521	4.1115	4.4708	4.8355
Alignment for 1" blur					
Secondary decenter (cm)	-.0079	-.0107	-.0143	-.0186	-.0239
Secondary tilt (')	-.9258	-1.038	-1.153	-1.275	-1.403
Secondary axial motion (cm)	.00146	.00179	.00215	.00256	.00301
Alignment for 1" motion					
Secondary decenter (cm)	-.0016	-.0018	-.0020	-.0022	-.0024
Secondary tilt (')	.08549	.07811	.07175	.06647	.06192
Initial alignment					
Secondary defocus for 20" blur (cm)	.02918	.03571	.04305	.05122	.06027
Secondary decenter for 10" coma (cm)	.07911	.10744	.14278	.18605	.23857
Secondary decenter for 1" corrected blur	.19085	.25514	.33427	.42856	.54055
Secondary decenter for 2.5' motion (cm)	.23748	.26523	.29417	.32420	.35547
Secondary tilt for 2.5' motion (')	12.824	11.716	10.762	9.9709	9.2882
Secondary tilt for 10" coma (')	9.2580	10.377	11.528	12.749	14.026

Table A-4. Overall Length Tradeoff

APPENDIX B

Pointing Control System Servomechanism Analysis

Glossary of Symbols

Θ_c Angular command (desired pointing) of mirror assembly with respect to inertial space

Θ_m Angular response (actual pointing) of mirror assembly with respect to inertial space

ϵ_m Angular pointing error of mirror assembly

J_W Moment of inertia of momentum wheel

τ_{TM} Torque developed by momentum wheel torque motor

J_m Moment of inertia of mirror assembly

τ_{ext} External torque applied to mirror assembly

k Spring rate of flex-pivot suspension of mirror assembly [torque units per radian]

T_M Torque developed by ancillary torque motor

Θ_H Angular position of Horseshoe gimbal with respect to local vertical

J_H Moment of inertia of Horseshoe gimbal

ω_H Frequency of angular vibration of Horseshoe gimbal [rad/sec]

S Laplace operator

$\dot{\Theta}_W$ Angular velocity of momentum wheel with respect to inertial space

K' Ancillary torque motor conversion gain [torque units per rad/sec]

AK_τ Amplifier-Torque motor constant [torque units per radian]

T_1 Lead time constant of lead/lag network

T_2 Lag time constant of lead/lag network

$\tau_{applied}$ Total systemic torque applied to the pendulous Horseshoe gimbal (reaction of ancillary torque motor and flex-pivot)

τ_ν Torque Noise (bearing torque noise, motor cogging, etc.)

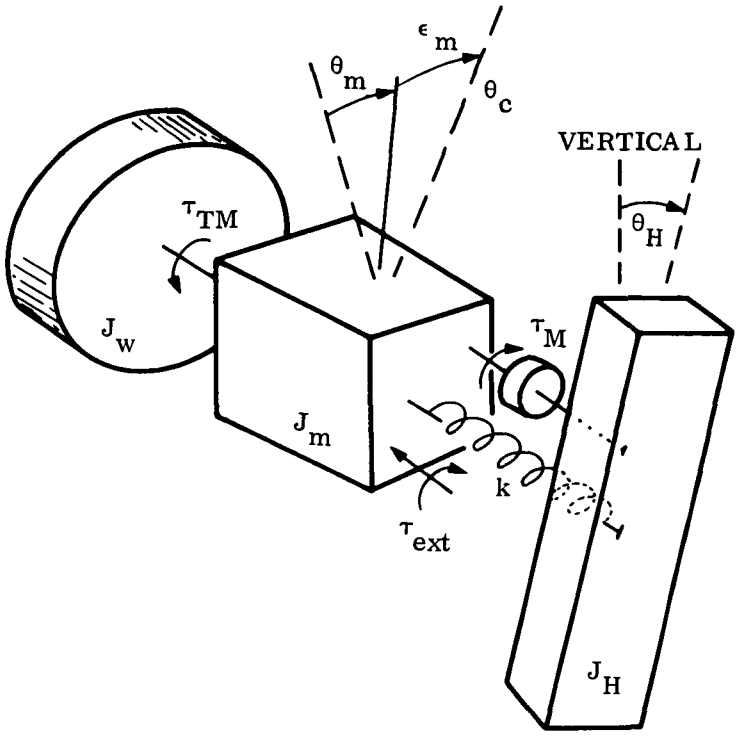

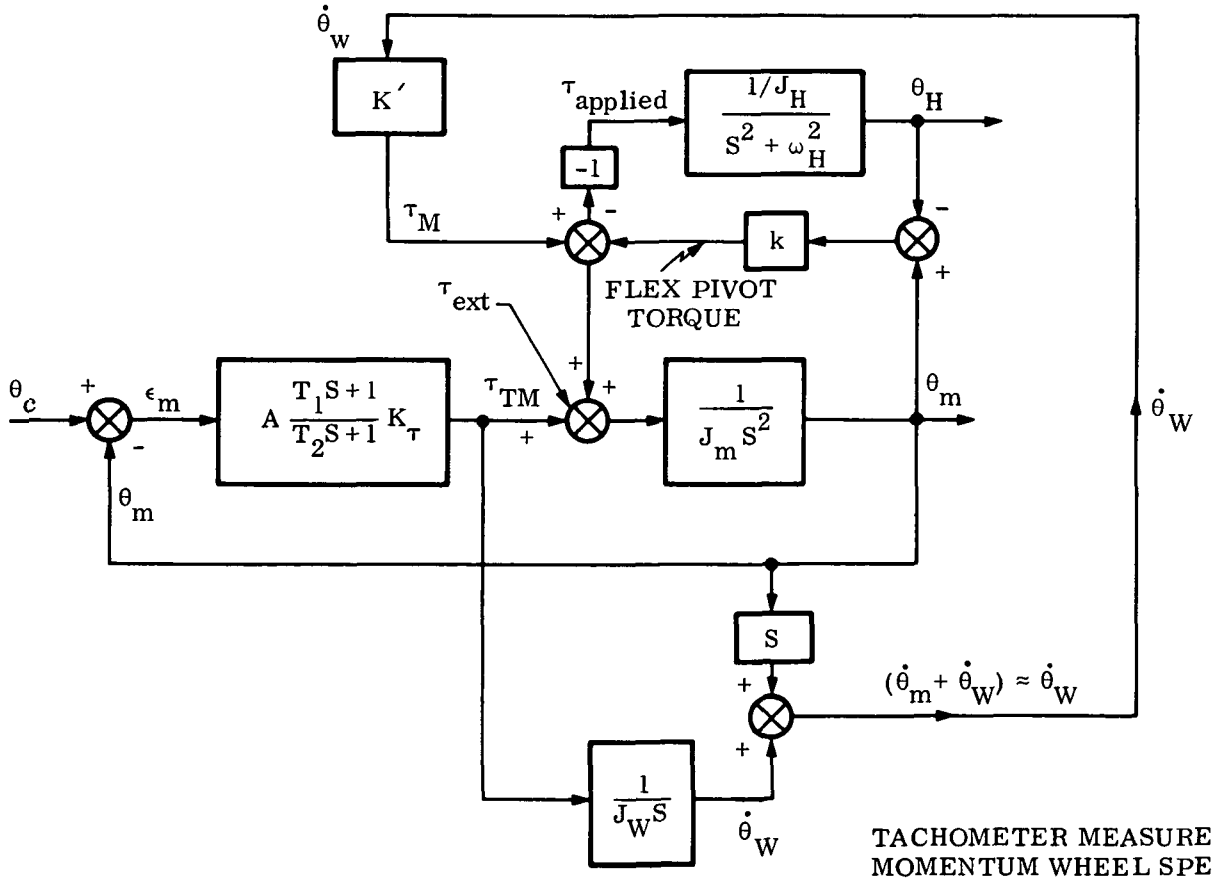

TACHOMETER MEASURE OF MOMENTUM WHEEL SPEED

System Dynamics Equation is:

$$\begin{bmatrix} \left[J_m S^2 + \frac{T_1 S+1}{T_2 S+1} AK_\tau \left(1 + \frac{K'}{J_W S}\right) + k\right] & -k \\ -\left[k + \frac{T_1 S+1}{T_2 S+1} AK_\tau \frac{K'}{J_W S}\right] & \left[\left(S^2+\omega_H^2\right)J_H+k\right] \end{bmatrix} \begin{Bmatrix} \Theta_m \\ \Theta_H \end{Bmatrix} =$$

$$\begin{Bmatrix} \frac{T_1 S+1}{T_2 S+1} AK_\tau \left(1+\frac{K'}{J_W S}\right)\Theta_c + \tau_{ext} \\ -\frac{T_1 S+1}{T_2 S+1} AK_\tau \frac{K'}{J_W S} \Theta_c \end{Bmatrix}$$

Determinant is:

$$\Delta(S) = \frac{1}{S}\left\{ J_m J_H S^5 + \left(J_m J_H \omega_H^2 + J_m k + J_H k\right) S^3 + \frac{T_1 S+1}{T_2 S+1} AK_\tau \left[\left(S^2+\omega_H^2\right)\left(J_H S + \frac{K' J_H}{J_W}\right)+kS\right] + \omega_H^2 J_H kS \right\}$$

which can be recast in form of:

$$\Delta(S) = \frac{1}{S(T_2 S+1)} \left\{K_6 S^6 + K_5 S^5 + K_4 S^4 + K_3 S^3 + K_2 S^2 + K_1 S + K_0\right\}$$

Stable!

Full System Response to Pointing Command

$$\theta_m = \frac{\begin{bmatrix} \frac{T_1S+1}{T_2S+1}\,AK_\tau\left(1+\frac{K'}{J_WS}\right)\theta_c + \tau_{ext} & -k \\ -\frac{T_1S+1}{T_2S+1}\,AK_\tau\,\frac{K'}{J_WS}\,\theta_c & \left[(S^2+\omega_H^2)J_H+k\right] \end{bmatrix}}{\Delta(S)}$$

or

$$\theta_m = \frac{1}{\Delta(S)}\left\{\left[(S^2+\omega_H^2)\,J_H\,\frac{T_1S+1}{T_2S+1}\,AK_\tau\left(1+\frac{K'}{J_WS}\right) + k\frac{T_1S+1}{T_2S+1}\,AK_\tau\right]\theta_c + \left[\left(S^2+\omega_H^2\right)J_H+k\right]\tau_{ext}\right\}$$

Final value of mirror pointing is:

$$\theta_m\Big|_{s.s.} = \lim_{S\to o} S\theta_m(S) = \lim_{S\to o}\frac{1}{\Delta(o)}\left\{\left[\omega_H^2 J_H AK_\tau\left(1+\frac{K'}{J_WS}\right) + kAK_\tau\right]\theta_c + \left[\omega_H^2 J_H+k\right]\tau_{ext}\right\}$$

or

$$\Theta_m\Big|_{s.s.} = \underset{S\to o}{\text{Lim}} \frac{1}{\omega_H^2 \frac{K'J_H}{J_W}AK_\tau} \left\{ \left[\omega_H^2 J_H AK_\tau \left(S + \frac{K'}{J_W} \right) + kAK_\tau S \right] \Theta_c + \left[\omega_H^2 J_H + k \right] S \tau_{ext} \right\}$$

$$= \frac{1}{\omega_H^2 \frac{K'J_H}{J_W}AK_\tau} \left\{ \omega_H^2 \frac{K'J_H}{J_W}AK_\tau \right\} \Theta_c$$

$$= \Theta_c$$

with zero final error even with torsional flex-pivots, external torque, and disturbing horseshoe-motion coupling.

FREQUENCY DOMAIN ERROR ANALYSIS

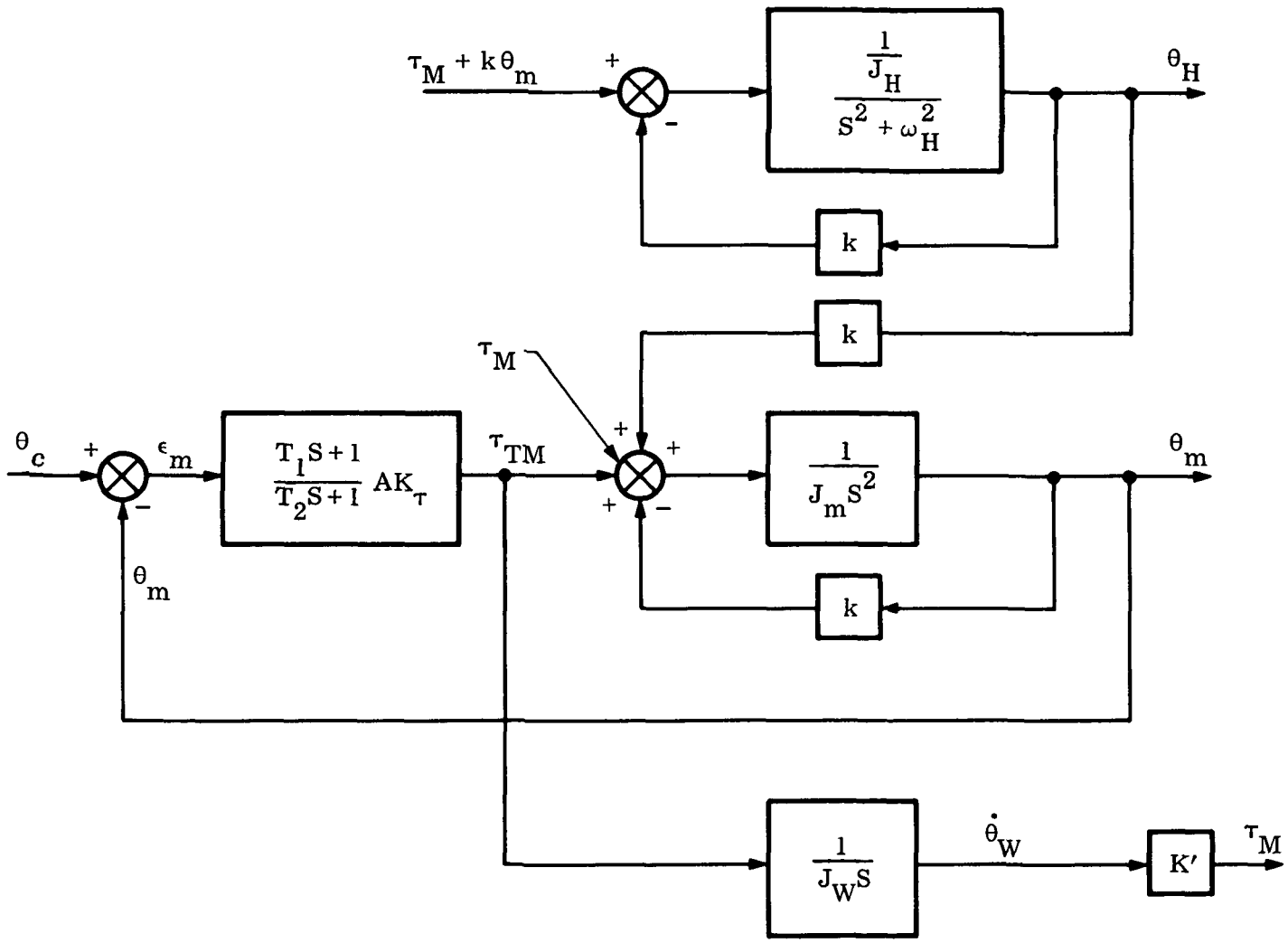

Mirror spectral sensitivity to Horseshoe Gimbal motion is given by:

$$\frac{\Theta_m}{\Theta_H} = \frac{\left(k \frac{J_W}{J_m}\right)\left(T_2 S+1\right) S}{K_4 S^4 + K_3 S^3 + K_2 S^2 + K_1 S + K_0}$$

where

$$K_4 = T_2 J_W$$

$$K_3 = J_W$$

$$K_2 = \left(\frac{J_W}{J_M} kT_2 + \frac{J_W}{J_m} AK_\tau T_1\right)$$

$$K_1 = \left(\frac{J_W}{J_m} k + \frac{AK_\tau K'}{J_m} T_1 + \frac{J_W}{J_m} AK_\tau\right)$$

$$K_0 = \frac{AK_\tau K'}{J_m}$$

Note: •Zero at origin reduces steady-state sensitivity to zero.

•Sensitivity at "horseshoe" gimbal frequency is given by above equation

FREQUENCY DOMAIN SKETCH OF SPECTRAL SENSITIVITY

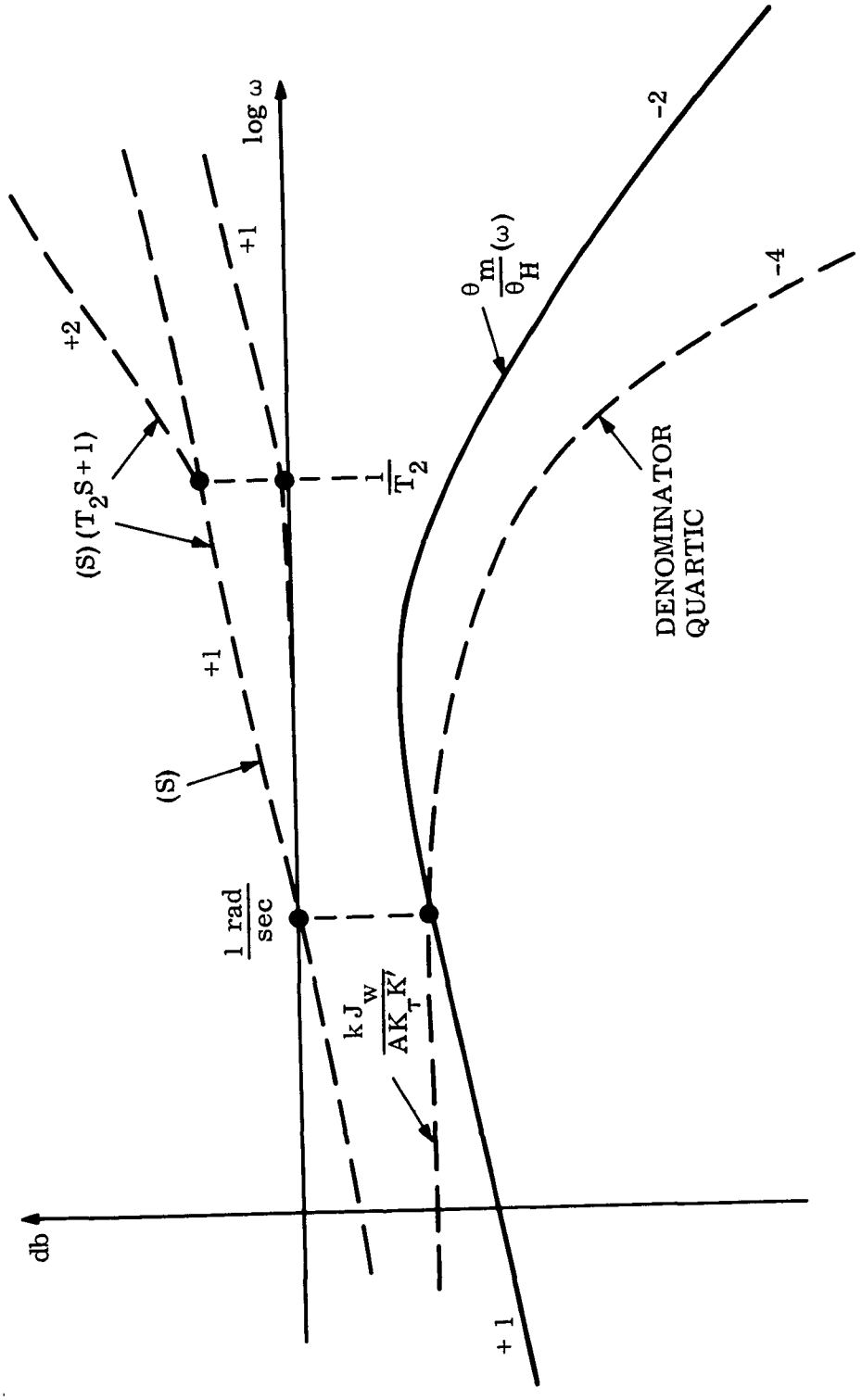

Because "horseshoe" gimbal characteristic frequency, ω_H, is very low, the low frequency asymptote of spectral sensitivity expression may be used:

$$\boxed{\frac{\Theta_m}{\Theta_H} \approx \frac{k\ J_w\ \omega}{A\ K_\tau\ K'}}$$

where $\omega = \sqrt{\omega_H^2 + \frac{k}{J_H}}$, rad/sec

k = flex-pivot constant, [torque units per radian]

J_W = momentum wheel moment of inertia [torque units per radian/sec^2]

AK_τ = amplifier torque motor constant [torque units per radian]

K' = ancillary torque motor conversion gain [torque units per rad/sec.]

J_H = horseshoe moment of inertia [torque units per rad/sec^2]

System Spectral Sensitivity to Torque Noise

$$\frac{\Theta_m}{\tau_\nu}(S) = \frac{1}{\Delta(S)} \left\{ (S^2+\omega_H^2)J_H+k \right\}$$

or

$$\frac{\Theta_m}{\tau_\nu}(S) = \frac{S[T_2S+1][S^2+\omega_H^2+\frac{k}{J_H}]J_H}{K_6S^6+K_5S^5+K_4S^4+K_3S^3+K_2S^2+K_1S+K_0}$$

where:

$$K_6 = J_m J_H T_2$$

$$K_5 = J_m J_H$$

$$K_4 = [(J_m J_H \omega_H^2+J_m k+J_H k)T_2+AK_\tau J_H T_1]$$

$$K_3 = \left[J_m J_H \omega_H^2+J_m k+J_H k+AK_\tau J_H+AK_\tau T_1 \frac{K'J_H}{J_w} \right]$$

$$K_2 = \left[AK_\tau \frac{K'J_H}{J_W} + AK_\tau(\omega_H^2 J_H+k)T_1+\omega_H^2 J_H k T_2 \right]$$

$$K_1 = \left[AK_\tau(\omega_H^2 J_H+k)+AK_\tau \omega_H^2 T_1 \frac{K'J_H}{J_w} + \omega_H^2 J_H k \right]$$

$$K_0 = AK_\tau \omega_H^2 \frac{K'J_H}{J_w}$$

SPECTRAL TORQUE-NOISE SENSITIVITY

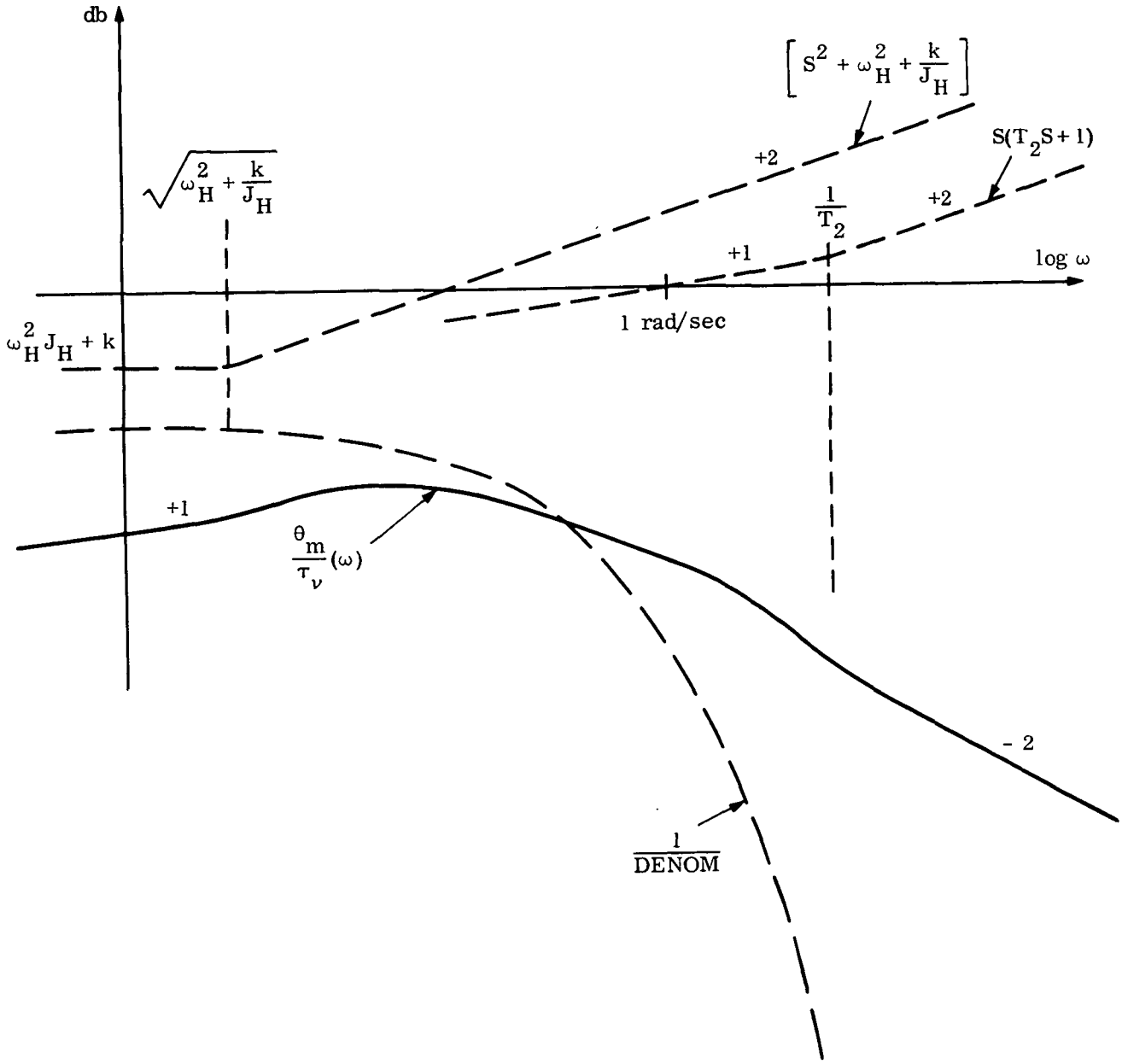

The low frequency asymptote may be approximated by:

$$\frac{\Theta_m}{\tau_\nu} \approx \frac{\left(\omega_H^2+\frac{k}{J_H}\right)J_H}{AK_\tau \omega_H^2 \frac{K'J_H}{J_W}} \omega_\nu$$

(low freq.)

$$\approx \frac{\left(\omega_H^2 + \frac{k}{J_H}\right)J_W}{AK_\tau \omega_H^2 K'} \omega_\nu$$

$$\approx \frac{J_W}{AK_\tau K'} \omega_\nu$$

where ω_ν is the circular frequency of the torque-noise in rad/sec.

Generic Control

The controlled system can be written as:

$$\ddot{X}_T = -K_{FP}/J_T \; X_T + T_c/J_T + \frac{X_c \; K_{FC}}{J_T} \qquad (1)$$

where X_T is the angle being controlled

K_{FP} is a spring constant

J_T is an inertia

T_c is the control torque

X_c is the command input

If we select a simple proportional plus rate controller we have:

$$T_c = -K_g \; (\dot{X}_T \; \tau + X_T) \qquad (2)$$

where: τ is the zero location of the controller

K_g is the control gain

Combining (2) and (1) and rewriting we get:

$$\ddot{X}_T + \frac{K_g \tau}{J_T} \dot{X}_T + \frac{(K_{FP} + K_g)}{J_T} X_T = \frac{K_{FP}}{J_T} X_c \qquad (3)$$

The generic equation for a 2nd order system like this is:

$$\ddot{X} + 2\zeta\omega_n \dot{X} + \omega^2_n X = \omega_n^2 \; X_c \qquad (4)$$

where: ζ is the damping ratio

ω_n is the natural frequancy

If we select ω_n, ζ we can match coefficients between (4) & (3):

$$\frac{K_g + K_{fp}}{J_T} = \omega^2_{n_o} \qquad (5)$$

$$\frac{K_g \; \tau}{J_T} = 2\zeta_o \omega_{n_o} \qquad (6)$$

In this way we solve for K_g and τ and get our control.

The individual loops are then combined into a system of equations and solved. Some adjustments are made for the ignored coupling.

Elevation Axis Equation.

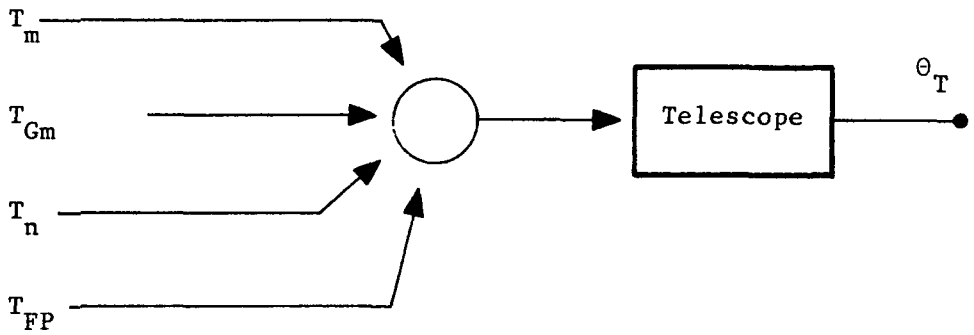

The equation of motion of the telescope is:

$$J_T\ddot{\Theta}_T = K_{FP}(\Theta_g - \Theta_T) + T_{Gm} + T_m + T_n \qquad (1)$$

where: J_T is the telescope inertia

Θ_T is the telescope angular position

K_{FP} is the flex-pivot sprint constant

Θ_g is the gondola's angular position

T_{Gm} is the gimbal motor torque

T_m is the reaction wheel motor

T_n is noise torque

The equation of motion for the gondola is

$$J_g\ddot{\Theta}_g = K_{Fp}(\Theta_T - \Theta_g) - T_{Gm} - \omega_p^2 J_g \Theta_g \qquad (2)$$

where: ω_p is the compound pendulum natural frequency.

Elevation Axis Equation (continued):

Equation of motion of the Reaction Wheel is:

$$J_{r\omega}\ddot{\Theta}_{R\omega} = -T_m \tag{3}$$

The control law states:

$$T_m = k_1 \frac{(\tau_1 S+1)}{(\tau_2 S+1)} \tag{4}$$

&

$$T_{Gm} = K_2\ddot{\Theta}_{R\omega} \tag{5}$$

If we put these equations into state space form as the following:

$$\left.\begin{aligned} X_1 &= \Theta_T \\ X_2 &= \dot{\Theta}_T \\ X_3 &= \Theta_g \\ X_4 &= \dot{\Theta}_g \\ X_5 &= \dot{\Theta}_K \\ X_6 &= \Theta_1 \end{aligned}\right\} \tag{6}$$

where: Θ_1 is used to define a state existing in the control law or:

$$T_m = K_1\,\Theta_1 \tag{7}$$

Elevation Axis Equations:

Eqs. (1), (2), (3) & (4) with eqs. (6) can be put into 6 first order differential equations:

$$\dot{X}_1 = X_2 \tag{8}$$

$$\dot{X}_2 = \frac{1}{J_T}\left[-K_{Fp}\, X_1 + K_{Fp}\, X_3 - K_2\, X_5 + K_1\, X_6 + T_n\right] \tag{9}$$

$$\dot{X}_3 = X_4 \tag{10}$$

$$\dot{X}_4 = \frac{1}{J_g}\left[K_{Fp}\, X_1 - X_3\,(K_{Fp} + \omega_p{}^2\, J_g) + K_2\, X_5\right] \tag{11}$$

$$\dot{X}_5 = -\frac{K_1}{J_{F\omega}}\, X_6 \tag{12}$$

$$\dot{X}_6 = \frac{1}{\tau_2}\left[-X_1 - \tau_2\, X_2 - X_6 + X_6\right] \tag{13}$$

Where: X_6 is the commanded signal for the telescope. These equations can be placed in matrix form as

$$\dot{\underline{X}} = [A]\underline{X} + [B]\underline{u} \tag{14}$$

where: [A] is the matrix of coefficients of the x_i's

$$\underline{u} = \begin{bmatrix} x_c \\ T_n \end{bmatrix}$$

$$[B] = \begin{bmatrix} 0 & 0 \\ 0 & \frac{1}{J_T} \\ 0 & 0 \\ 0 & 0 \\ 0 & 0 \\ \frac{1}{\tau_2} & 0 \end{bmatrix}$$

In this form the system was run through a program called "TF" (Transfer Function) written at Stanford University to generate system responses.